

Mapping functional dynamics and neuronal structure in a hindbrain neural integrator circuit

Master's thesis

submitted by

Florian Felix Kämpf

at the

Universität
Konstanz



AG-Bahl

Departement of Biology

1. Reviewer: Armin Bahl
2. Reviewer: Patrick Müller

Konstanz, 2023

To my gecko Pippin,
who studied with me all this
time in Konstanz but
couldn't see me graduate.



Abstract

Animals have to process a multitude of noisy information in their natural environment. To analyze and transform these signals into accurate behavioral outputs, neurons are organized in neural circuits that perform complex tasks through distributed activity in the brain. To understand the sensorimotor transformations performed in neural networks, it is necessary to understand their components and how they subsequently interact. In the case of biological neural networks, these characteristics include cell activity, which is the information a cell transmits; neurotransmitter identity, which is how a cell transmits its information; and connectivity, which is the partner of a cell that receives the transmitted information. Building upon the work of the established model of the motion integrator network in the anterior hindbrain of the zebrafish (Bahl & Engert, 2020), we investigate these modalities and combine them within each fish.

In our first chapter, we expand the model of the hindbrain integrator by using volumetric functional two-photon imaging, leveraging the innate optomotor response of zebrafish through random dot motion stimuli presentation. We analyze their functional neural dynamics using biased and unbiased metrics to identify the distribution of functional neuron classes over the zebrafish hind- and midbrain. We find several new spatial clusters of motion response cells, show how known localizations display unknown responses to motion stimuli, and reidentify the expected localization of established functional cell classes of the motion integrator.

In Chapter 2, we introduce HCR RNA-FISH as a method to detect the neurotransmitter identity of functional cell classes. Additionally, we add registration parameters to ensure automatic cell-wise mapping of HCR RNA-FISH-stained brains for automatic cell-wise neurotransmitter identification. We validate HCR RNA-FISH as a powerful tool to access neurotransmitter identity, and set the stage for automatic cell-wise neurotransmitter identification across the whole brain.

In Chapter 3, we synthesize functional dynamics and neurotransmitter identity with neurite morphologies within the same fish, by functionally guided photoactivations. This enables us to study the zebrafish hindbrain motion integrator in unprecedented modalities combining neural dynamics, neurotransmitter identity, and neurite morphology of the same cell within the same animal. We find several morphological classes associated with functional neuron classes, establishing a crucial link between cell function and morphology.

Overall, this represents a major step towards understanding the neural circuits of complex sensorimotor transformations. This brings us closer to understanding the basic principles of how neural circuits solve complex tasks through the interplay of morphology and cell activity.

Zusammenfassung

Tiere müssen in ihrer natürlichen Umgebung eine Vielzahl von verrauschten Informationen verarbeiten. Um diese Signale zu analysieren und in genaue Verhaltensaustauschen umzuwandeln, sind Neuronen in neuronalen Schaltkreisen organisiert, die über die verteilte Aktivität im Gehirn erstaunliche Probleme lösen. Um die in neuronalen Netzen durchgeföhrten sensomotorischen Transformationen zu verstehen, muss man ihre Komponenten und ihr Zusammenspiel kennen. Im Falle biologischer neuronaler Netze umfassen diese Merkmale die Zellaktivität (die Informationen, die eine Zelle überträgt), die Identität der Neurotransmitter (die Art und Weise, wie eine Zelle ihre Informationen überträgt) und die Konnektivität (die Partner einer Zelle, an die sie ihre Informationen überträgt). Unter Verwendung des etablierten Modells des Bewegungsintegrator-Netzwerks im vorderen Hinterhirn des Zebrafisches (Bahl & Engert, 2020) untersuchen wir diese Modalitäten und kombinieren sie innerhalb eines Fisches.

In unserem ersten Kapitel erweitern wir das Modell des Hinterhirnintegrators, indem wir die angeborene optomotorische Reaktion von Zebrafischen auf die Projektion von zufälligen Punktbewegungsreizen mit Hilfe der volumetrischen funktionellen Zwei-Photonen-Bildgebung nutzen. Wir analysieren ihre funktionelle neuronale Dynamik mit Hilfe von voreingenommenen und nicht voreingenommenen Metriken, um die Verteilung der funktionellen Neuronenklassen im Hinter- und Mittelhirn des Zebrafisches zu identifizieren. Wir finden mehrere neue Lokalisationen von Bewegungsreaktionszellen, zeigen, wie bekannte Lokalisationen unbekannte Reaktionen auf Bewegungsreize aufweisen, und identifizieren die erwartete Lokalisation etablierter funktioneller Zellklassen des Bewegungsintegrators.

In Kapitel 2 stellen wir HCR RNA-FISH als Methode zur Erkennung der Neurotransmitter-Identität funktioneller Zellklassen vor und fügen Registrierungsparameter hinzu, um eine zellweise Zuordnung von HCR RNA-FISH-gefärbten Gehirnen zu gewährleisten, um eine automatische zellweise Neurotransmitter-Identifizierung sicherzustellen. Wir validieren HCR RNA-FISH als leistungsfähiges Werkzeug für den Zugang zur Neurotransmitter-Identität und schaffen die Voraussetzungen für die automatische zellweise Identifizierung von Neurotransmittern im gesamten Gehirn.

In Kapitel 3 synthetisieren wir funktionelle Dynamik und Neurotransmitter-Identität mit Neuritenmorphologien innerhalb desselben Fisches durch funktionell geleitete Photoaktivierungen. Auf diese Weise können wir den Zebrafisch-Hinterhirn-Bewegungsintegrator in noch nie dagewesener Weise untersuchen, indem wir neurale Dynamik, Neurotransmitter-Identität und Neuritenmorphologie derselben Zelle innerhalb desselben Tieres kombinieren. Wir finden mehrere morphologische Klassen, die mit funktionellen Neuronenklassen assoziiert sind, und stellen damit eine entscheidende Verbindung zwischen Zellfunktion und Morphologie her.

Insgesamt ist dies ein wichtiger Schritt zum Verständnis der neuronalen Schaltkreise komplexer sensomotorischer Transformationen und bringt uns dem Verständnis der grundlegenden Prinzipien näher, wie neuronale Schaltkreise komplexe Aufgaben durch das Zusammenspiel von Morphologie und Zellaktivität lösen.

Contents

1 Investigation of functional dynamics of a motion integrator using biased and unbiased metrics	7
1.1 Introduction	7
1.2 Methods	9
1.2.1 Experimental Design and Setup	9
1.2.2 Animal Preparation	9
1.2.3 Imaging Procedure	10
1.2.4 Data Preprocessing and Segmentation	10
1.2.5 Neural Response Analysis	12
1.3 Results	15
1.3.1 Expanding the hindbrain integrator circuit	15
1.3.2 Localizing brain-wide distribution of a rare component of the integration circuit	18
1.3.3 Unbiased responsitivity and reliability metrics of the larval zebrafish hindbrain during the RDMS	20
1.3.4 Metric-based cluster detection	22
1.3.5 DBSCAN-based cluster formation	24
1.3.6 Revealing structure in the zebrafish brain by k-means clustering cell metrics	27
1.3.7 Revealing structure in the zebrafish brain by clustering RDMS neural response dynamics	30
1.4 Discussion	31
1.4.1 Logic-based selection identifies several loci of rebound neurons	32
1.4.2 Unbiased metric maps reveal novel motion-responsive Regions and validate established Centers in the Zebrafish Brain	32
1.4.3 Neighborhood-Based synchrony metrics highlight functional clusters	34
1.4.4 Mutual information as a tool for inferred connectivity	34
1.4.5 K-means clustering of neural response metrics separates subcircuits of motion integration	35
1.4.6 Conclusion	37
2 HCR RNA-FISH as a method to identify cellular neurotransmitter identity	37
2.1 Introduction	37
2.2 Methods	38
2.3 Results	41
2.3.1 Establishing HCR RNA-FISH as a method to identify neuro-transmitter identity of functionally identified cells	41
2.3.2 Establishing a metric for brain mapping using ANTs (Avants et al., 2015)	44
2.4 Discussion	45
2.4.1 HCR RNA-FISH staining of Gad1b/Vglut2a mRNA shows colocalization with endogenously marked Gad1b/Vglut2a	46

2.4.2	B-Spline-Syn registration enables cell-to-cell mapping between pre-HCR and post-HCR imaging stacks of zebrafish brains	46
2.4.3	Outlook	47
3	Functionally guided photoactivation to map neurite morphologies	47
3.1	Introduction	47
3.2	Methods	48
3.3	Results	50
3.3.1	Functionally guided photoactivations	50
3.3.2	Analysis of photoactivated cell neurites	53
3.3.3	Synthesizing functional dynamics, projection patterns, and neurotransmitter identity	55
3.4	Discussion	56
3.4.1	Functionally Guided Photoactivations: A Comparative Analysis of Pros and Cons	57
3.4.2	Updating the motion integrator circuit through functionally guided photoactivations	58
3.4.3	Conclusion	60

List of Figures

1	Two-photon imaging in the mid- and hindbrain of the anterior hindbrain of the larval zebrafish during RDMS presentation	17
2	Logic-based selection reveals spatial clusters of rebound cells	19
3	Metric maps of responsitivity, reliability, and stimulus information across all cells	21
4	A lateral cluster in the eminentia granularis	22
5	Metric maps combining distance and activity reveal spatial organization of the motion integration network	24
6	DBSCAN clustering of density-based metrics highlights various functional clusters	26
7	K-means clustering of cells based on responsitivity, reliability, and stimulus information metrics	29
8	K-means clustering of neural responses finds established functional classes of the motion integrator	31
9	Verification of registration quality using the Hausdorff-distance	43
10	Colocalization of endogenous Gad1b/Vglut2 expression and gad1b/vglut2a staining	45
11	Functionally guided photoactivations to connect functional responses, neurotransmitter identity, and morphology	52
12	Neurite morphologies of functionally characterized neurons	54
13	An overview of all neurite morphologies	56

List of Tables

1	Categorization of neurons by functional cell type, morphological class, and neurotransmitter identity. .	55
---	--	----

1 Investigation of functional dynamics of a motion integrator using biased and unbiased metrics

1.1 Introduction

Animals live in various environments under a multitude of conditions that offer complex and variable signals. Information in these environments is often accompanied by a huge amount of noise, which makes it difficult to extract ecologically relevant information from their surroundings to respond accordingly. Animals thus need robust mechanisms that process and extract useful information from their senses to navigate their environment, make decisions, and maximize their fitness (Adami, 2012). The basic processing unit, the neuron, enables transformative evaluation of all these stimuli. However, it is not suited to this problem independently, limited through its biophysical properties. Through its interconnection with other neurons forming neural networks, the ability to manage such a large amount of information arises (Hopfield, 1982).

Since Hopfield, much time has passed, and nowadays, research has identified many neural circuits are found to process a multitude of complex tasks, including learning (Makino et al., 2016; Malleret et al., 2010), path integration (McNaughton et al., 2006), hunger (Tsao et al., 2018), orientation (Gomez-Marin & Louis, 2012), circadian rhythm (Aston-Jones et al., 2001), social behavior (Krishnan et al., 2007) and motion integrations (Bahl & Engert, 2020; Hanks et al., 2006). These neural circuits are distributed across various model systems, including mice (Aston-Jones et al., 2001; Evans et al., 2018), monkeys (Hanks et al., 2006; Huk et al., 2017), Drosophila (Borst, 2014; Creamer et al., 2018; Groschner et al., 2022), and zebrafish (Ahrens et al., 2012; Bahl & Engert, 2020; Dragomir et al., 2020; Petrucco et al., 2023).

One particularly interesting model organism for investigating neural circuits is the larval zebrafish. Through its small size and transparency, zebrafish larvae present an ideal vertebrate model for the investigation of neural circuits (Bilotta & Saszik, 2001; Naumann et al., 2016; Vargas et al., 2011). Current research has investigated this through two-photon (Bahl & Engert, 2020) and light sheet (Ahrens et al., 2013; Vladimirov et al., 2014) whole brain imaging, as well as optogenetic techniques (Baier & Scott, 2009; Dal Maschio et al., 2017; Förster et al., 2017; Förster et al., 2018; Schoonheim et al., 2010). Furthermore, zebrafish larvae display a wide array of behaviors including motion integration (Bahl & Engert, 2020; Dragomir et al., 2020) escape behaviors (Douglass et al., 2008; Dunn, Gebhardt, et al., 2016), phototaxis (X. Chen & Engert, 2014; Hartmann et al., 2018) and other interesting less investigated behavioral outputs (Audira et al., 2018; Qin et al., 2014; Reddy et al., 2021; Saverino & Gerlai, 2008).

Foremost, the larval zebrafish shows the inherent reflex of the optomotor response (OMR), which regulates the positional homeostasis of individuals in moving streams based on visual cues (Fleisch & Neuhauss, 2006; E. Yang et al., 2022). This innate response of the larval zebrafish can be easily triggered in experimental setups without previous training through using the well-established random dot motion paradigm which was first adopted in primates (Newsome & Pare, 1988). Furthermore, the randomly appearing and disappearing dots of the stimuli have a low lifetime, making it impossible for the zebrafish to track individual dots while still showing a uniform distribution of motion over the presentation area. This sets an excellent experimental stage for the behavioral examination of the integration of motion in the larval zebrafish (Bahl & Engert, 2020; Dragomir et al., 2020) and furthermore brain imaging of the corresponding neural networks (Bahl & Engert, 2020; Dragomir et al., 2020).

This neural investigation is enabled through GCaMP (Zhang & Looger, 2023) a calmodulin-bound version of Green

fluorescent protein (GFP). GCaMP fluoresces at different brightness levels based on intracellular calcium, which spikes on action potentials. Using this genetically encoded calcium indicator (GECI) enables long-term two-photon imaging during the stimulation through random dot motion stimuli (RDMS). This revealed the neural dynamics of motion integration in zebrafish (Bahl & Engert, 2020; Dragomir et al., 2020).

This non-invasive method of examining neural circuits within the larval zebrafish poses an ideal experimental approach to the neural investigation of cells and brain regions involved in motion integration. Previous studies highlighted the pretectum (Kubo et al., 2014; Naumann et al., 2016; Wang et al., 2019) and the anterior hindbrain (X. Chen et al., 2018; Dunn, Mu, et al., 2016) as regions involved in the preprocessing and processing of motion stimuli within the zebrafish brain. Bahl and Engert, 2020 revealed several functional classes of neuron responses in the GCaMP signal of cells within the anterior hindbrain during motion presentation. In particular, they showed that neural dynamics in the anterior hindbrain are significantly slow, suggesting they temporally integrate motion. This suggests that this area temporally integrates information during sensory-motor decision-making. In addition, regression analysis of functional cell response based on behavioral experiment was used to establish the anterior hindbrain as a center of distributed computation of temporal integration.

Decisions based on this kind of temporal integration, like the OMR, can be described by bounded drift-diffusion models. These models have decision thresholds (Ratcliff & McKoon, 2008) representing a point at which enough information has been collected to inform a behavior. These models were able to link the temporal dynamics within the lateral intraparietal cortex (LIP) to slow temporal integration within monkeys (Hanks et al., 2006; Huk et al., 2017; Shadlen & Newsome, 2001). However, further investigations of LIP and the related middle temporal visual area (MT) have shown that this approach cannot fully explain motion integration and decision-making (Katz et al., 2016; Yates et al., 2017). Through using a whole-brain imaging approach within the larval zebrafish, Bahl and Engert, 2020 could relate the identified functional classes of neurons involved in the motion integration, subsequently informing the directional decision tasks of the OMR to the underlying components of such a drift-diffusion model. Through their behavioral experiments and the cell-wise identification of neurons participating in motion integration, Bahl and Engert, 2020 proposed a simple bounded leaky integrator model. This model is based on three neuron types. In this model the first neuron, representing a dynamic threshold, and the second, representing an evidence integrator, converge in a push-and-pull configuration onto the third class, which executes swimming decisions whenever the evidence integrator overpowers the dynamic threshold. Through this configuration the model was able to predict neural dynamics as well as behavioral output.

A technique complementing this cell-wise approach to neural circuit investigation is the mapping of cells and the corresponding image stacks to larval brain atlases (Kunst et al., 2019; Randlett et al., 2015). This enabled Bahl and Engert, 2020 to compare cells across individual zebrafish larvae, which aided in identifying rare cell types. This also enables brain region analysis by automatically detecting which cells lie within which brain regions. Thus, brain regions can be identified based on their general function. Functional clusters within these brain regions (Buzsáki & Mizuseki, 2014) can then be identified by associating certain coordinates in these atlases with specific responses of cells across fish thus establishing functional cell clusters.

Bahl and Engert, 2020 identified neurons belonging to functional classes by regression analysis based on previously conducted behavioral experiments. However, when assigning and identifying functional classes of neurons, alternative methods exist such as clustering (Helton et al., 2019; Kubo et al., 2014; Masquelier & Thorpe, 2007), correlational analysis (Dombeck et al., 2009), neural networks (Haesemeyer et al., 2019), and metric analysis (Freeman et al., 2014; Naumann et al., 2016) based on both neural dynamics (Masquelier & Thorpe, 2007) and cell morphology (Helton et al., 2019). These characterization metrics range from uniformed, such as clustering, to biased, such as regression analysis, and thus explore the functional cell categories in different lights.

In this chapter, we evaluate the neural circuit proposed by Bahl and Engert, 2020 using biased and unbiased methods to identify neurons belonging to the functional classes constituting this circuit. We hereby create an alternative

and more flexible version of regression analysis using logical conditions based on general dynamics of functional neural responses of the targeted neuronal class. We furthermore introduce and evaluate multiple unbiased responsiveness and reliability metrics on the larval zebrafish processing when presented with a random dot motion stimuli. We also attempt to identify potential unknown functional clusters within the motion integration circuit in the anterior hindbrain of the zebrafish by assuming colocalization of functional neuron types in close physical neighborhoods (Buzsáki & Mizuseki, 2014; Ohki et al., 2005). Lastly, we perform K-means clustering on our established metrics to explore patterns across the zebrafish brain during motion response. We contrast k-means clustering on metrics with K-means clustering of neural dynamics of motion-responsive cells to reconstruct the neural classes proposed by Bahl and Engert, 2020. Through these approaches, we aim to confirm and expand the established motion integrator in the zebrafish hindbrain while establishing a combination of unbiased and biased metrics to evaluate neural circuits based on cell localization and functional responses.

1.2 Methods

1.2.1 Experimental Design and Setup

1.2.2 Animal Preparation

Animal Preparation: To obtain zebrafish larvae, we incrossed transgenic *Tg(elavl3:H2B-GCaMP8s)* fish with a *mitfa* \sim mutant background in bucket crosses of up to 6 animals. We added rested adult zebrafish to breeding tanks supplied with spawning substrate mimicking plants to stimulate breeding. We put parent animals in breeding tanks until the following morning, when we checked the tanks for eggs and harvested them. We raised 50 - 100 larvae in 14.5 cm diameter Petri dishes in E3 water (5 mM NaCl, 0.17 mM KCl, 0.33 mM CaCl₂, 0.33 mM MgCl₂, 10-5%) with supplemented methylene blue for one day before cleaning eggs and switching to (normal) E3 water without methylene blue. We raised animals at 28 °C in an incubator on a 14:10 day:night cycle. Before imaging the 5 days post fertilization (dpf) larvae, we screened them for the *mitfa* \sim phenotype, which manifests in pigmentless larvae, and strong nuclear localized H2B-GCaMP8s expression with a Zeiss AxioZoom v16 microscope to ensure optimal imaging quality.

Stimulus Presentation: To elicit motion integration in the larval zebrafish, we designed an adaptation of the RDMS as described by Shadlen and Newsome, 2001. Our presented RDMS consisted of a maximum of 1200 1 mm-sized red dots on a black background, generated using Panda3D (Surer, 2020). The stimulus was projected using a P300 Neo Pico projector (Aaxa Technologies) onto diffusive paper attached to the bottom of the experimental platform with an 8 cm diameter circle. A red foil was placed in front of the projector's lens to prevent unintended bleed-through of non-red light into the photomultiplier tubes (PMT). We ensured that the imaged larvae were positioned at the center of the experimental platform to occupy the maximum field of view with the stimulus. The dots were continually and stochastically redrawn, each assigned a new position with a maximum lifetime of 200 ms to prevent successful dot tracking by the larvae. The stimulus sequence consisted of an initial 10 s of 0% coherence movement, followed by 40 s of 100% coherent movement either to the left (RDMS-L) or to the right (RDMS-R), with the direction being randomly assigned for each trial. Finally, the stimulus concluded with 10 s of 0% coherence movement.

Fish lines: For imaging, the transgenic line *Tg(elavl3:H2B-GCaMP8s)* was used (Zhang & Looger, 2023). (Fast and Sensitive GCaMP Calcium Indicators for Imaging Neural Populations | Nature, n.d.) This line is an improved and brighter nuclear-localized version of the calcium indicator GCaMP6s (T.-W. Chen et al., 2013). This GECI provides a non-invasive, reliable measurement of intracellular calcium, an indirect measurement for action potentials in neurons. The fusing of the GCaMP8s protein to the histone protein H2B ensures nuclear localization and, thus, better segmentability.

1.2.3 Imaging Procedure

Agarose restraint: To ensure stability while performing functional imaging, larvae were embedded within a 6 cm diameter Petri dish with low melting agarose 1.6% - 2.0% (UltraPure Low Melting Point Agarose, 16520-100, Invitrogen) at 40°C. We ensured that fish were not rolled or tilted in their body axis by correcting their posture in the agarose with a small pipette tip. After the agarose solidified, we filled the Petri dish with E3 water without methylene blue.

Functional two-photon calcium imaging: Larvae were prescreened for the *mitfa* -/- phenotype and bright expression of H2B-GCaMP8s. After embedding, we transferred the fish under the custom-built two-photon microscope. We adjusted the fish's position under the microscope with a head camera, creating an image based on the fish's absorption of a 730 nm LED light source placed under the fish. The two-photon setup was operated using a custom Python 3.10-based software (PyZebra2P). The custom two-photon microscopes consist of a femtosecond-pulsed MaiTai Ti:Sapphire laser (SpectraPhysics) operated at 950 nm to image the H2B-GCaMP8s at its peak excitation wavelength. During imaging, the laser was scanned over the focal area with a set of x/y-galvanometers (8315K series, 6 mm mirrors, Cambridge technology). We set the power of the imaging beam to 13.8 mW at the specimen, to avoid harming the larvae. We regulated the imaging beam power with a combination of a λ -half plate and a Glan-Thomson prism. The objectives differed between the two microscopes used and consisted of a 20x Olympus objective and a 25x Nikon objective. We collected the fluorophore emission using an akali photomultiplier (Hamamatsu). Further information on the custom-built two-photon microscopes can be found in (Fuchsloch, 2023). While imaging the larvae's hind- and midbrain, we scanned each plane for 30 min, with a framerate of 1 Hz over an area of 800x800 pixels at a resolution of 0.4 μ m per pixel. There was an interval of 6 μ m between each plane. While scanning each plane for 30 min, we presented RDMS as described above. The stimulus was presented 15 times in its leftward orientation and 15 times in its rightward orientation, with direction of stimuli randomly ordered. Each larva was imaged across 15 planes, creating a total imaging time of 8.5 h per fish.

1.2.4 Data Preprocessing and Segmentation

Data cleaning: Data was cleaned using a custom-written Python 3.11-based preprocessing script. Firstly, due to the design of the image reconstruction algorithm the acquired raw data was cleaned by filling missing pixels with an estimated pixel value based on the surrounding existing pixels for each frame acquired. This was completed using the `inpaint` function of the OpenCV library (Bradski, 2000). To compensate for the potential movement of the fish during imaging, we applied rigid motion correction using the `MotionCorrect` function with the parameters `[max_shifts = (60, 60), strides = (48, 48), overlaps = (24, 24), max_deviation_rigid = 3, splits_rig = 14, splits_els = 14]` and the `apply_shifts_movie` function with the parameters `[border_nan = True]` of the computational toolbox for large-scale calcium imaging data analysis (CalmAn) (Giovannucci et al., 2019). Furthermore, we temporally aligned the gathered imaging data using stimulus onset times with the `interp1d` function of `scipy` (Virtanen et al., 2020) using a time discretization of 0.5 s to interpolate the imaging signal. We also created average images based on the motion-corrected videos to use within cell segmentation.

Cell Segmentation: We segmented cell nuclei expressing H2B-GCaMP8s based on motion-corrected average plane images using the `cellpose` trained neural network algorithm (Stringer et al., 2021) with the parameters `[model_type = 'cyto', diameter = 12, cellpose_flow_threshold = 0.95]`. Based on these segmented masks, we extracted single-cell calcium dynamics from the stimulus-aligned data for every detected cell. We calculated $\delta F/F_0 = (F - F_0)/F_0$ for each segmented cell by taking the mean of the calcium signal traces during 0% coherence stimulation of stimulus-aligned single-cell traces as the F_0 baseline in each trial. We also calculated a normalized version of every cell's calcium response $\Delta F/F_{0\text{normalized}} = \frac{\Delta F/F - \bar{\Delta F}/\bar{F}}{\sigma \Delta F/F_0}$ where $\sigma \Delta F/F_0$ is the standard deviation of $\delta F/F_0$ across the response and $\bar{\Delta F}/\bar{F}$ is the mean $\delta F/F_0$ across the response.

Preferred and non-preferred motion response: The responses of motion responsive cells were categorized as

either preferred motion responses (PMR) (Fig 1f, cell a 1st column) or non-preferred motion responses (NPMR) (Fig 1f, cell a, 2nd column) in response to RDMS stimulation. Motion-responsive cells in the left hemisphere generally respond to leftward random dot motion stimuli (RDMS-L) with positive dynamics PMR and neutrally or negatively to leftward random dot motion stimuli (RDMS-R) (NPMR) and vice versa in the right hemisphere.

Mapping to Reference Brain: To make the locations of cells within the brain comparable between larvae, we mapped the coordinates of segmented cells to a reference brain (z-brain atlas (Randlett et al., 2015)) using Advanced Normalization Tools (ANTs) (Avants et al., 2015). For this, we used the following command with the z-brain as the fixed component and the average image stack as the moving component,

```
[${ANTs_bin_path}/antsRegistration -v 1 -d 3 --float 1 --winsorize-image-
← intensities [0.005, 0.995] --use-histogram-matching 0 -o ${
← temp_transformation_path} --initial-moving-transform [${fixed_path}, ${
← moving_path}, 1] -t Rigid[0.1] -m MI[${fixed_path}, ${moving_path}, 1, 32,
← Regular, 0.25] -c [1000x500x250x300, 1e-8, 10] -s 3x2x1x0 -f 12x8x4x2 -t
← Affine[0.1] -m MI[${fixed_path}, ${moving_path}, 1, 32, Regular, 0.25] -c
← [1000x500x250x300, 1e-8, 10] -s 3x2x1x0 -f 8x4x2x1 -t Syn[0.05, 6, 0] -m CC[{
← fixed_path}, ${moving_path}, 1, 4] -c [100x70x50x20, 1e-8, 10] -s 3x2x1x0 -f 6
← x4x2x1]
```

We concatenated the generated transforms with the following command into one cohesive matrix.

```
[${ANTs_bin_path}/antsApplyTransforms --float -v 1 -d 3 -r ${fixed_path} -i ${
← moving_path} -n linear --transform ${temp_transformation_path}1Warp.nii.gz
← --transform ${temp_transformation_path}0GenericAffine.mat -o [${
← transformation_prefix}.nii.gz, 1]
```

In addition we also did the same with inverse transforms to enable the application of our transformation maps to single points.

```
[${ANTs_bin_path}/antsApplyTransforms --float -v 1 -d 3 -r ${moving_path} -i ${
← fixed_path} -n linear --transform [${temp_transformation_path}0
← GenericAffine.mat, 1] --transform ${temp_transformation_path}1InverseWarp.
← nii.gz -o [${transformation_prefix}_inverse.nii.gz, 1]]
```

To map our average image stack to the Z-brain, we applied the generated concatenated transforms with the following command.

```
[${ANTs_bin_path}/antsApplyTransforms --float -v 1 -d ${ANTs_dim} -i ${
← moving_path} -r ${fixed_path} -n linear --transform ${
← transformation_prefix}.nii.gz -o ${output_path}]
```

We also mapped segmented cells coordinates to the Z-brain atlas using the following command while passing the points as a CSV array.

```
[${ANTs_bin_path}/antsApplyTransforms --float -v 1 -d 3 -i ${moving_path} -r
← ${fixed_path} -n linear --transform ${transformation_prefix}_inverse.
← nii.gz -o ${output_path}]
```

1.2.5 Neural Response Analysis

Quantification of cell responses using Z-test: To quantify if cells responded significantly differently to one stimulus than an opposing stimulus, we applied the two-sample Z-test for comparing two means over time.

$$Z(t) = \frac{\bar{X}_1 - \bar{X}_2}{\sqrt{\frac{s_1^2}{n_1} + \frac{s_2^2}{n_2}}}$$

Within this, \bar{X}_1 is defined as the mean calcium dynamic over trials of a target single cell in response to the target stimulus and \bar{X}_2 being the mean dynamic of the response of the in response to the non-target stimulus. $s_{1,2}$ is the standard deviation across trials for a certain time point while $n_{1,2}$ being the number of repeated stimulus presentations. Applying these calculations to neural traces yields an array of the length of the stimulus. We then selected the 90th percentile, as a stability measure, of this z-score array from trial start till 100% coherence stimulation stop and therefore provided the z-score assigned to the cell. Since we interpolated neural responses to dt=0.5s, this includes 100 time points. The comparison of 100 time points set the significance value to 3.3 after applying the Bonferroni correction.

Direction-Selective Neuron Classification: We define direction-selective neurons as cells with a high z-score in response to RDMS-L or RDMS-R. To select direction-selective neurons, we take the 99th percentile of all z-scores of all cells in response to RDMS-L and the 99th percentile of all cells in response to RDMS-R and select cells with z-scores that show a z-score higher than its corresponding 99th percentile value. This can be formalized as pseudocode, with Z being the z-scores of all cells

$$\begin{aligned} Z_{thresholdRDMS-L} &= \text{Percentile}(Z_{RDMS-L}, 99) \\ Z_{thresholdRDMS-R} &= \text{Percentile}(Z_{RDMS-R}, 99) \\ Z_{directionselective} &= Z[(Z \geq Z_{threshold RDMS-L}) \vee (Z \geq Z_{threshold RDMS-R})] \end{aligned}$$

\vee – selection

this *or-selection* can be extended to

$$\begin{aligned} Z_{directionselective} &= Z[(Z \geq Z_{threshold RDMS-L}) \wedge (Z \geq Z_{threshold RDMS-R})] \\ \wedge &- selection \end{aligned}$$

This allows us to select for cells that negatively respond to their NPMR.

Logical selection of rebound cells: To identify dynamic threshold neurons, also called rebound neurons, within our cell response library we established logical rules. These rules are based on the defined dynamic threshold neuron dynamics as found by Bahl and Engert, 2020, and selection is based on the mean of their responses in certain intervals related to the presented stimulus. For the PMR of rebound cells, we defined these intervals as:

- i1 - second 0 to second 10 of stimulus presentation
- i2 - second 15 to second 40 of stimulus presentation
- i3 - second 50 to second 60 during stimulus presentation

Relating this to the phases of stimulus presentation, i1 represents the prestimulus 0% coherence dot motion during which rebound cells should not show a response; i2 represents the neural response after 100% coherence onset, during which rebound cells should show transient high activity; i3 represents post-stimulus activity in which rebound cells should return to baseline activity. For the NPMR of rebound cells, we defined these intervals as:

- i4 second 0 to second 10 of stimulus presentation
- i5 second 15 to second 40 of stimulus presentation
- i6 second 50 to second 60 during stimulus presentation

In the NPMR, i4 again represents the baseline activity before 100% coherence onset. i5 represents the interval during 100% coherence stimulus presentation in which the cells should go down in their activity, and i6 represents the interval in which rebound cells should perform the characteristic rebound dynamic. We performed logical operations by averaging over these intervals in the neural responses of cells. A PMR of a cell is classified as a rebound dynamic response when (Fig. 2a):

$$(i\bar{1} < i\bar{2}) \wedge (i\bar{3} < i\bar{2})$$

The NPMR of a cell is classified as a rebound dynamic when (Fig. 2b):

$$i\bar{6} > i\bar{4} > i\bar{5}$$

When PMR and NPMR fulfill their complementary conditions, we select a neuron as a rebound cell.

DBSCAN cluster identification: To create clusters from sparse distributions of selected cells across the reference brain, we performed distance-based DBSCAN clustering. This enabled us to separate clusters within metric maps and the selected cells during logic cell selection. We used the sklearn (Pedregosa et al., 2011) implementation of DBSCAN. DBSCAN operates on two major parameters: ϵ , a radius that determines the neighborhood of a datapoint, and `min_samples`, the minimum number of points to form a cluster. Each data point is categorized as a core point, a border point, or a noise point. Core points possess at least the amount of `min_samples` data points within their ϵ . Border points are located in the ϵ neighborhood of another point but do not have `min_samples` within their own ϵ . Noise points are not in the ϵ of a core point. A cluster is only formed when at least one core point is part of the cluster. We applied DBSCAN on the brain-mapped centroids of cells to identify clusters in 3D space from sparse cell distributions. This three-dimensional clustering is an advantage over manual classification since humans are notoriously bad at inferring 3D structures from 2D displayed data. When applying DBSCAN on the logic-selected cells, we used $\epsilon = 12$ and `min_samples = 4`. For the application on the distribution of the nearest neighbor cross correlation metric (nn-CC), we set $\epsilon = 12$ and `min_sample = 5`. For the application on the distribution of the nearest neighbor mutual information metric (nn-MI) metric, we set $\epsilon = 10$ and `min_sample = 4`. We adjusted ϵ and `min_sample` of the nearest neighbor metrics to receive the same number of clusters for both metrics to make results comparable.

Autocorrelation metric: The autocorrelation metric shows how reliably a cell reacts across multiple trials of presentation of the same stimulus. We calculated the autocorrelation metric by cross-correlating each single trial of a neural response, using the `corrcoeff` function of numpy (Harris et al., 2020), and averaging the resulting cross-correlation matrix. This was repeated for every neural response of each cell.

Standard deviation metric: The standard deviation metric combines the reliability and responsiveness of a specific cell to a selected stimulus. We calculated the standard deviation metric by dividing each neural response of each cell with the average standard deviation of the same neural response across trials.

Crosscorrelation to mean metric: The crosscorrelation to mean metric is a way to gauge how well the average of a cell's neural response represents the single-trial neural responses of this cell. For every single trial of stimulus

responses, we calculated the crosscorrelation, using the `corrcoef` function of numpy (Harris et al., 2020). We received the crosscorrelation to the mean metric by averaging these single-trial correlations.

Mutual information with stimulus metric: Mutual information quantifies the information that knowing the value of one variable provides about the other variable, considering linear and non-linear relationships. The mutual information with stimulus metric is a metric that represents how much mutual information a cell's complete experiments neural trace possesses about stimulus identity. First, we discretized the presented stimulus into three values (0 = 0% coherence, -1 = 100% coherence to the left, 1 = 100% coherence to the right). Next, we extracted each cell's complete unaltered neural responses of each cell from our imaging data and assigned each timepoint of neural responses a presented stimulus. To receive the mutual information with stimulus metric, we calculated the mutual information between the whole experiment calcium trace and the corresponding stimulus trace using the `mutual_info_regression` function of sklearn (Pedregosa et al., 2011).

Nearest neighbor metrics: The nearest neighbor-based metrics can assess how a cell's neural response relates to the neural responses of its physical closest neighbors. This is based on the assumption that functional clusters exist within local physical space. After \vee -selecting cells with a 99th percentile, we calculated the three nearest neighbors of all selected cells using the `NearestNeighbors` function of sklearn (Pedregosa et al., 2011). Pearson correlation coefficient, using the `corrcoef` function of numpy (Harris et al., 2020), is then used to correlate the normalized neural response of the target cell to RDMS-L with each of its three nearest neighbors normalized responses to RDMS-L. Averaging these cross-correlations yields the nearest neighbor correlation coefficient nn-CC. Pearson's correlation coefficient quantifies the linear codependencies between two series. It works by dividing the covariance of two variables by the product of the variable's standard deviation. We also calculated the mutual information for the target and nearest neighbors, yielding the nn-MI. To calculate mutual information, we used the `mutual_info_regression` function of sklearn (Pedregosa et al., 2011).

Most similar distance metrics: The most similar distance-based metrics are a good way to assess how far a cell is distanced from the cell with the most similar neural response. For the most similar distance cross-correlation metric (msd-CC), we first calculated the highest correlating partner for each cell based on their neural response to RDMS-L. For the Pearson correlation coefficient calculation, we used the `corrcoef` function of numpy (Harris et al., 2020) and, once identified, then calculated the Euclidean distance in μm between the target cell and its partner, constituting the msd-CC metric. For the most similar distance mutual information metric (msd-MI), we calculated the Mutual information of the target cell with each possible partner based on their neural response to RDMS-L. We calculated mutual information using the `mutual_info_regression` function of sklearn (Pedregosa et al., 2011). Once we identified the partner cell, we calculated the Euclidean distance between the target cell and its partner in μm , constituting the msd-MI metric.

Resampling for Cluster Enhancement: To ensure that we missed no cells displaying similar neural responses to selected cluster responses we resampled our cell library. To resample resulting clusters from the DBSCAN application on logic-selected cells, we first calculated 3D convex hulls with the `Delaunay` function of `scipy` (Virtanen et al., 2020) based on Z-brain mapped cell centroids belonging to the cluster. We then selected all cells from our cell library with Z-brain-mapped cell centroids within these convex hulls. We cross-correlated the normalized NPMR of these selected cells, using the `corrcoef` function of numpy (Harris et al., 2020), to the mean normalized NPMR of the resampled cluster. We added all cells with a Pearson correlation coefficient higher than 0.9 to the cluster.

Metric Maps Creation: We created metric maps to easily represent the distribution of cell dynamic-based metrics in the zebrafish brain. Metrics were mapped on a xy/xz projection of the Z-brain using the Z-brain registered masks of cells. Each cell mask, with the to-be-mapped metric calculated, was coordinate-wise compared to the xy and xz array representing the metric map. If the metric exceeded the currently assigned value of the xy/xz array, at the compared coordinate, we assigned it as the new value at the checked position. We set alpha values to mirror the maximum normalized value of each pixel.

K-means clustering: We used K-means clustering as a way of categorizing cells into unbiased subclusters. We clustered cells based on previously calculated metrics, including msd-CC, msd-MI, autocorrelation metric, Z-score to RDMS-L, CC to mean, MI to stimulus, and the std metric. We normalized every clustered metric of every cell to have a mean of 0 and a standard deviation of 1 using the TimeSeriesScalerMeanVariance function of tslearn (Tavenard et al., 2020). Based on this normalized data, we clustered the cells using the TimeSeriesKMeans function of tslearn (Tavenard et al., 2020) with the parameters [n_clusters = 4, n_init = 1 random_state = 1337]. We decided on n_clusters = 4 based on the elbow method (Umargono et al., 2019) to determine optimal cluster size and resulting cluster evaluation. We applied K-means clustering on the neural dynamic of cells and focused on the stimulus interval, meaning only the neural responses during 100% coherent motion presentation of the PMR of cells. This subselection of the clustered neural responses resulted in 80 features clustered, reducing the dimensionality of the clustered data. We normalized these responses to have a mean of 0 and a standard deviation of 1 using the TimeSeriesScalerMeanVariance function of tslearn (Tavenard et al., 2020) and applied K-means using the TimeSeriesKMeans function of tslearn (Tavenard et al., 2020) with the parameters [n_clusters = 4, n_init = 1 random_state = 1337]. We decided on n_clusters = 4 based on the elbow method to determine optimal cluster size and resulting cluster evaluation.

K-means clustering evaluation: To assess the quality of formed clusters we evaluated each k-means clustering using the common clustering evaluation metrics compactness, separation, and silhouette score. Compactness represents how cohesive a cluster is, indicating how close data points within the cluster are to each other (Milligan & Cooper, 1985). We calculated the compactness as the sum of the Euclidean norm of each point of a cluster $\sum_{i=1}^n \|x_i - c_{k(i)}\|^2$ with x_i being a data point and $c_{k(i)}$ being the center of the cluster x_i belongs to. Summing the summed squared Euclidean norms of each cluster resulted in the compactness of the complete clustering. Separation quantifies the dissimilarity between clusters (Bezdek & Pal, 1998). We calculated separation as the minimum Euclidean distance between cluster centers. Silhouette score combines compactness and separation, thus evaluating clusters by relating their intra-cluster and extra-cluster distances. We calculated the silhouette score using the silhouette_score implementation of scikit learn (Pedregosa et al., 2011)).

Reliability and synchrony according to Bahl and Engert, 2020: We calculated reliability and synchrony like Bahl and Engert, 2020. For calculating the synchrony, we divided the variance over time of the response mean over cells by the mean of the response variance over time of all cells. We calculated trial-to-trial reliability by dividing, per time bin, the absolute mean response over trials by the standard deviation over trials, and then averaged those values during stimulus presentation.

1.3 Results

1.3.1 Expanding the hindbrain integrator circuit

To validate and expand the zebrafish hindbrain integration circuit model (Bahl & Engert, 2020), we conducted two-photon imaging across the entire zebrafish hind- and midbrain while presenting RDMS-L and RDMS-R to the fish (Fig. 1a). Research to date has only described the motion integrator of the larval zebrafish hindbrain with a very narrow spatial resolution in Z. Here, we added volumetric information to the circuit (Fig. 1c). This allowed us to gather more detailed information about the location of neuronal clusters. Furthermore, we can now describe how these clusters functionally compartmentalize. For the functional volumetric imaging, zebrafish were fully restrained in transparent agarose (Fig. 1b) while expressing H2B-GCaMP8s, a calcium-dependent nuclear-localized fluorophore, in most neurons (Fig. 1c). Compared to cytosolic GCaMP8s the nuclear localization of H2B-GCaMP8s ensures an improved segmentability (Fig. 1d). On the other hand, its nuclear localization, H2B-GCaMP8s is thought to have slower dynamics, thus making the neural response more challenging to compare to Bahl and Engert, 2020. Like in Bahl and Engert, 2020, we presented fish with 100% coherence RDMS either to the left (RDMS-L) or right (RDMS-R) (Fig. 1a). We extracted over 200,000 functional responses of individual neurons distributed over 14 fish (Fig. 1i,e).

To quantize this vast amount of cells, we used the two sampled Z-test to compare the two responses of a cell to RDMS-L and RDMS-R (Fig. 1g). We classified cells with a high z-score for a response to a stimulus as direction-selective neurons since their responses are significantly different based on the stimulus direction (Fig. 1f, cell a). Furthermore, their responses are categorizable as preferred motion responses (PMR) (Fig. 1f, cell A, first column). Direction-selective neurons in the left brain hemisphere show PMR to RDMS-L. The same cells exhibit the NPMR when presented with the reversed stimulus (RDMS-R) (Fig. 1f, cell A, second column). The same applies to cells in the right hemisphere, which show PMR to RDMS-R and NPMR to RDMS-L. After establishing our cell library of over 200,000 cells and the establishment of the first metric categorization, we are then able to investigate the motion integrator in the zebrafish larvae in more detail.

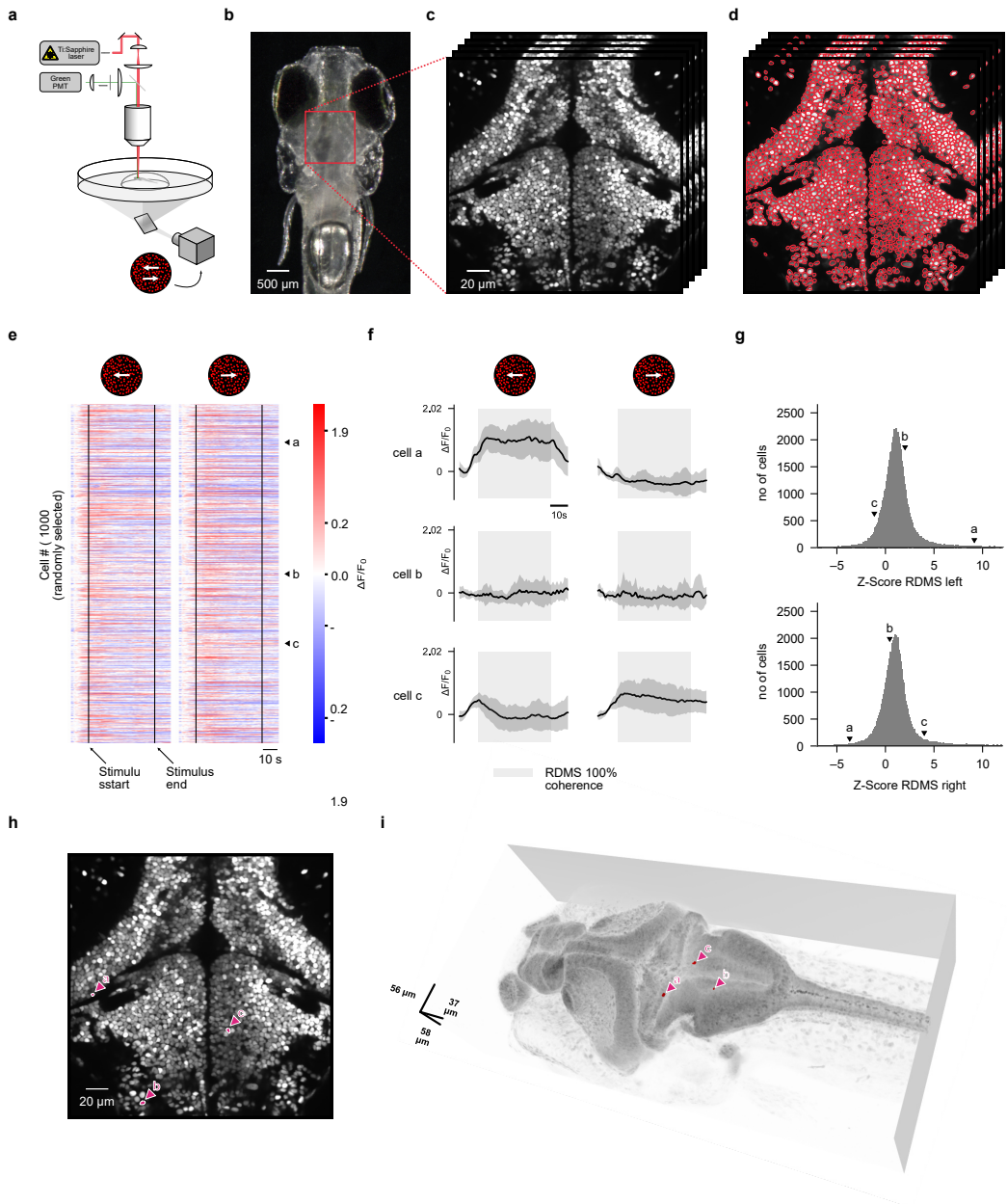


Fig. 1: Two-photon imaging in the mid- and hindbrain of the anterior hindbrain of the larval zebrafish during RDMS presentation. **a**, Schematic of the custom-built two-photon microscope. Fully agarose-embedded 5 dpf zebrafish larvae (no behavior) are presented with random-dot-motion stimuli at 100% coherence from below that either show motion to the left or the right. **b**, Agarose embedded 5 dpf zebrafish larva embedded in agarose photographed using a stereomicroscope. Focal region of two-photon imaging marked with red square. **c**, Volumetric imaged functional two-photon stack of the zebrafish mid- and hindbrain. Imaged region corresponds to **(b)**. **d**, Cellpose segmented volumetric imaged functional two-photon stack of the zebrafish mid- and hindbrain. **e**, 1000 semi-randomly chosen functional dynamics of segmented cells to RDMS-L and RDMS-R. Colormap represents $\Delta F/F_0$ calculated for each individual segmented cell. **f**, Three semi-randomly chosen responses of cell a, cell b, and cell c to RDMS-L and RDMS-R. Cells correspond to letter indications in **(e)**. **g**, Distribution of calculated z-scores for responses to RDMS-L (top) and RDMS-R (bottom) of all cells segmented over 14 fish. Letter indications correspond to same cells as in **(e,f)**. **h**, Locations of cell a, cell b, and cell c in corresponding zebrafish mid- and hindbrain. Letter indications correspond to same cells as in **(e-g)**. **i**, Locations of cell a, cell b, cell c mapped to the z-brain atlas as visualized by Napari. Letter indications correspond to same cells as in **(e-h)**.

1.3.2 Localizing brain-wide distribution of a rare component of the integration circuit

Dynamic threshold neurons were proposed by Bahl and Engert, 2020 to play a critical role in the motion integration network in the larval zebrafish. According to the circuit model proposed by Bahl and Engert, 2020, which portrays the hindbrain integrator as a drift-diffusion model, the dynamic threshold neurons represent a decision threshold that gates the integration circuit from premature readout and, thus, premature behavior output before the circuit gathers enough information. This functionality is portrayed through their transient neural dynamic (Fig. 2a), which Bahl and Engert, 2020 propose acts in a push-and-pull configuration with the integrator neurons. This important proposed role in the network and the cell types' general rarity make them vital to understanding the whole circuit. In addition to their transient PMR, the dynamic threshold neurons also show a poststimulus rebound in their NPMR. Bahl and Engert, 2020 propose this to be a post-inhibitory rebound resulting from the competing circuits located in both hemispheres integrating RDMS-L and RDMS-R. This post-inhibitory rebound is salient and unique compared to other responses in the larval zebrafish brain. Due to the post-inhibitory rebound's uniqueness, we made it one of our primary selection criteria for finding these neurons, thus renaming the dynamic threshold neurons to rebound neurons.

To select these rebound neurons, we first performed 85 percentile z-score \wedge -selection (Fig. 2c) for their PMR and NPMR to receive decently responsive and selective neurons. Instead of classical regressor analysis, we used logical rules that a target cell's neural response had to fulfill. The rules defining a rebound neuron were thus defined based on certain time intervals in the stimulus in which the neural response had to fulfill a set of criteria. To capture the transient dynamic of the PMR, the neural response average in the intervals i1 and i3 (Fig. 2a) had to be lower than the average neural signal in the interval i2 for a neuron to classify as a rebound neuron. Identifying the actual rebound dynamic in the NPMR was defined by the average of interval i4 (Fig. 2b) to be higher than interval i5. In contrast, the average of the interval i6 had to be higher than both of those. Formalized in a formula, we can write this as

$$((i2 > i1) \wedge (i2 > i3)) \wedge (i6 > i4 > i5).$$

After z-score selection and application of logical conditions, we identified 229 potential rebound cells predominantly located in the anterior hindbrain and the pretectum (Fig. 2d). Additionally, these cells exhibited the characteristic dynamic of rebound neurons (Fig. 2e).

Next, we applied DBSCAN on the coordinates of cells within the Z-brain to define clusters of rebound neurons. We defined a neuronal cluster as an assemblage of at least 4 cells that have maximally one additional cell body between their centroid and the centroid of the next member of the cell cluster. Assuming the radius of a larval zebrafish hindbrain neuron to be roughly 6 μm , we set $\epsilon = 12 \mu\text{m}$. Based on these parameters, DBSCAN found four mirror symmetric clusters, three located within the anterior hindbrain and one in the pretectum (Fig. 2f). To increase the number of rebound cells found per cluster, we resampled each cluster. By resampling these regions, we could add cells we missed through limitations with the chosen parameters. This resampling added 139 rebound cells (purple: 33, green: 29, blue: 68, yellow: 9) to our analysis and helped us determine how prevalent the rebound response was in the selected neuronal clusters. The purple cluster correlates with previous studies conducted by Bahl and Engert, 2020 and resembles the most commonly identified transient and rebound dynamics of rebound neurons (Fig. 2g). The other clusters are undocumented as rebound cells but identified as motion responsive (Naumann et al., 2016), and all show volumetric properties that have gained additional information through imaging a larger volume of the whole brain. The green cluster takes the bulbous shape located relatively deep within the pretectum. The blue and yellow clusters are both located medial within the hindbrain but show vastly different cluster shapes. While the yellow cluster also forms a ventral bulbous formation, the blue cluster almost spans the whole ventral-dorsal axis in the posterior part of the hindbrain. Over all areas identified as rebound clusters 5.26% of neurons in all fish showed stereotypical rebound dynamics in PMR and NPMR (purple: 4.11%, green: 6.13%, blue: 5.33%, yellow: 8.75%).

In summary, we were able to reproduce the localization and neural dynamics of rebound neurons described in Bahl and Engert, 2020. In addition, we identified 3 more spatially localized neuron clusters that have previously not been classified as rebound/dynamic threshold neurons. This shows how logical detection of cell types by comparing features of their neural dynamics is a valid method to identify specific cell types.

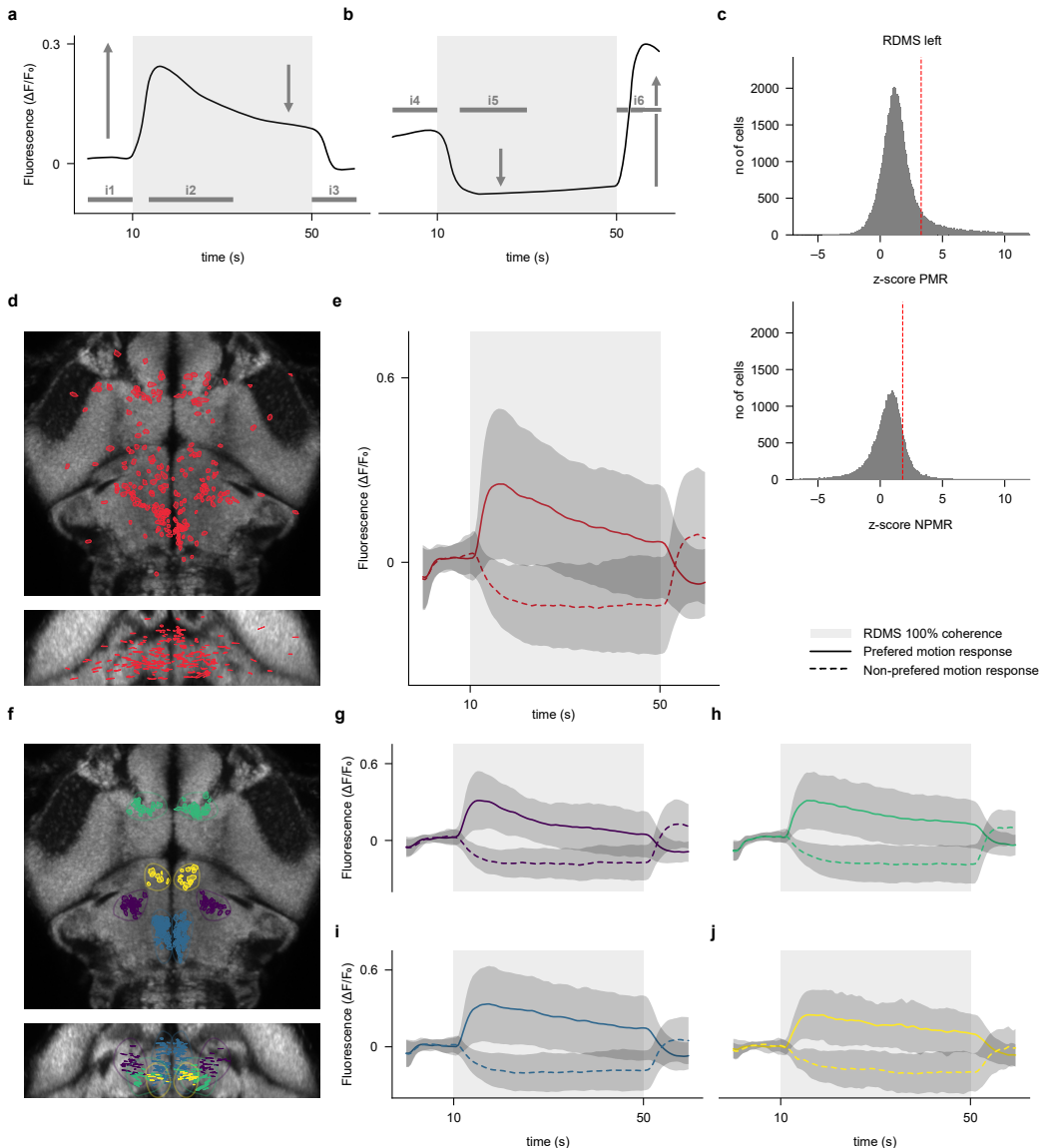


Fig. 2: Logic-based selection reveals spatial clusters of rebound cells. **a**, Schematic illustrating the intervals applied to PMR responses of cells for logic-based selection of rebound cells. Dynamics represent fictional ideal PMR response of a rebound cell. **b**, Schematic illustrating the intervals applied to NPMR responses of cells for logic-based selection of rebound cells. Dynamics represent fictional ideal NPMR response of a rebound cell. **c**, Distribution of calculated z-scores for PMRs (top) and NPMRs (bottom) of all cells segmented over 14 fish. Dotted line represents 85 percentile of z-scores used for \wedge -selection. **d**, Z-projection (top), and y-projection (bottom) of distribution of z-score and logic-selected cells registered to the Z-brain ($n = 229$). Displayed planes correspond to average registered z-coordinate or registered y-coordinate of selected cells. **e**, Average functional dynamics of z-score, and logic-based selected cells. Solid line represents PMR and dotted line represents NPMR. Gray background represents interval of 40s of 100% RDMS presentation. Gray envelope of functional dynamics represents standard deviation across all selected cells for either PMR or NPMR. **f**, Z-projection (top) and y-projection (bottom) of selected cells after DBSCAN application and cell cluster resampling. Colors represent different cluster identities (n , purple = 63, green = 51, blue = 140, yellow = 21). **g-j**, Average functional dynamics of DBSCAN resulting cell clusters. Color represents cluster localization in (f). Solid line represents PMR and dotted line represents NPMR. Gray background represents interval of 40s of 100% RDMS presentation. Gray envelope of functional dynamics represents standard deviation across all selected cells for either PMR or NPMR.

1.3.3 Unbiased responsitivity and reliability metrics of the larval zebrafish hindbrain during the RDMS

After identifying the rebound neurons with a biased method we focused on unbiased methods to analyze the rest of the cell responses in the context of the RDMS. Unlike the logical conditions that we used before, neutral metrics avoid biases and allow us to discover localized clusters and cell types with any type of dynamics. We calculated these neutral metrics for all segmented cells. We again used the mapping of segmented cells onto a reference brain, enabling us to compare cells across individuals and create maps to show metrics across the brain (Fig. 3a).

The metrics describe the responsivity and reliability of cells in response to the RDMS-L but should apply to the RDMS-R in a mirrored manner under the assumption that the motion integrator is mirror symmetric. This hemispherical orientation is prevalently visible in the metric map displaying maximal values of the z-score calculated for the PMR to RDMS-L (Fig. 3a). As established by Bahl and Engert, 2020, the highest values can be found in the anterior hindbrain and a bulbous cluster in the pretectum. Additionally, we identified a salient, very lateral cluster in the eminentia granularis. This metric map of the z-score gives a comprehensive overview of direction-selective PMRs during RDMS-L presentation.

Continuing to understand where direction-selective neurons are located, we examined the autocorrelation metric. Using the autocorrelation metric, we aimed to explore how reliable cells respond to RDMS-L across multiple stimulus trials. The metric map (Fig. 3b) shows an asymmetry that cells in the left hemisphere highly correlate between several trials and thus respond more reliably to RDMS-L than the right hemisphere. Structures like the pretectum bulb and the lateral cluster in the eminentia granularis are discernible and show localized spikes of the metric. Despite this asymmetry, local clusters, like the bulb structure in the pretectum and the anterior hindbrain, show medium to high reliability while performing their NPMR.

To combine the responsivity metric of the z-score and the reliability metric of the autocorrelation metric, we next created a metric map combining both in the form of the standard deviations metric (Fig. 3c). By relating the variation within trials to the variation across trials, we visualized cells that reliably react strongly to the RDMS-L (Fig. 3c). This standard deviation metric highlights 4 regions across the zebrafish brain: the pretectum bulb, the anterior hindbrain, the lateral eminentia granularis cluster, and the posterior hindbrain, thus identifying them as salient clusters of the circuit processing RDMS-L in the zebrafish brain.

Since most of our analysis is on the mean of trials, we wanted to establish a metric representing how well a cell's mean of individual responses represents a single trial response. Mapping this metric to the brain, we can see that even though this was calculated for the RDMS-L (meaning that left hemisphere cells show PMR and right hemisphere show NPMR), the apparent pattern is hemispherical symmetrical. Compared to other metric maps such as z-score, this metric map also shows high values in large parts of the pre-tectum and not only the anterior bulbous formations.

As a last metric, we calculated the mutual information between the neural responses of individual cells and a discretized representation of the presented stimulus (Fig. 3e). The values assigned to cells show how much mutual information and the discretized stimulus array share, thus making this a stimulus-independent metric. Mapping this to the brain, we can see the locations of the brain that deliver the most information about the currently presented stimulus. This metric primarily highlights the medial anterior hindbrain and the bulbous formation in the pretectum as the centers of motion processing. Additionally, it shows several minor regions of interest in the lateral cluster in the eminentia granularis and several small regions of interest in the pretectum and posterior parts of the hindbrain, like the anterior rhombencephalic turning region and the ventromedial spinal projection neurons.

Since many metric maps (Fig. 3a-d) show peak values for the lateral clusters in the eminentia granularis, we were curious about its dynamics. We can further investigate these extraordinary cell clusters by manually subsetting our cell library to only include cells located in this brain area (Fig. 4a). The resulting neural responses show dynamic

threshold-like dynamics with a transient PMR and a strong rebound in the NPMR (Fig. 4b) localized in the eminentia granularis.

Altogether, the metric maps give us an unbiased overview of how cells in different regions of the zebrafish brain respond to the presentation of the RDMS. We confirmed patterns found by Bahl and Engert, 2020 and previously detected with our logic condition cell detection. Additionally, we found very salient cell dynamics in the eminentia granularis (Fig. 4) which is present in almost all of our metric maps. Furthermore, we added a new perspective on the hindbrain integrator circuit and finally, we aimed to formalize metric maps using distance-based metrics into spatial clusters.

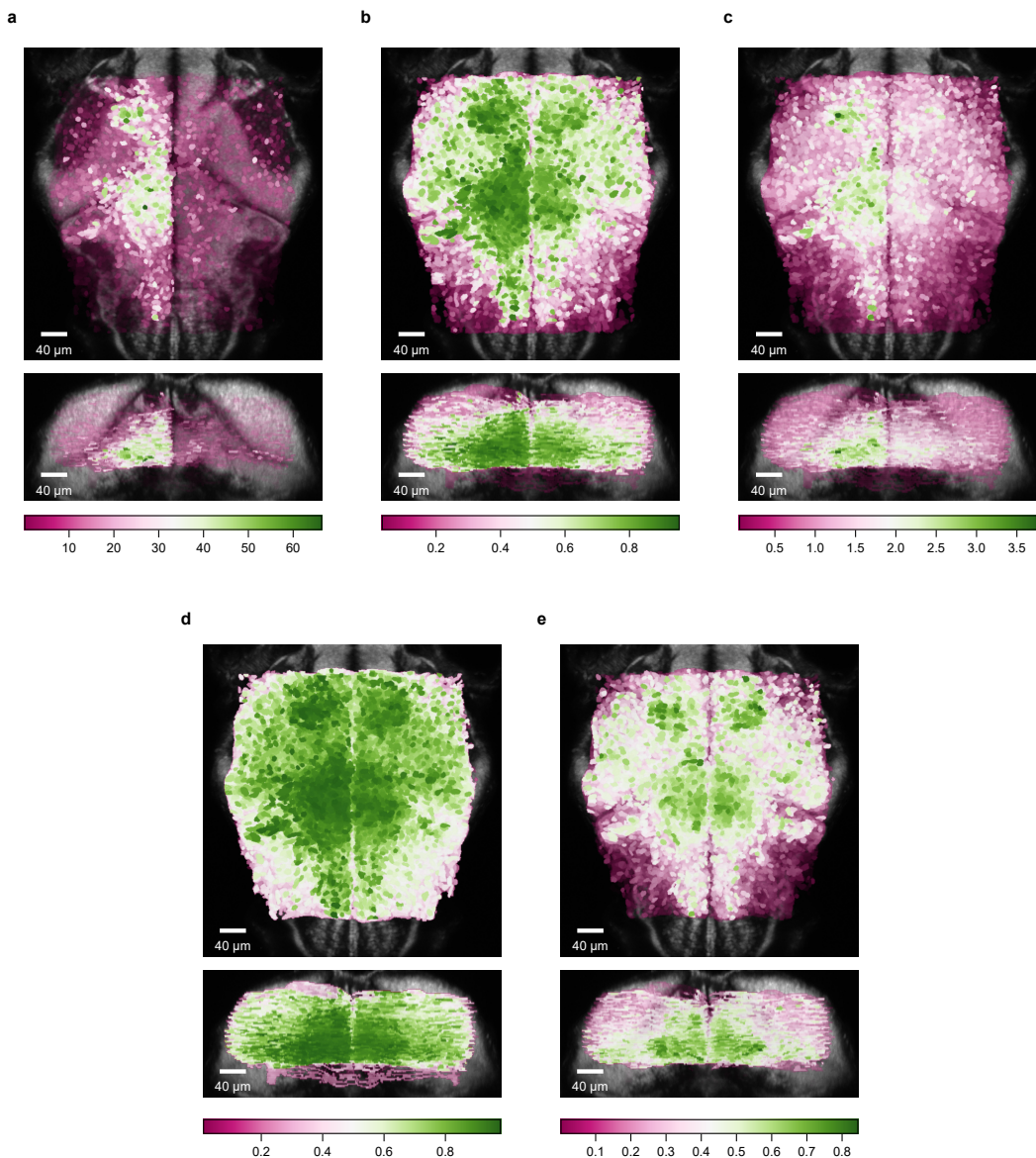


Fig. 3: Metric maps of responsitivity, reliability, and stimulus information across all cells. Maximum value z- (top) and y-projection (bottom) of metric maps visualizing. **a**, z-score in response to RDMS-L. **b**, Autocorrelation metric during RDMS-L. **c**, Standard deviation metric during RDMS-L. **d**, Crosscorrelation metric to mean metric during RDMS-L. **e**, Mutual information with stimulus metric identity. For each pixel in z-projection and y-projection, the maximum metric was calculated based on cells' registered position in the z-brain atlas. Alpha values correspond to cells' metric values. Displayed planes correspond to average registered z-coordinate or registered y-coordinate of selected cells.

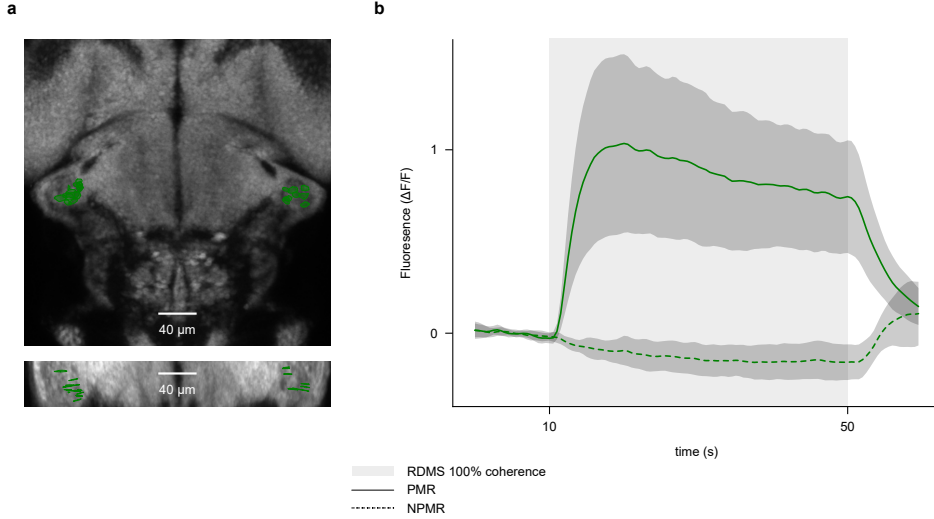


Fig. 4: A lateral cluster in the eminentia granularis. **a**, Z-projection (top) and y-projection (bottom) of the distribution of a lateral cluster in the eminentia granularis identified by the metric maps in Fig. 3b. Functional dynamics corresponding to the cells in the eminentia granularis cluster. Solid line represents PMR and dotted line represents NPMR. Gray background represents interval of 40 s of 100% RDMS presentation. Gray envelope of functional dynamics represents standard deviation across all selected cells for either PMR or NPMR. Displayed planes correspond to average registered z-coordinate or registered y-coordinate of selected cells.

1.3.4 Metric-based cluster detection

Since we predict that functional clusters are close in physical space (Ohki et al., 2005), we designed several metrics that use physical distance in 3D space based on the centroid of cells registered to the z-brain. We used two base approaches to incorporate the distance between cells and neural responses, one being metrics that compare responses of cells and their nearest neighbors and the other being the distance between cells and their most similar partner.

First, we looked at nearest neighbors and compared how well a cell correlates with its three nearest neighbor neurons (Fig. 5a). Since nearest neighbor calculations are computationally costly, we opted to apply 99th percentile \vee -selection on the z-scores of cells' responses to RDMS-L and RDMS-R (red cells in insets in Fig. 5). We looked for their nearest neighbors within the same fish for these preselected cells. We calculated the Pearson correlation coefficient with the responses to RDMS-L of their nearest neighbors. We eventually received the nearest neighbor nn-CC. As a last step, we selected the 90th percent of cells based on their nn-CC metric. The metrics map of nn-CC (Fig. 5a) shows that cells that correlate the most with their neighbors are primarily located in the left hemisphere, performing the PMR to RDMS-L. Furthermore, the pretectum bulb and the medial part of the anterior hindbrain show a high neighbor correlation. Also, the lateral cluster in eminentia granularis mentioned before and a cluster in the locus coreuleus are recognizable. In the right hemisphere, some cells in the location of the purple rebound cluster we detected through logic detection (Fig. 2f) which show a high neighbor correlation, as well as cells that relatively fit the other rebound clusters discussed in Fig. 2f.

We also looked at the mutual information that cells share with their nearest neighbors. We again applied 99th percentile \vee -selection on the z-scores of cells' PMRs and NPMRs (red cells in insets in Fig. 5) and again looked for nearest neighbors of cells within the same fish. We calculated the mutual information cells displayed on average with their 3 nearest neighbors receiving the nn-MI from this. The nn-MI metric map shows a different distribution across the brain than the nn-CC map (Fig. 5.c). Noticeably, the cells in the pretectum bulb cluster in the right hemisphere possess the most information about their neighbors. We also identified a salient small cluster in the stratum periventriculare. However, the metric map shows an equal distribution of cells with high nn-MI across both

hemispheres. The lateral locus coreuleus cluster mentioned before shows a high nn-MI and is easily differentiable.

Next, we looked at the distance between target cells and their most similar cells. This approach is the reversed logic from nearest neighbor analysis, which first looks at distance and then similarity. To match our approach of nn-CC and nn-MI, we first applied 99th percentile \vee -selection on the z-scores of cells' PMRs and NPMRs for their PMR and NPMR. In these preselected cells, we first found the most similar cell of each target cell either by Pearson correlation coefficient or mutual information. Next, we calculated the distance between target cells and their most similar partner. We received the most similar cell distance based on correlation coefficient (msd-CC) and mutual information (msd-MI). As a last step, we selected the 90th percentile of cells for their msd-CC and msd-MI values. These metric maps show an equal distribution across hemispheres of cells with low msd-CC and msd-MI.

The metric map displaying msd-CC (Fig. 5.b) shows that cells close to their highest correlating cell are comparatively medial oriented. In addition, it shows a difference in the anterior-posterior distribution of cells in the left hindbrain hemisphere, where cells are spread across the axis, versus the right hindbrain hemisphere, where cells localize in a denser cluster. The bulbous pretectum formation can be recognized better in the nn-MI metric map (Fig. 5c) than in the msd-MI metric map (Fig. 5d). This metric map also shows less medial and more distributed localization of cells with a low msd-MI. The high symmetry displayed in the msd-MI metric map is reflected in one very lateral pretectum cell visible in both hemispheres.

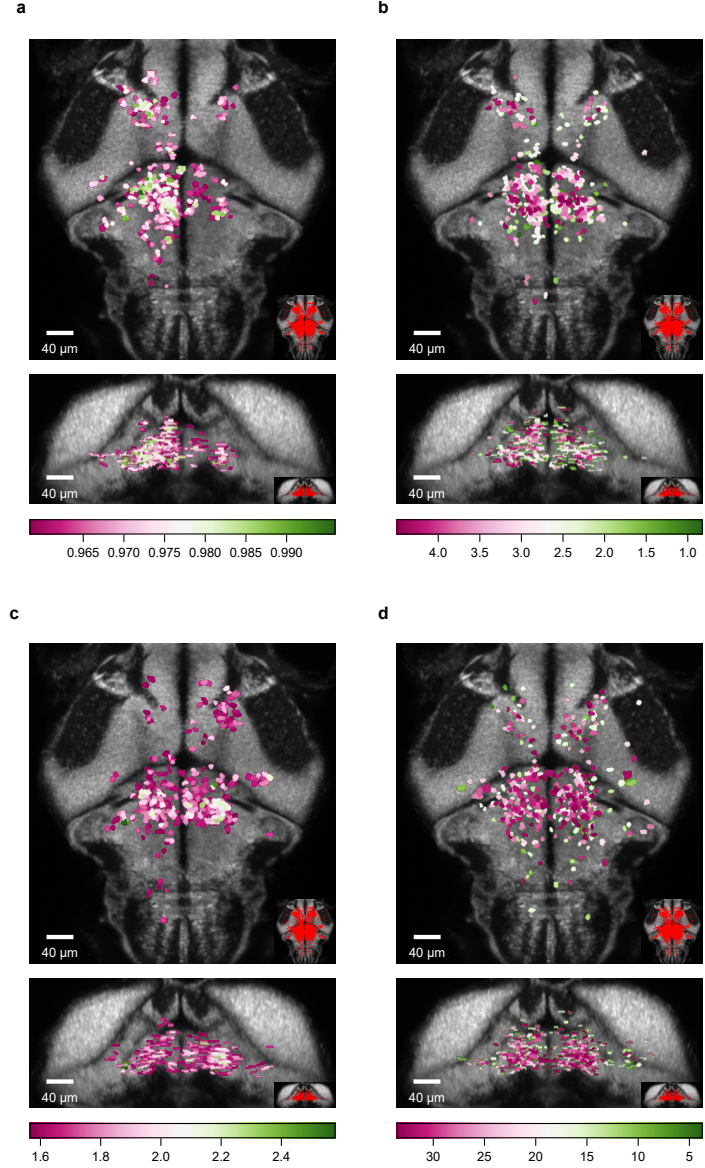


Fig. 5: Metric maps combining distance and activity reveal spatial organization of the motion integration network. Maximum value z- (top) and y-projection (bottom) of metric maps visualizing. **a**, nn-CC during RDMS-L. **b**, msd-CC during RDMS-L. **c**, nn-MI during RDMS-L. **d**, msd-MI during RDMS-L. For each pixel in the z-projection and y-projection, the maximum metric was calculated based on cells' registered position in the z-brain atlas. Alpha values correspond to cells' metric values. Displayed planes correspond to average registered z-coordinate or registered y-coordinate of selected cells. Colormaps in (**b,d**) are reversed since lower values represent a better lower distance in μm to the most similar cell. Cells have been preselected before calculating metrics by 99th percentile \vee -selection on the z-scores of cells' PMRs and NPMRs. The distribution of these preselected cells is visualized by the red cells in the insets of (**a-d**).

1.3.5 DBSCAN-based cluster formation

To form segregated clusters of the cells in the metric maps of nn-CC (Fig. 5a) and nn-MI we used DBSCAN. While applying DBSCAN to nn-CC, we chose $\epsilon = 12 \mu\text{m}$ and set the minimal cluster size to 5 cells. DBSCAN returned 14 different clusters (Fig. 6a) with varying neural dynamics, which enabled us to look at potential functional clusters emergent from the nn-CC metric. The blue cluster comprises most of the medial anterior hindbrain (Fig. 6a) and shows a moderately fast-rising PMR (blue solid line in Fig. 6b) and small NPMR (blue dotted line in Fig. 6b). The pink cluster representing the visually salient lateral cluster in the locus coreuleus demonstrates a slowly rising PMR. In contrast, the green cluster in the pretectum shows a quick PMR and a strong rebound in the NPMR. The small red

cluster at the boundary of the anterior hindbrain and pretectum shows a strong and slow PMR with a comparatively small NPMR.

For the application of DBSCAN to the nn-MI metric map we chose $\epsilon = 10 \mu\text{m}$ and a minimal cluster size of 4 cells. We chose these parameters to match the number of clusters produced by the application of DBSCAN on nn-MI. The application of DBSCAN on nn-MI produced a similar cluster to the red cluster in Fig. 6a-b in the form of the yellow cluster in Fig. 6a-d. This shows how both metrics (nn-CC and nn-MI) partially produce the same clusters even though they are created through different methods. After we ran DBSCAN on the nn-MI metric map, we identified a preliminary cluster similar to the blue one in Fig. 6a but with incoherent neural dynamics. To solve this problem, we split the incoherent clusters by k-means clustering on the neural response to RDMS-L and RDMS-R. This resulted in two new clusters with differentiated neural dynamics. The first of these clusters is the red lateral anterior hindbrain cluster, which shows a slowly rising PMR and a weak NPMR. The other created cluster, the blue cluster, is located more medial in the anterior hindbrain and shows rebound dynamics in PMR and NPMR. The last orange cluster presents as a pretectal cluster with a fast but weak PMR and almost similarly strong NPMR.

Summarizing this we find cells in the anterior hindbrain as described by Bahl and Engert, 2020, suggesting a close functional clustering of integrator and rebound neurons. Furthermore, we identify a cluster of cells in the right pretectum responding to RDMS-L and RDM-R previously assumed to show PMRs (Naumann et al., 2016) and a motion-responsive cluster with slow dynamics in the locus coreuleus.

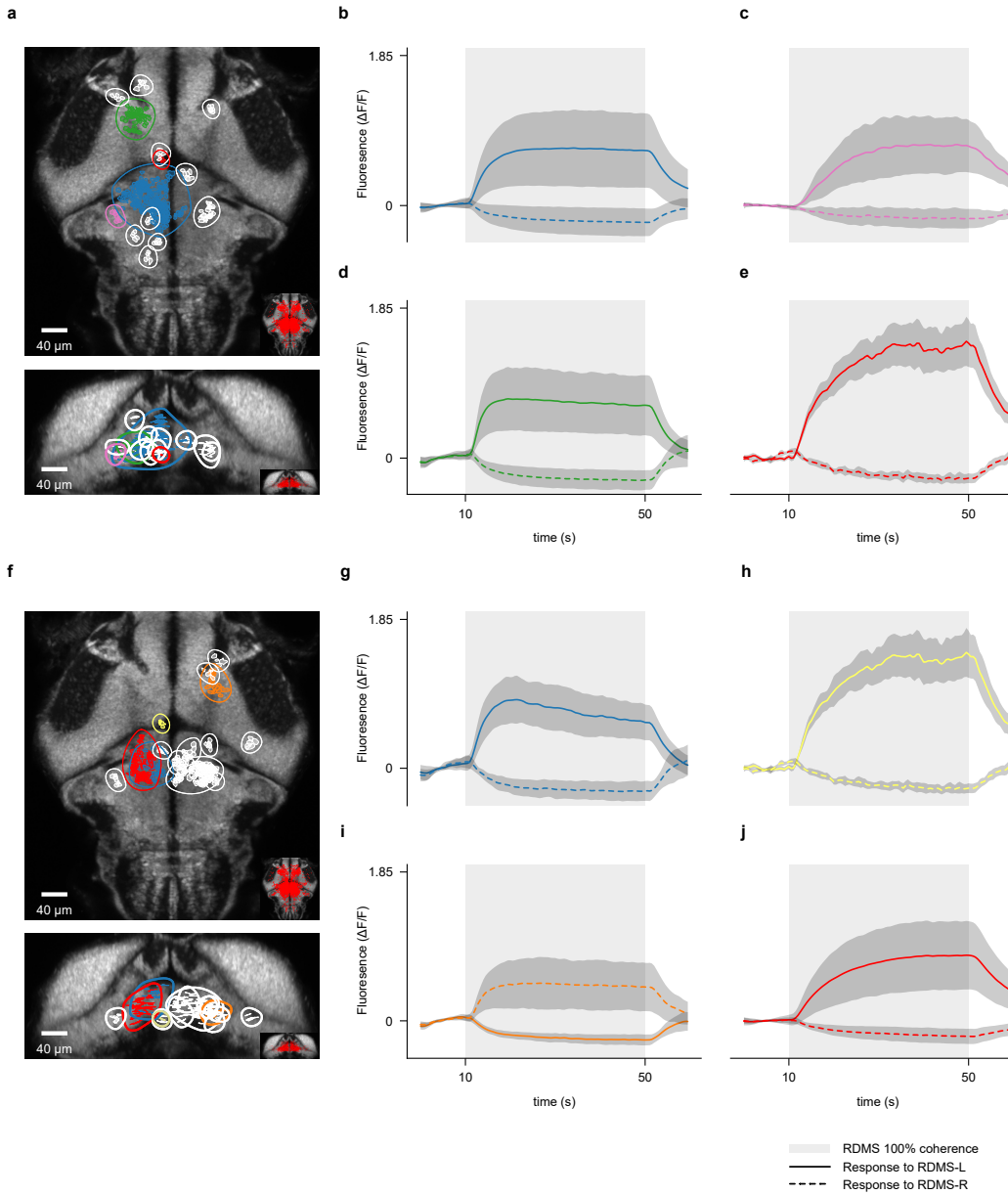


Fig. 6: DBSCAN clustering of density-based metrics highlights various functional clusters. **a**, Z-projection (top) and y-projection (bottom) of selected cells after DBSCAN application to nn-CC metric map (Fig. 5a). Colors represent different cluster identities while white clusters are not further analyzed (n, blue = 101, pink = 7, green = 47, red= 5). **b-e** Average functional dynamics of cell clusters resulting from DBSCAN application on nn-CC metric map (Fig. 5a). Color represents cluster localization in **(a)**. Solid line represents neural responses to RDMS-L and dotted line represents neural responses to RDMS-R. Gray background represents interval of 40s of 100% RDMS presentation. Gray envelope of functional dynamics represents standard deviation across all selected cells for either response to RDMS-L or RDMS-R. **f**, Z-projection (top) and y-projection (bottom) of selected cells after DBSCAN application to nn-MI metric map (Fig. 5c). Colors represent different cluster identities, while white clusters are not further analyzed (n, blue = 24, yellow = 5, orange = 20, red = 76). **g-j**, Average functional dynamics of cell clusters resulting from DBSCAN application on nn-MI metric map (Fig. 5c). Color represents cluster localization in **(f)**. Solid line represents neural responses to RDMS-L and dotted line represents neural responses to RDMS-R. Gray background represents interval of 40s of 100% RDMS presentation. Gray envelope of functional dynamics represents standard deviation across all selected cells for either response to RDMS-L or RDMS-R.

1.3.6 Revealing structure in the zebrafish brain by k-means clustering cell metrics

Clustering cells using k-means is a common unbiased approach to categorizing cells based on their characteristics. Since clustering gets more opaque with increasing dimensions, we used clustered our created metrics from the previous chapter. Through this dimensional reduction, we aim to maximize the interpretability of the differences in cells without relying on the emergence of differences in neural dynamics between the resulting clusters.

We excluded nn-CC and nn-MI since we only calculated these metrics for parts of the available data due to high computational costs. Since many cells make it more challenging to recognize structure within this data, we still decided to apply 99th percentile \vee -selection on the z-scores of cells' PMRs and NPMRs.

We used the K-means algorithm with 4 clusters, which we determined as an optimal cluster size based on the elbow method, personal experience, and the analysis of resulting clustering results. The returned clusters showed visible structural differences (Fig. 7a-d) but no emergent differing neural dynamics (Fig. 7e).

The blue cluster (Fig. 7a) presents a symmetrical formation across both hemispheres, including the bulbs in the pretectum and some lateral and very posterior locations in the hindbrain. The highest density of the blue cluster is in the anterior hindbrain.

The red cluster (Fig. 7b) is located primarily in the right hemisphere, with only a few cells in the left hemisphere. This laterality includes the often identified aggregations of cells in the pretectum, the anterior hindbrain, and the lateral locus coreuleus and eminentia granularis cluster. In the right hemisphere, k-means identifies only a small amount of cells located exclusively in the anterior hindbrain.

The pink cluster (Fig. 7c) shows asymmetry towards the left hemisphere. The pink cluster cells reside in the anterior hindbrain, pretectum, the posterior parts of the hindbrain, and in the lateral locus coreuleus and eminentia granularis clusters. Despite its laterality, a population of cells in the pretectum bulb of the right hemisphere also contributes to the pink cluster.

The cyan cluster (Fig. 7d) shows a symmetric distribution across both hemispheres. Unlike the other resulting clusters, the cyan group does not contain cells in the pretectum bulb but only in the medial parts of the pretectum. In the anterior hindbrain, cyan cluster cells show a more laterally spread distribution than cells in other clusters. In the region of the ventromedial spinal projection cluster, part of the anterior hindbrain, the cyan cluster shows a distinct lack of cells, differentiating it even more from the other clusters. Compared to the red and pink clusters, it also contains fewer cells belonging to the lateral locus coreuleus and eminentia granularis clusters.

We calculated compactness, separation, and silhouette score to evaluate clustering quality. A cluster's compactness score shows how closely a cluster's single data points are to each other in metric space. The separation score shows how well separated the resulting clusters are, and the silhouette score shows how well a data point fits into its assigned cluster compared to other clusters. Comparing these metrics to the same data with shuffled cluster identities shows good scores for all three metrics, indicating a good clustering result.

Furthermore, to understand which metrics were responsible for cluster separation, we looked at the average values of the resulting clusters normed by maximum metric values in the data (Fig. 7i). This analysis highlights the correlation coefficient of single trials to the mean and the mutual information about the stimulus presented as the differentiating metric for the cyan cluster.

The pink cluster separation is visible in msd-MI, showing that cells in this cluster have, on average, a lower distance to their most informative other cell.

The blue cluster separates most in the correlation coefficient to the cell's mean trial, the std intra/std extra metric,

and the z-score, which shows that the blue cluster separates through its lower average responsibility and reliability. Except for these metrics, the red cluster shows close homogeneity with the blue cluster. Combined with the high compactness scores (high values mean less compact) of the red and blue clusters, this is the worst clustered group in this analysis.

Overall, we show that from clustering reliability, responsiveness, stimulus mutual information, and activity metrics alone structure arises from the cells located all over the zebrafish brain. We hereby highlight the red and pink clusters which seem to be mirror-symmetric clusters and separate through reliability and responsitivity. These clusters also show cells in the eminentia granularis which appears to be a common thread going through our analysis.

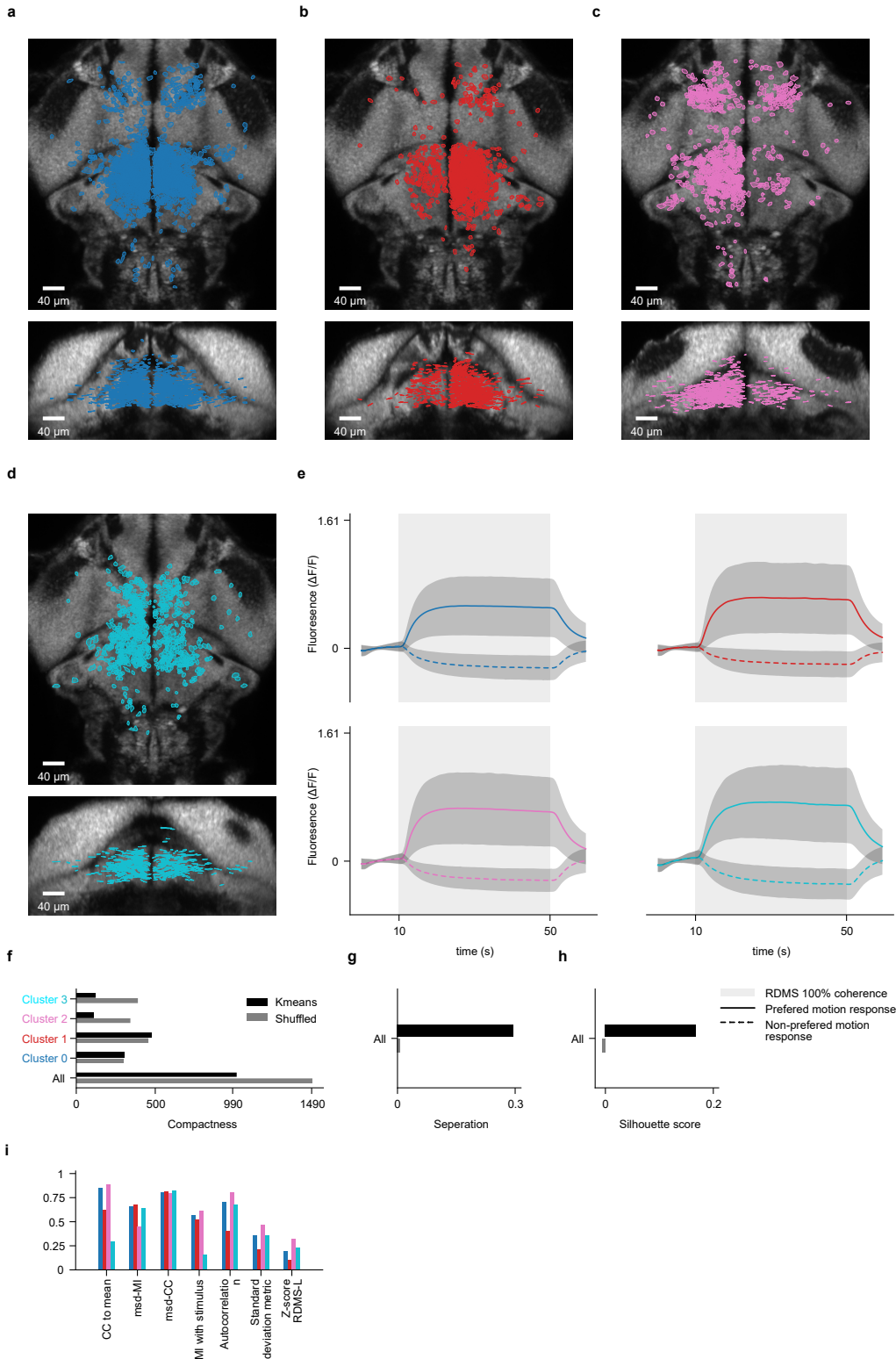


Fig. 7: K-means clustering of cells based on responsitivity, reliability, and stimulus information metrics. **a-d**, Z-projection (top), and y-projection (bottom) of resulting clusters from k-mean clustering of metrics quantizing responsitivity, reliability, and stimulus information. Displayed planes correspond to average registered z-coordinate or registered y-coordinate of selected cells. **e**, Average functional dynamics of cell clusters resulting from k-means clustering. Color represents cluster localization in (a-d). Solid line represents PMR and dotted line represents NPMR. Gray background represents interval of 40s of 100% RDMS presentation. Gray envelope of functional dynamics represents standard deviation across all selected cells for either PMR or NPMR. **f**, Quantification of cluster compactness compared to shuffled cluster identities. **g**, Quantification of cluster separation compared to shuffled cluster identities. **h**, Quantification of cluster silhouette score compared to shuffled cluster identities. **i**, Normalized average metric values per cluster.

1.3.7 Revealing structure in the zebrafish brain by clustering RDMS neural response dynamics

Since using k-means on our generated metrics only unveiled structural differences but no varying neural dynamics, we decided to apply k-means to our available neural dynamics. To reduce the dimensionality of the data, we only selected the cell responses of PMRs and NPMRs during 100% coherence RDMS stimulation. This selection reduced the clustered data by 33%. We again applied 99th percentile \vee -selection on the z-scores of cells' PMRs and NPMRs. After preselection, we ran the K-means algorithm with a cluster size of three, determining this through elbow optimization and analysis of the output clusters. The resulting clusters (Fig. 8a-c) showed low structural differences but striking variations in their average neural dynamics. All clusters show a symmetrical distribution over the brain. Cells of the red cluster in the pretectum can be found in an anterior bulb and a posterior medial position (Fig. 8a). In the anterior hindbrain, the red cluster shows an equal distribution with lateral localizations in more posterior parts and localizations in the very lateral locus coreuleus and eminentia granularis clusters. A few cells of the red cluster also localize in very posterior parts of the hindbrain.

The purple cluster (Fig. 8b) shows fewer cells in the anterior pretectum bulb and medial parts of the posterior pretectum than the red cluster. In the anterior hindbrain, the purple cells show an equal distribution shifted more anteriorly than the red cluster. The purple cluster does not contain cells in the mentioned lateral eminentia granularis cluster but few in the locus coreuleus cluster. The cyan group (Fig. 8c) shows a similar distribution in the pretectal bulb like the red cluster, but misses medial pretectum cells in the posterior pretectum except in a very localized spot in the left, posterior end of the pretectum. In the anterior hindbrain, cyan cells show a medial-lateral gradient with a high density of cells close to the midline and a lesser density to lateral parts. In contrast to the purple cluster, Cyan cells possess cells in lateral localization in the lateral eminentia granularis cluster but not in the locus coreuleus cluster. Furthermore, the cyan cluster forms an uncanny bow/circle formation in the posterior part of the anterior hindbrain, recognizable in both hemispheres. These localizations are probably attributable to registration artifacts. Beyond these structural localizations, clustering on neural dynamics produced clusters (Fig. 8e) with much more variation in their neural responses than the cell aggregations produced through metric clustering (Fig. 7e).

The red cluster shows a PMR with a fast neural response and a discernable NPMR. Compared to the red cluster, the purple cluster (Fig. 8f) shows a PMR with a much higher time constant and a very weak NPMR. The average neural response of the cyan cluster shows a PMR with a weak transient characteristic and a rebound-like NPMR. Since the resulting three clusters showed high similarity to the functional cell types presented in Bahl and Engert, 2020), we decided to recreate their reliability vs. cluster synchrony plot (Fig. 8i). According to this analysis, we found out that our resulting clusters segregated according to these features, with the cyan cluster placing the lowest and the purple cluster placing the highest. To evaluate the quality of the k-means clustering, we calculated compactness for every cluster and separation and silhouette for all clusters together. Each cluster and all clusters together show a compactness not noticeably different from shuffled data, resulting from clustering high dimensional data. The silhouette score indicates a separation worse than shuffled data, representing the fluidity between the single-cell responses, illustrating that cells do not operate in well-defined neural classes but are a continuum of varying neural responses. Conversely, the clustering shows a high separation, quantizing the clusters' visibly different neural response mean of the clusters (Fig. 8e-g).

Overall, the K-means clustering of PMR neural responses during stimulus presentation results in the functional cell classes proposed by Bahl and Engert, 2020. These functionally separated resulting clusters show differing localizations over the zebrafish brain. Hereby, the cluster evaluation metrics of the clustering show characteristics of three functionally separated cell types with fluid intermediate neural responses.

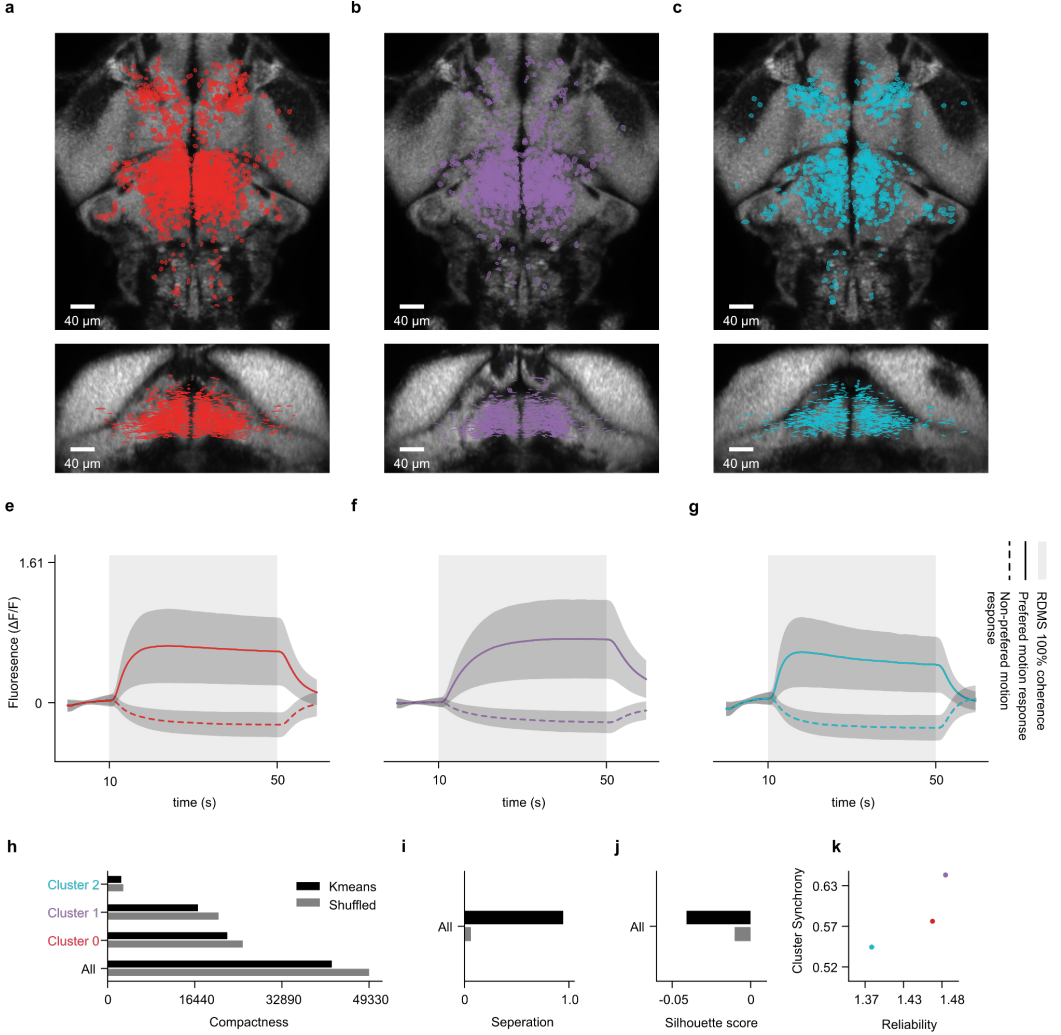


Fig. 8: K-means clustering of neural responses finds established functional classes of the motion integrator. **a-c**, Z-projection (top), and y-projection (bottom) of resulting clusters from k-mean clustering of PMRs during stimulus presentation. Displayed planes correspond to average registered z-coordinate or registered y-coordinate of selected cells. **e-g**, Average functional dynamics of cell clusters resulting from k-means clustering. Color represents cluster localization in **(a-c)**. Solid line represents PMR and dotted line represents NPMR. Gray background represents interval of 40s of 100% RDMS presentation. Gray envelope of functional dynamics represents standard deviation across all selected cells for either PMR or NPMR. **h**, Quantification of cluster compactness compared to shuffled cluster identities. **i**, Quantification of cluster separation compared to shuffled cluster identities. **j**, Quantification of cluster silhouette score compared to shuffled cluster identities. **k**, Trial-to-trial reliability plotted against cluster synchrony for each cluster adapted from Bahl and Engert, 2020.

1.4 Discussion

Here, we further explored the neuronal dynamics and localizations of the functional components of the motion hindbrain integrator in the larval zebrafish Bahl and Engert, 2020. We employed biased logical identifications of cells by their neural dynamics based on salient neural dynamic characteristics sourced from Bahl and Engert, 2020. Furthermore, we employed unbiased metrics, characterizing neural dynamics regarding reliability, responsiveness, and inter-cell relationships. We related these metrics to their physical locations within the brain, leveraging the opportunity of mapping cells to a reference brain (Z-brain (Randlett et al., 2015)). We applied clustering algorithms in physical, metric, and neural dynamic space to uncover functional clusters across the larval zebrafish's brain.

1.4.1 Logic-based selection identifies several loci of rebound neurons

In our logic-based selection approach, we recaptured the dynamics and localization of dynamic threshold neurons from Bahl and Engert, 2020 as the purple cluster in Fig. 2f. This purple cluster is strongly similar in its neural dynamics (1.2g) to the dynamic threshold cells' neural dynamics of Bahl and Engert, 2020. We also identified three other clusters with strong rebounds in their NPMRs but differences in their PMRs compared to Bahl and Engert, 2020. These logic-selected cell clusters are located in medial parts of the posterior anterior hindbrain (blue cluster Fig. 2f), in a bulbous cluster in the anterior pretectum (green cluster Fig. 2f), and in the Oculomotor nucleus nIV (yellow cluster Fig. 2f). All these clusters show distinct localization across the z-axis, highlighting the benefits of our volumetric approach to imaging.

The newly identified dynamic threshold clusters in the anterior hindbrain show variance in the transiency of their PMRs while retaining similar NPMRs. Bahl and Engert, 2020 proposed the post-inhibitory rebound to represent inhibition through a contralateral mirror symmetric circuit primed to the opposite stimulus. Although the observed differences in PMR could potentially be explained by the nuclear localization of H2B-GCaMP8s, we consider this option unlikely. Rather, we believe this could be explained by these neurons being the dynamic threshold neurons of other integration networks in the anterior hindbrain optimized for different stimuli than the RDMS. In this case, NPMRs would stay the same since the active circuit, in our case, the motion integration circuit, would inhibit all cells of other circuits. These cells' PMRs would not show strong transient dynamic threshold dynamics in their PMRs since they belong to networks that integrate information other than the RDMS. This partial transient response may indicate how closely related the different circuits may be to the motion integration circuit. These related neural networks could integrate directional stimuli like light integration or density differentiators but also could generally be circuits that require a binary decision.

Finding this overlap between our identified dynamic threshold neurons and the ones from Bahl and Engert, 2020 shows that the logic selection of cells is a suitable tool to identify rare cell types and can be applied in finding cell types of desired dynamics. This method can be helpful when transitioning from behavioral experiments to whole-brain imaging to identify cells of expected neural functionality, like neurons detecting changes in brightness.

1.4.2 Unbiased metric maps reveal novel motion-responsive Regions and validate established Centers in the Zebrafish Brain

Transitioning to our unbiased metric analysis, we identified several regions of interest where cells respond to presented stimuli (Fig. 3a-e). Our z-score metric map (Fig. 3a) shows that almost all responsive cells to the RDMS-L sit in the left hemisphere. Comparing this to the autocorrelation metric map (Fig. 3b) shows a big overlap of cell distributions but with an added contralateral localization of high metric values. We interpret this as cells reliably not responding through inhibition of the circuit responsible for RDMS-L.

Subtracting these two metric maps may help understand where interactions between neural circuits arise. By taking the intersection of the z-score metric map and autocorrelation map, we can see only cells that reliably do not react. These cells are situated in the right hemisphere anterior hindbrain. Cells that reliably do not react instead of producing noise may be cells that are part of a network that actively inhibits their response. Seen from this angle, these metric maps can be interpreted to distinguish cells in active complex networks from cells in less complex networks with less activity regulation.

Moving to our next metric map, which combines the functionality of the z score (shows responsitivity) and autocorrelation (shows reliability) into the standard deviation metric map. This metric map divides the responsitivity (standard deviation within mean response) and by the reliability (standard deviation across trials), which gives us a responsitivity/reliability index. Four prominent brain regions stand out within these three discussed metric maps. The bulbous structure in the pretectum, the lateral cluster in the eminentia granularis, the anterior hindbrain, and a medial region

in the anterior rhombencephalic turning region (Fig. 3c).

The pretectum is generally seen as a preprocessing center but is not necessarily limited to these bulbous structures. Thus, it is reasonable to assume that these may be specific motion preprocessing centers. To test the hypothesis of this structure being a motion-related preprocessing center, we must present other motion-based stimuli like a moving luminance gradient to rule out the dot processing modality. Alternatively, we could present single moving dots to remove the feature of ambiguous information presented through the RDMS. We expected high metric values in the anterior hindbrain since it was shown that it is the center of motion integration (Bahl & Engert, 2020), which validates this method. We also see metric peaks in the contralateral anterior hindbrain, which generally responds with NPMR to the here-analyzed RDMS-L. These metric peaks may be associated with dynamic threshold cells performing their NPMR.

We analyzed the location of the salient cluster in the eminentia granularis (Fig. 4a) and revealed strong dynamic threshold dynamics (Fig. 4b). Even though these cells are rare and this region has not been associated with motion responses yet the identified cells show a distinct dynamic threshold response. Furthermore, the eminentia granularis is very distant from the anterior hindbrain, making it inefficient as a component of motion integration since it would first require sending signals to the eminentia granularis and then back into the anterior hindbrain making it unlikely to be directly involved in motion processing. There is some weak evidence that the eminentia granularis may be associated with the processing of lateral lines and acoustic signals (Abrahão & Shibatta, 2015; Kaslin & Brand, 2022; Liao & Haehnel, 2012; McCormick, 1989). This would be an interesting new hypothesis looking into this region as an interfacing region between visual and lateral line stimuli. Since the random dot motion triggers the OMR response, which is used to stay at a stable position in streams, it could be useful to measure the currents through the lateral line and then integrate them with visual signals.

The high metrics in the anterior rhombencephalic turning region correlate with previous studies on the optomotor response, which established this region as motion-selective (Naumann et al., 2016). This further validates our metrics as a robust method to find responsive processing centers in the zebrafish brain.

We also identify a cluster with high metric values in the locus coeruleus. This region is prominently featured in all metric maps (1.3a-e), implying a strong functional cluster in this brain area. The locus coeruleus area has not yet been associated with RDMS-L and is considered responsive to forward motion (Naumann et al., 2016). We analyze its dynamics in (Fig. 6a) which shows an integrating slow time constant dynamic. Since the locus coeruleus sits close to the eminentia granularis, it could be another part of the multisensory integration of visual motion and lateral line stimuli.

Our metric map showing mutual information of neural traces with the stimulus shows regions that share the most information with the stimulus. This shows us that the centers of RDMS processing happen as expected in the pretectal bulbs and the anterior hindbrain. Structures like the lateral cluster in locus coeruleus and the localized, responsive group in the anterior rhombencephalic turning region are visible but do not show peak values.

We demonstrate the effectiveness of metric maps for unbiased exploration of neural responses to stimuli by applying them to the single-cell dynamics of zebrafish neurons in response to the RDMS-L. Our analysis unveils several undescribed motion-responsive areas within the locus coeruleus and eminentia granularis characterized by robust reliability and heightened responsiveness to leftward random dot motion. These regions, mainly the eminentia granularis, may be associated with the lateral line organ, potentially representing an interfacing point between lateral line signals and visual signals. Furthermore, we introduce several metrics to gauge reliability, responsiveness, stimulus mutual information, and activity, which we then map onto a reference brain. Our introduced metrics and the method to metric map them onto a reference brain present an easily accessible and visually compelling method to pinpoint neural processing centers within the zebrafish brain. This facilitates investigations into neural processing by aiding the spectator to visually identify regions of interest related to the targeted mechanism.

1.4.3 Neighborhood-Based synchrony metrics highlight functional clusters

Functionality within neuron populations neurons is often proposed to arise with colocalization within the brain (Buzsáki & Mizuseki, 2014; Ohki et al., 2005). We aimed to capture characteristics representing functional clusters by integrating Euclidean distance between cells and synchronous activity. We leveraged the mapped centroids of cells and their extracted single-cell dynamics to create 4 metrics based on Pearson's correlation coefficient and mutual information of cell responses with physically related cells. We combined this approach with our previously established metric maps. This allowed us to visualize and easily extract functional clusters using DBSCAN clustering.

Our analysis highlights asymmetry between hemispheres in the nearest neighbor cross-correlation (nn-CC) in response to RDMS-L (Fig. 5a). This clearly shows how functional clusters govern the PMR in motion integration. These clusters localize in the expected regions of the anterior hindbrain and the pretectum (Fig. 5a). We also reidentify the lateral cluster in the locus coeruleus previously mentioned (Fig. 3). This further validates them as a functionally important cluster. Furthermore, we identify contralateral clusters in the right hemisphere. These resemble cell collections we identified earlier, with our logic-based cell detection (Fig. 2f) and Bahl and Engert, 2020 identified as dynamic threshold cells. This result strengthens our method of neighborhood metrics. Additionally, this result verifies the localization of dynamic threshold neurons in the anterior hindbrain close to the cerebellar neuropil.

Applying DBSCAN on this nearest neighbor correlation metric (Fig. 6a) returns clusters, enabling us to analyze the neural dynamics of these potentially functional neuronal clusters. We find the predicted integrating neural dynamics within the anterior hindbrain (Fig. 6b bluetrace). We also find similar faster dynamics in the pretectal areas, which show a fast time constant as predicted for a preprocessing area. Our newly identified function cluster within the locus coeruleus shows a slow integration neural trace, suggesting that this cluster may be an integration center of the motion integration circuit.

We also calculated a similar metric based on the distance of cells to their most correlating partner, which shows a much wider distribution of cells across both hemispheres. In the visual inspection of this metric map (Fig. 5c), we can identify clusters of close distance to partner cells in the left and right pretectum, the entire left anterior hindbrain (while having a less dense distribution than Fig. 5a), and two clusters in the anterior hindbrain, one localized in the Oculomotor nucleus nIV and another cluster being located more posterior with a bigger lateral spread.

This addition of high metrics in the contralateral hemisphere indicates cells that highly correlate in their neighborhood in their NPMR. Since this metric displays highly correlating cells, we know that cells in this region have a specified response to their non-preferred motion response. Such specific behavior is expected by cells involved in a neural circuit. To summarize, this metric map shows cells involved in neural networks responsible for PMRs in the left hemisphere and cells involved in the neural network response for NPMRs in the right hemisphere. This network in the right hemisphere, which displays NPMR, is the network for integration of the RDMS-R.

1.4.4 Mutual information as a tool for inferred connectivity

We also calculated these neighborhood and partner distance metrics for mutual information, enabling us to track nonlinear relationships between cells (Buzsáki & Draguhn, 2004; Fries, 2009), as well as linear relationships. Looking at the nearest neighbor mutual information map (Fig. 5c), we see a more symmetrical distribution than the nearest neighbor correlation (Fig. 5a). We can identify clusters of high neighbor mutual information in the right and left pretectum (surprisingly more in the right hemisphere) and the entire left and right anterior hindbrain (with a less posterior distribution than Fig. 5a). Through this metric, we highlight clusters that share mutual information about each other, thus highlighting clusters that not only share similar responses but probably influence each other or are influenced by similar sources. This makes mutual information a nice tool for identifying cells involved in coherent neural networks.

Information is the object transmitted through neural networks. Thus, these mutual information clusters may be more critical than correlation clusters. Summarizing this would mean that cells within correlation clusters basically explore the brain by recapitulating the dogma of “what fires together wires together” (Hebb, 1949). On the other side, mutual information shows which cells inform most about their neighbors or are informed by the same cells, basically demonstrating which cells convey the same or similar information.

This would explain the lack of cells in the left pretectum since they all receive independent input from the retina. The cells localized in the contralateral pretectum could then be explained by receiving the same cross-inhibition from cells in the left pretectum, effectively giving them much mutual information about each other by being inhibited by the same cell population. Finding clusters like this and calculating inter-cluster mutual information would be an interesting analysis for exploring the transmission of information through functional clusters across neural networks.

In the DBSCAN analysis of this metric map, we can isolate a population of integrator neurons and dynamic threshold neurons in the anterior hindbrain. We achieved this with the additional help of neural dynamic-based K-means clustering. This shows a definitive overlap of dynamic threshold neurons and the integrator within the left anterior hindbrain in response to RDMS-L, with the integrators being located more lateral and dynamic threshold neurons being located more medial.

Furthermore, we identify a pretectal (orange cluster Fig. 6c) cluster showing NPMRs (negative responses to non-preferred stimuli), which contradicts (Naumann et al., 2016), who classified these neurons as only being responsive to their preferred stimulus. This NPMR response partly refutes the claim of the pretectum being a preprocessing area since it was thought that a combination of left and right-moving stimuli happened further downstream in this neural circuit.

We also identified a cluster through DBSCAN in both the neighborhood correlation map (red cluster Fig. 6a,b) and in the neighborhood mutual information map (yellow cluster Fig. 6c-d), which matches both metrics. This shows that while these metrics can capture different characteristics of neural responses to RDMS-L, they still share similarities given by the organization of the cells within the zebrafish hindbrain, which leads them to find similar clusters.

In the mutual information partner map metric map (Fig. 5d), we visualize the distance between target cells and the cells with the most mutual information about them (Fig. 5d). This metric map shows a far less dense distribution of cells, suggesting that most connections of cells are not within cell clusters but between them, since distances are significantly higher in this metric map (10 μ m to 40 μ m) than in the partner cell distance cross-correlation map (Fig. 5b) (2 μ m to 4 μ m). An interesting idea here would be to compare mutual information between neighboring cells (Fig. 5c) and mutual information between target cells and their partners. This could unveil which clusters receive mutual information from which other cluster or which clusters are governed by local vs. global mechanisms.

Overall, we show that neighborhood-based synchrony metrics can characterize functional clusters in the zebrafish hindbrain and can differentiate cells belonging to stimulus-processing neural networks. They present an intriguing tool to understand connections within the neural processing of motion in the larval zebrafish. They may help to understand how information is passed through the integration network in the zebrafish hindbrain.

1.4.5 K-means clustering of neural response metrics separates subcircuits of motion integration

K-means clustering is an easy approach to distill clusters from data. We applied K-means to our established metrics describing reliability (CC single trial to mean, autocorrelation metric, standard deviation metric), responsivity (z-score, standard deviation metric), neural proximity (msd-CC, msd-MI), and stimulus-informativeness (MI with stimulus). This reduction of cells’ neural responses to metrics equates to a dimensional reduction aimed at improving the clustering quality. We receive clusters varying in their distribution but not in their neural responses. The resulting red (Fig. 7b) and pink (Fig. 7c) clusters present mirror symmetric clusters respectively located in the left hemisphere (red cluster

Fig. 7b) and right hemisphere (Fig. 7c). These clusters (Fig. 7b,c) primarily differ in reliability and responsivity measures (CC single trial to mean, autocorrelation, standard deviation metric, z-score) (Fig. 7i). This is expected since these metrics were only calculated for the metrics responses to RDMS-L, and we assume that the red cluster shows primarily responses to RDMS-R. Both of these clusters (Fig. 7b,c) show the lateral cell loci in the locus coeruleus and eminentia granularis we described earlier. With the blue cluster (Fig. 7a) distributed evenly between hemispheres, we assume that these may represent cells that are shared between the circuits processing RDMS-L and RDMS-R. The hemispherical clusters (red and pink Fig. 7b,c) would then be the cells belonging only to one of these two neural circuits. The last resulting cluster (cyan cluster Fig. 7d) separates itself through its low reliability (Fig. 7i CC single trial to mean, MI to complete trial). The cyan cluster also shows high compactness (Fig. 7f), meaning it is significantly different from the other clusters. This could hint that this cluster may not be related to motion integration or serves an entirely different purpose within motion integration, like being a downstream target. Further analysis could apply clustering on the neural dynamics of the cyan cluster (Fig. 7d) to evaluate its dynamics and function. For the other cluster evaluation metrics, we see that the worst compact clusters (Fig. 7f) are the red and blue clusters. This may be because the red cluster is primed for RDMS-R as the rightward motion processing network, and the blue cluster is a general motion cluster. Thus, the created metrics would not capture their unique characteristics well. Except for these partly not well-clustered cells, the general clustering shows a higher than random separation and silhouette score. These higher-than-random clustering evaluation metrics show that our dimensional reduction using metrics as clustering substrates successfully improved clustering quality.

Having discussed the K-means clustering on our derived metrics, we wanted to perform an analysis resulting in neural dynamic differentiation within the resulting clusters. For this, we used K-means clustering on the PMRs of cells during the presentation of 100% coherence RDMS. With this clustering, we receive three different clusters that resemble the cell dynamics of the major functional cell classes proposed by Bahl and Engert, 2020 (Fig. 8e) in the form of evidence integrators (Fig. 8a), motor command neurons (Fig. 8b), and dynamic threshold neurons (Fig. 8c). While these clusters show a low compactness score (Fig. 8f) and silhouette score compared to shuffled cluster labels, we receive good separation evidenced by clearly defined distinguishable average cluster neural dynamics (Fig. 8e). Furthermore, since we retrieved the functional dynamics of Bahl and Engert, 2020, we decided to recreate their reliability vs. cluster synchrony plot (Fig. 8i). Through this analysis, we see that our dynamic threshold cell (cyan dot in Fig. 8i) compares similarly as the least reliable and least synchronized cluster compared to motor command neurons (purple dot Fig. 8i) and evidence integrators (red dot Fig. 8i). Meanwhile, our evidence integrators and motor command neurons show a different order in their reliability to synchrony relationship with the motor command neurons more reliable and synchronized than the evidence integrators. Our analysis displays a switched hierarchy from the evidence integrator and motor command relationship from Bahl and Engert, 2020. A possible reason for this could be our preselection, which already selects for stronger reliability than was required in Bahl and Engert, 2020.

We show that k-means clustering can retrieve the functional cell types of Bahl and Engert, 2020. This demonstrates how motion integration in the larval zebrafish is based on these functional cell types. This analysis indicates how K-means clustering is an unbiased method of uncovering functional cell types within complex neural circuits from calcium imaging data.

This chapter introduced several biased and unbiased methods to evaluate neural circuits in the framework of an expanded investigation of motion integration in the zebrafish anterior hindbrain by extensive volumetric calcium imaging. We investigate functional dynamics concerning reliability, responsitivity, inter-cell interactions, and localization of functional clusters to highlight how these represent important characteristics of neural circuits. We discover a new integrating locus in the lateral locus coeruleus that shows strong responses to motion stimuli previously thought not responsive to forward motion (Naumann et al., 2016). Close to the new integrating locus, we find even more lateral a region in the eminentia granularis with few cells displaying strong dynamic threshold responses. Weak evidence (Abrahão & Shibatta, 2015; Kaslin & Brand, 2022; Liao & Haehnel, 2012; McCormick, 1989) suggests that the eminentia granularis may be processing signals of the lateral line organ. Together with the close-by locus coeruleus, this

could present an interfacing region between visual and lateral line signals. Furthermore, we establish the motion selectiveness of cells in the pretectum who, contradictory to previous studies (Naumann et al., 2016), not only respond positively to their preferred stimulus but also negatively to non-preferred stimuli, inferring possible inhibition through other circuits. We further connect this to mutual information neighborhood metrics, which discover a high amount of shared information in the right pretectum during stimulation through RDMS-L. This suggests a regulated control of this region, possibly by inhibiting the left pretectum. This creates an exciting possibility of validating this theory by ablating the left pretectum to test if inhibition of the contralateral right pretectum still generates this NPMR after ablation. We also introduce metric maps demonstrating the power of mapping metrics through a reference brain into a shared coordinate system. We leverage this metric map method to compare relationships of neural cell dynamics across the brain, incorporating them with distances between cells and local neighborhoods, thus generating new hypotheses like cross-hemisphere pretectum inhibition during motion processing.

1.4.6 Conclusion

Taken all together, we delved deeper into the functional cell responses constituting the motion integrator in the zebrafish hindbrain. Even though we now have a solid grasp of the circuits' functional cell responses, these only form a part of sensorimotor transformations within neural circuits. Contextualizing these functional responses in terms of connectivity and mode of signal transduction is essential to understanding the flow of information through such complex networks. We suggest that further studies focus on these topics by using electron microscopy, electrophysiology, photoactivations, and cell electroporations to investigate cell connectivity and single-cell transcriptomics, immunohistochemistry, and *in situ* hybridization to investigate neurotransmitter identity. Once all this information is synthesized, we are able to contextualize functional neural dynamics within a framework of connectivity and neurotransmitter identity, thus generating a detailed holistic model of the zebrafish hindbrain integrator. We are confident that such a model, rooted in empirical observations, would prove invaluable and would greatly aid us in understanding the governing principles of sensorimotor transformations in vertebrates.

2 HCR RNA-FISH as a method to identify cellular neurotransmitter identity

2.1 Introduction

Neurotransmitters play a crucial role in neural circuits by characterizing the interactions between cells and how the activity of one cell can influence the activity of other cells. Different neurotransmitters play distinct roles in neural communication and circuit function. Thus, it is important to understand the relationship between a cell's neurotransmitter and its neural response, since this clarifies how a cell interacts with the circuit and the functionality it processes as a part of the neural network. Ultimately, this relationship with neurotransmitters shows how information flows through the neural circuit and how signals are processed within neural networks. Neurotransmitter show a huge variety in functions and expression and range from broadly facilitating neurotransmitters like dopamine to specific excitatory transmitters like glutamate. Accordingly, which neurotransmitter a cell expresses and whether this neurotransmitter acts inhibitory or excitatory, or in other specific ways is known as its neurotransmitter identity.

Traditionally, neurotransmitter identity has been investigated using immunohistochemistry (Chun & Shatz, 1989; Fritschy et al., 1998; Maley, 1996; Priestley et al., 1981) and fluorescent *in-situ* hybridizations (FISH)(Lein et al., 2007; Meissner et al., 2019; Shariatgorji et al., 2021; Tapia et al., 2018). However, these techniques have limitations in spatial resolution and multiplexing capabilities. Furthermore, these techniques often require long incubation times and antibodies may show high cross-reactivity or nonspecific binding. This can lead to high signal-to-noise ratios based on false-positive or false-negative bindings (Pereira et al., 2015).

Recently, single-cell RNA sequencing has proved as an extremely quantitative and reliable approach to retrieving

the neurotransmitter identity with single-cell resolution (Hwang et al., 2018; Kalish et al., 2018). While this approach helps us understand the diversity in neurotransmitter expression heterogeneity, it is impeded by the difficult process of isolating targeted individual cells, making it difficult to relate single-cell expression with other modalities such as functional responses or morphology.

Hybridization Chain Reaction Ribonucleic Acid Fluorescence In Situ Hybridization (HCR RNA-FISH) (Choi et al., 2018) is a method combining FISH with hybridizing chain reaction, a spatial transcriptomic method, presents as the optimal solution for neurotransmitter staining of single cells while retaining cellular identity. This successfully allows for the combination of neural responses with neurotransmitter identity. It enables multiplexed imaging by using multiple probes and amplifiers simultaneously, thus making it easy to stain multiple neurotransmitters simultaneously. In addition, HCR RNA-FISH requires only a short protocol, resulting in a turnover of 3 days from the first sample collection till the imaging of the results.

Several zebrafish labs already use HCR RNA-FISH to survey mRNA expression over zebrafish neural circuits (Lovett-Barron et al., 2017; Lovett-Barron et al., 2020; Schulze et al., 2023). Most notably Shainer et al., 2023 produced expression maps of 291 mRNAs and mapped them to a reference brain (Kunst et al., 2019)). This demonstrates the easy applicability of HCR RNA-FISH to zebrafish to investigate the expression of any mRNAs. including the mRNAs of Vglut2a which is involved with the excitatory neurotransmitter Glutamate (Kani et al., 2010) and Gad1b which is involved with inhibitory GABA signaling (Weston et al., 2011).

Compared to this highly accurate staining of neurotransmitter expression within the experimental animal, Bahl and Engert relied on previously established endogenous expression neurotransmitters within a brain atlas (Randlett et al., 2015). They categorized cells' neurotransmitter identities based on brain regions that showed corresponding endogenous expression of the fluorescently marked Gad1b and Vglut proteins. This approach is inferior to single-cell neurotransmitter identities acquired from HCR RNA-FISH staining performed within the experimental animal.

To automatically achieve this cell-resolution neurotransmitter identity, the staining of an animal must be mapped to a functional stack of the same animal. This is commonly done in the zebrafish field using the ANTs(Avants et al., 2015) or the Insight Segmentation and Registration Toolkit (Lowe kamp et al., 2013). Within the zebrafish field, established registration settings are commonly used for these mapping steps (Lovett-Barron et al., 2017; Shainer et al., 2023). Once cell-to-cell registration is achieved, cell neurotransmitter identity can be automatically assigned.

In this chapter, we will explore HCR RNA FISH as a tool for identifying single-cell neurotransmitter identities within the zebrafish brain, on the example of mRNAs of Gad1b and Vglut2a - two examples of proteins involved in neurotransmitter signaling within the anterior hindbrain of the larval zebrafish. Furthermore, we will investigate the established registration settings for brain mapping in the zebrafish field and propose a metric to objectively judge cell-to-cell registration needed for cell-wise identification of neurotransmitter identity using HCR RNA-FISH.

2.2 Methods

General: In addition to all methods applied in Chapter 1, the following additional methods were carried out for Chapter 2.

HCR RNA-FISH: HCR RNA-FISH, is a molecular technique to visualize the RNA within tissue (Choi et al., 2018). We use HCR RNA-FISH to visualize the neurotransmitter identity of neurons within the zebrafish brain, with Gad1b being a marker for inhibitory gamma-aminobutyric acid (GABA) regions and Vglut2a being a marker for excitatory glutamatergic regions (Filippi et al., 2014; Satou et al., 2013). For this, we use probes supplied by Molecular Instruments targeting the messenger ribonucleic acid (mRNA) of these proteins. We applied the protocol described in Wannemacher, 2023 for both *gad1b* and *vglut2a*. We assigned our *gad1b* probe (Molecular Instruments) the amplifier B1 (Molecular Instruments) with an amplifier paired with Fluorophore 546 and our *vglut2a* probe (Molecular

Instruments) the amplifier B2 (Molecular Instruments) with amplifier paired to Fluorophore 405. For the colocalization experiments recorded with the LSM 880 Zeiss Airyscan, we used an alternative amplifier B2 paired with Fluorophore 647 for the HCR RNA-FISH-staining of *vglut2a*.

Fish lines: We used *Tg(elavl3:H2B-GCaMP8s)* fish with *mitfa* -/ mutant background for our HCR RNA-FISH treatment example (Fig. 9b). We used *Tg(vglut2a:DsRed; elavl3:H2B-GCaMP8s* with a *mitfa* -/ background and *Tg(gad1b:LOXP-DsRed-LOXP-GFP; elavl3:H2B-GCaMP8s)* with a *mitfa* -/ mutant background for our example of endogenous localization (Fig. 9a). For our experiments showcasing the colocalization of HCR RNA-FISH signal with endogenous expression, we used *Tg(BAC(gad1b:GFP)* with a *mitfa* -/ mutant background (Fig. 9c) and *Tg(vglut2a:EGFP* with a *mitfa* -/ mutant background (Fig. 9d).

Imaging two-photon microscope: For two-photon imaging, we use the same custom-built two-photon microscope used in Chapter 1. Using this two-photon microscope, we imaged endogenously expressing fish at a wavelength of 950 nm in two channels using an additional PMT, which recorded red fluorescent light. A dichroic mirror splits the red from the green fluorescent light. We imaged 800x800 pixels with a resolution of 0.5 μm per pixel. Each plane was scanned with a power of 13 mW for 30 s with an acquisition rate of 1 Hz. Overall, we scanned 120 planes with a delta z of 0.5 μm . For imaging HCR RNA-FISH-treated fish, we also used the established two-photon microscope. We scanned these fish in two different imaging configurations. To detect *gad1b*, whose HCR RNA-FISH probe is paired with a red fluorophore (Fluorophore 546), we imaged at a wavelength of 1020 nm in two channels using one PMT to detect green fluorescence from H2B-GCaMP8s and another PMT to detect red fluorescence emitted by the HCR RNA-FISH probe. We imaged with 800x800 pixels with a resolution of 0.48 μm per pixel. Each plane was scanned with a power of 16 mW for 90 s with an acquisition rate of 1 Hz. Imaging power did not matter in these scans and was optimized for optimal Fluorophore 546 signal since the fish were already fixed and dead. Overall, we scanned 40 planes with a delta z of 1 μm . To detect *vglut2a*, whose amplifier is paired to a blue fluorophore (Fluorophore 405), we imaged the fish in a special configuration. Since we ascertained that the H2B-GCaMP showed a not useable fluorescence at 800 nm, the wavelength required to detect the blue fluorophore (Fluorophore 405 nm) paired with the HCR RNA-FISH amplifier of *vglut2a*, we imaged every plane at two wavelengths. First, we imaged each plane at 950 nm, detecting the H2B-GCaMP8s with the first PMT with a power of 13 mW for 120 s with an acquisition rate of 1 Hz. After this, we switched the imaging wavelength to 800 nm, where we imaged the blue fluorophore 405 paired to the *vglut2a*-HCR RNA-FISH amplifier with the second PMT with a power of 20 mW for 120 s with an acquisition rate of 1 Hz. In this imaging process, we used another dichroic mirror, which split the fluorescing green and blue light to separate PMTs. Through this process, we constantly imaged 800x800 pixels with a resolution of 0.48 μm per pixel. Overall, we scanned 40 planes with a delta z of 1 μm .

Imaging LSM 880 Zeiss Airyscan: To image the endogenously expressing fish treated with HCR RNA-FISH, we used an LSM880 Zeiss Airyscan courtesy of the Bioimaging Center Konstanz (BIC). The LSM880 Zeiss Airyscan is a confocal laser scanning microscope. It uses a unique detector system instead of a traditional pinhole, which enables fast simultaneous collection of light from multiple points, which results in increased sensitivity and resolution and faster image acquisition (Huff, 2015). For imaging, a LD LCI Plan Apochromat 25x/0.8 Multi-immersion objective from Zeiss was used.

For the fish expressing endogenous Gad1b and treated with HCR RNA-FISH probes for *gad1b*, we used an excitation wavelength of 488 nm for the endogenous expression and an excitation wavelength of 561 nm for the HCR RNA-FISH amplifier fluorophore (Fluorophore 546). The detection wavelength for the endogenous Gad1b was tuned to 516 nm, and the detection wavelength for the *gad1b* HCR RNA-FISH amplifier fluorophore (Fluorophore 546) was tuned to 579.

For the fish expressing endogenous Vglut2a and treated with HCR RNA-FISH probes for *vglut2a*, we used a detection wavelength of 488 nm for the endogenous expression and an excitation wavelength of 633 nm for the HCR RNA-FISH amplifier fluorophore (Fluorophore 647). The detection wavelength for the endogenous Vglut2a was tuned to 516 nm, and the detection wavelength for the *vglut2a* HCR RNA-FISH amplifier fluorophore (Fluorophore 647) was tuned to 654 nm.

For both fish, we recorded stacks over 200 μm with a delta z of 2 μm .

Imaging registration with ANTs (Avants et al., 2015): We mapped the volume-imaged stack post-HCR RNA-FISH treatment (moving component) two times to an image stack of the same fish pre-HCR RNA-FISH treatment to establish a metric for mapping. For the first registration resulting in Fig. 10a we used standard mapping parameters commonly used in the field for larval zebrafish brain registration (Shainer et al., 2023) we applied the following ANTs command to register the fish.

```
[${ANTs_bin_path}/antsRegistration -v 1 -d 3 --float 1 -o ${  
    ↪ registration_files_prefix_linux}_ --interpolation WelchWindowedSinc --  
    ↪ use-histogram-matching 0 -r [${fixed_path},${moving_path},1] -t Rigid  
    ↪ [0.1] -m MI[${fixed_path},${moving_path},1,32, Regular,0.25] -c [200  
    ↪ x200x200x0,1e-8,10] --shrink-factors 12x8x4x2 --smoothing-sigmas 4  
    ↪ x3x2x1 -t Affine[0.1] -m MI[${fixed_path},${moving_path},1,32,Regular  
    ↪ ,0.25] -c [200x200x200x0,1e-8,10] --shrink-factors 12x8x4x2 --  
    ↪ smoothing-sigmas 4x3x2x1 -t SyN[0.1,6,0.0] -m CC[${fixed_path},${  
    ↪ moving_path},1,2] -c [200x200x200x200x10,1e-7,10] --shrink-factors 12  
    ↪ x8x4x2x1 --smoothing-sigmas 4x3x2x1x0]
```

For the second new improved registration, resulting in Fig. 10b we used the following command.

```
[${ANTs_bin_path}/antsRegistration -v 1 -d 3 --float 1 --winsorize-image-  
    ↪ intensities [0.005, 0.995] --use-histogram-matching 0 -o ${  
    ↪ temp_transformation_path} --initial-moving-transform [${fixed_path},${  
    ↪ moving_path},1] -t Rigid[0.1] -m MI[${fixed_path},${moving_path},1,32,  
    ↪ Regular,0.25] -c [1000x500x250x300,1e-8,10] -s 3x2x1x0 -f 8x4x2x1 -t  
    ↪ Affine[0.1] -m MI[${fixed_path},${moving_path},1,32,Regular,0.25] -c  
    ↪ [1000x500x250x100,1e-8,10] -s 3x2x1x0 -f 8x4x2x1 -t BSplineSyn  
    ↪ [0.1,26,0,3] -m CC[${fixed_path},${moving_path},1,4] -c [100x70x50x20  
    ↪ ,1e-7,10] -s 3x2x1x0 -f 6x4x2x1 -t SyN[0.1,6,0] -m MI[${fixed_path},${  
    ↪ moving_path},1,2] -c [200x200x200x100,1e-7,10] -s 4x3x2x1 -f 12x8x4x2  
    ↪ ].
```

Consecutive transformations were concatenated and applied like in Chapter 1.

Hausdorff distance: The Hausdorff distance is a measure to determine the similarity between two sets of points (R. Tyrrell Rockafellar, 2009). For this, the Hausdorff distance calculates the shortest distance for any point in point cloud A and calculates the shortest distance to any point in point cloud B. The Hausdorff distance is the maximum of these shortest distances calculated. We use the Hausdorff distance to compare the contours of cells in a mapped, HCR RNA-FISH-treated, imaging stack with contours in an imaging stack of the same fish before HCR RNA-FISH treatment. To find the cells to compare the target contour, we select the cells of nearest and 2nd nearest neighbors. We calculated nearest and 2nd nearest neighbor contours based on cell contour centroids using the cKDTree function of scipy (Virtanen et al., 2020) Low Hausdorff distance values show high similarity between contours, and high values show low similarity between contours. We used the directed_hausdorff function of scipy (Virtanen et al., 2020) to calculate the Hausdorff distance between contours. This calculation of the Hausdorff can be formalized in:

$$d_{\text{Hausdorff}} = \sup_{a \in A} \inf_{b \in B} d(a, b)$$

With \sup representing the supremum, \inf representing the infimum, and $d(a, b)$ representing the distance between a point a and a point b .

Wilcoxon signed-rank test: The Wilcoxon signed-rank test (Wilcoxon, 1945) is a non-parametric statistical hypothesis test to compare two related samples by evaluating whether their population mean ranks differ. The Wilcoxon signed-rank test is an alternative to the Student's t-test when the data cannot be assumed to be distributed normally. The h_0 assumption of the Wilcoxon signed-rank test is that the median of the paired differences between the two related groups is zero. This means that the null hypothesis is that there are no systematic differences between the tested distributions, and any difference arises due to chance. We use the Wilcoxon signed-rank test to test if the distribution of Hausdorff distances between target cell contours within a plane and the assigned nearest neighbor and 2nd nearest neighbor contours are different. We assume that cells show a lower Hausdorff distance to their nearest assigned neighbor when correctly registered to their real position. Following this, a good registration should show a significantly lower distribution of Hausdorff distances to nearest neighbors compared to Hausdorff distances to 2nd nearest neighbors. We calculated the Wilcoxon signed-rank test using the `wilcoxon` function of `scipy` (Virtanen et al., 2020).

2.3 Results

2.3.1 Establishing HCR RNA-FISH as a method to identify neuro-transmitter identity of functionally identified cells

Neurotransmitter identity plays an important role in defining the functions of cells within neural circuits. They determine how the activity of neurons modulates other cells of the neural circuit through inhibition and excitation and thus modulate the overall behavior of the network. Because of this, it is of crucial importance to understand the distribution of neurotransmitter identity and neurotransmitter expression when investigating neural networks such as the hindbrain integrator.

To explore the neurotransmitter identities within the motion integration circuit of the larval zebrafish hindbrain, we decided to use the promising HCR RNA-FISH method to localize the expression of *Gad1b*-mRNA, the mRNA of a protein involved in inhibitory GABA signaling (Kani et al., 2010). We also localized the mRNA of *Vglut2a*-mRNA, a protein involved in Glutamate signaling (Weston et al., 2011). We applied this method to 5 dpf old zebrafish larvae expressing H2B-GCaMP8s using the protocol established by (Wannemacher, 2023). This staining of the mRNA of *Gad1b*/*Vglut* caused fluorescence of Fluorophore 546/Fluorophore 405, enabling us to identify regions of expression and, thus, inhibition/excitation. We imaged this staining with a custom-built two-photon microscope (Fig. 9b). The staining (Fig. 9b) reveals a distribution of *Gad1b*-HCR RNA-FISH signal localized in the medial and lateral parts of the hindbrain, in the midbrain at the border to midbrain as well as close to the midline in the midbrain. *Vglut2a*-HCR RNA-FISH shows a distribution surrounding the tectal neuropil in the midbrain and the cerebellar neuropil in the hindbrain. Furthermore, localizations of the *Vglut2a*-HCR RNA-FISH signal can be spotted in the lateral and medial parts of the posterior hindbrain and in a small hole in the *Gad1b*-HCR RNA-FISH signal within the anterior hindbrain.

To get a ground truth of the spatial expression of the *Vglut* and *Gad1b* protein, we generated two zebrafish lines expressing fluorescently marked *Vglut2a* and *Gad1b*. We imaged this staining with a custom-built two-photon microscope (Fig. 9b). The endogenous expression of fluorescently marked *Vglut2a* and *Gad1b* (Fig. 9a) shows *Gad1b* primarily localized in the medial and lateral anterior hindbrain as well as in the midbrain close to the midline and the border to the hindbrain. The expression of the endogenously marked *Vglut2a* shows a distribution focused around the tectal neuropil in the pretectum and around the cerebellar neuropil. It also shows weaker expression in the posterior hindbrain and within a hole in the *Gad1b* expression within the anterior hindbrain.

To verify the colocalization of the HCR RNA-FISH staining with the endogenous expression of *Gad1b* and *Vglut2a* within the same fish, we generated two zebrafish lines with DsRed fused expression of *Gad1b* and *Vglut2a*. We imaged the endogenous expressions within a custom-built two-photon microscope (Fig. 9a). Furthermore, we applied the HCR RNA-FISH staining to fish with marker protein-fused expressions of *Gad1b* and *Vglut2a*. We recorded

this HCR RNA-FISH staining of a fish expressing [fused protein] with gad1b probes and the staining of a fish expressing Ds-red:Vglut2a with vglut2a probes with an LSM 880 Zeiss Airyscan at the Bioimaging Center Konstanz (BIC). This shows a good overlap of the HCR RNA-FISH signal and the endogenously marked expression. Looking at the Gad1b expression and staining (Fig. 9c) we see colocalization all around the brain mainly in the anterior hindbrain with a spike in very lateral parts of the hindbrain in the eminentia granularis. Further colocalizations can be spotted in the midbrain close to the midline and at the border to the hindbrain. The Vglut2a expression and staining (Fig. 9d) show colocalizations most saliently in the olfactory bulb and around the tectal and cerebellar neuropil. Colocalization also can be found very medial in the anterior hindbrain and scattered around the posterior hindbrain. Potential mismatches of the distributions do not arise and are rather artifacts of expression strength and the ability of HCR RNA-FISH to stain certain brain regions. Summarizing this we approve HCR RNA-FISH as a suited method to visualize the expression of Gad1b and Vglut2a within the larval zebrafish brain.

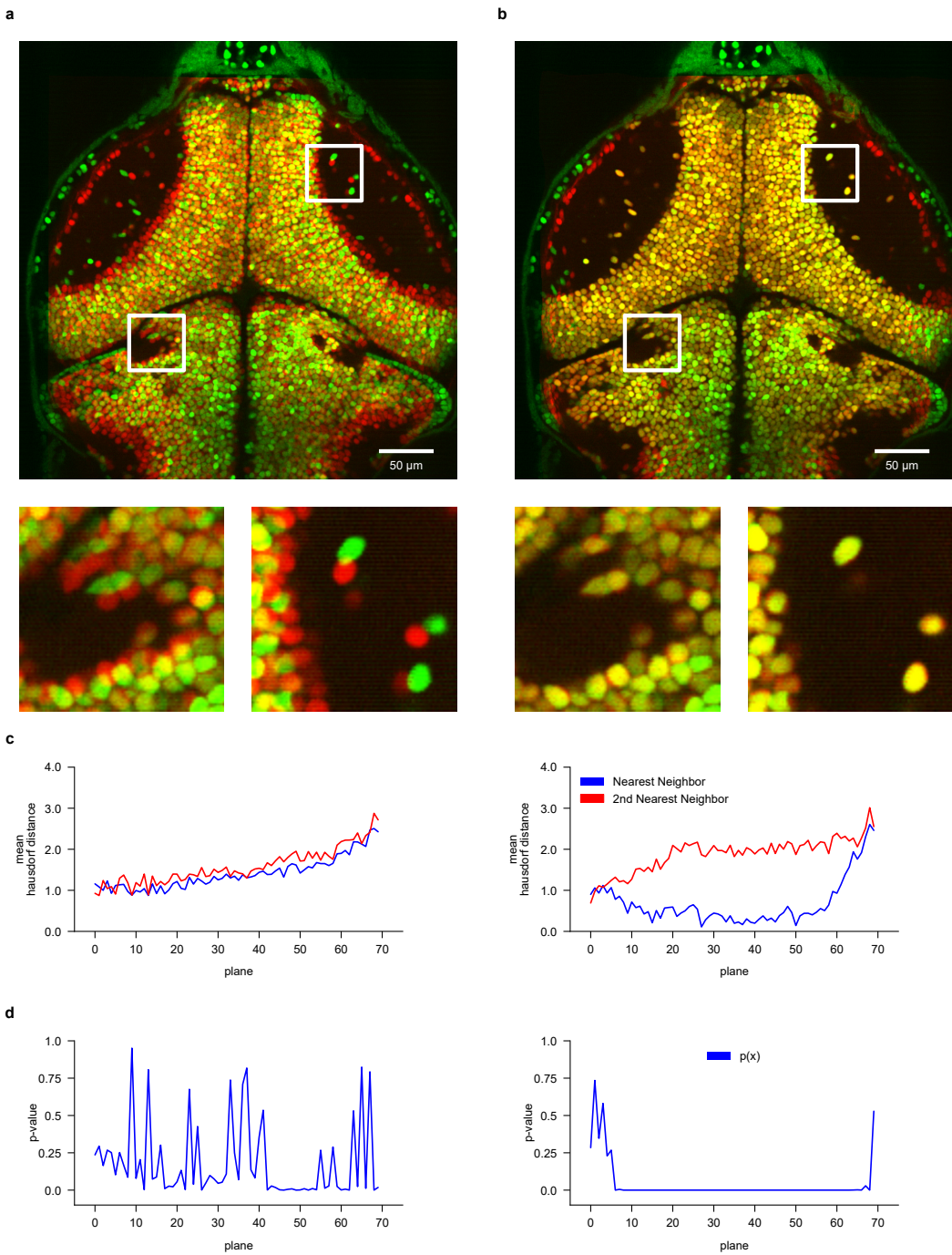


Fig. 9: Verification of registration quality using the Hausdorff-distance. **a**, Plane of a brain treated with HCR RNA-FISH (red) registered to the same brain pre-HCR RNA-FISH (green) using established registration parameters. White squares correspond to insets (bottom). **b**, Plane of a brain treated with HCR RNA-FISH (red) registered to the same brain pre-HCR RNA-FISH (green) using our new registration parameters, including b-spline-syn. White squares correspond to insets (bottom). Same imaging stack as in **(a)**. **c**, Mean Hausdorff-distance per plane between target cell in HCR RNA-FISH treated stack and nearest neighbor/2nd nearest neighbor in pre HCR RNA-FISH treated stack. Visualized for established registration parameters (left) and new b-spline-syn registration parameters (right). **d**, P-values of Wilcoxon signed-rank test per plane between distribution of Hausdorff-distance values in HCR RNA-FISH treated stack and nearest neighbor/2nd nearest neighbor in pre HCR RNA-FISH treated stack. Visualized for established registration parameters (left) and new b-spline-syn registration parameters (right).

2.3.2 Establishing a metric for brain mapping using ANTs (Avants et al., 2015)

To relate the previously established identification of neurotransmitter identity to single cells we need to map the different imaging stack to a common reference brain. Using ANTs (Avants et al., 2015) to do this kind of mapping is a quick and useful way to align imaging data from experiments in different animals to a common coordinate system. This allows us to easily compare physical distances between cells, analyze brain regions, and display cells within a common brain for visualization. Furthermore, an important application of ANTs is the mapping of imaging stacks to other imaging stacks of the same individual animal. This can be useful when trying to align imaging stacks recorded at different times, containing different information while being recorded from the same sample. The challenging aspect is the exact mapping of cell X in the reference stack to cell X*, which is the same cell in the same fish at another time point.

We aimed to explore the relationship between functional response classes present in the motion integration network of the anterior hindbrain of the larval zebrafish (Bahl & Engert, 2020) and their neurotransmitter identity. We tried mapping imaging stacks containing volumetric functional responses based on average H2B-GCaMP8s signal to imaging stacks containing HCR RNA-FISH signal and H2B-GCaMP8s as reference using standard ANTs parameters used in the field (Shainer et al., 2023). This gave insufficient results in which cells were not mapped to their corresponding position in the reference imaging stack (Fig. 10a). We explored the available options within the ANTs (Avants et al., 2015) registration commands to find parameters delivering better registration and finally settled on added B-spline-syn registration (Tustison & Avants, 2013). These added registration steps deliver a clearly discernable improvement in cell-to-cell matching in the registration (Fig. 10b).

To quantify this, we developed a cell contour-based metric quantifying the registration quality. To create this metric, we assumed that cell contours were unique to cells and, furthermore, would always be more similar to their own contour than to the contours of their neighbors. For this, we first segmented every cell in both the mapped moving stack (imaging stack that the registration is applied to) and fixed stack (imaging stack the moving stack is registered to) using Cellpose (Stringer et al., 2021). Next, we calculated for every segmented cell in the moving stack its nearest and second nearest neighbor cell in the fixed stack based on cell centroids. According to our assumption that cell contours of cells look more similar to themselves than their neighbors even after HCR RNA-FISH (Choi et al., 2018) treatment, we calculated the Hausdorff distance for every pair of nearest neighbor and 2nd nearest neighbor contours. The Hausdorff distance measure is used for comparing point clouds. For every point in set A, it searches the shortest distance to every point in set B. The Hausdorff distance is defined as the maximum of these shortest distances between those point clouds (R. Tyrrell Rockafellar, 2009). We averaged the Hausdorff distance between the nearest and second nearest neighbors per plane and thus received a value for each plane characterizing the registration quality (Fig. 10c). According to our assumption that cells show a lower Hausdorff distance when they are correctly mapped (since they are more similar to their own contour than to their neighbors' contours), we performed Wilcoxon signed-rank tests between the distribution for Hausdorff distances of cells to their nearest neighbor and their second nearest neighbor (Fig. 10d). We use a Wilcoxon signed-rank test since the data is paired (the contour of the cell in the moving stack is compared to the nearest neighbor and 2nd nearest neighbor in the fixed stack) and receive significant results for our proposed novel registration settings. This verifies our registration using B-Spline-Syn and enables us to map a cell to the same cell in different imaging stacks of the same animal.

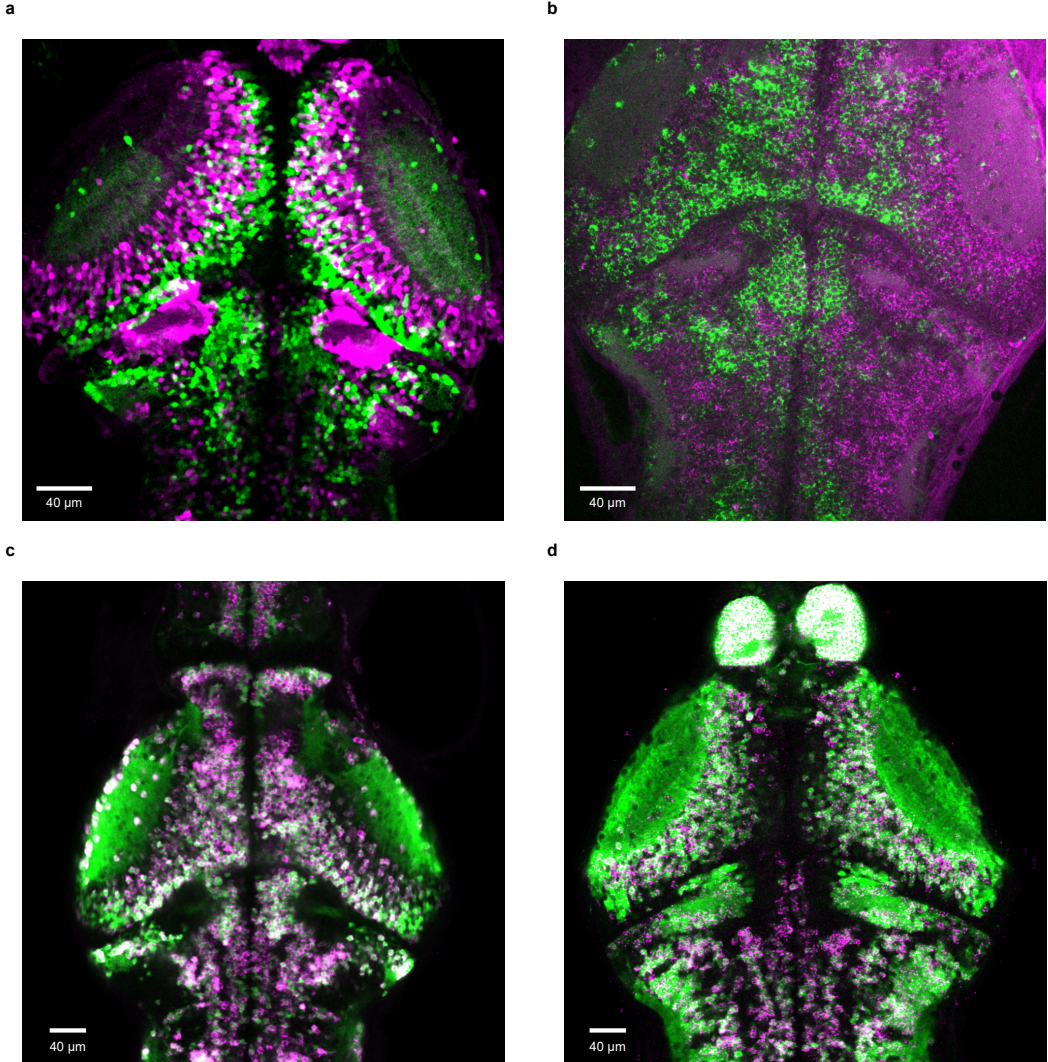


Fig. 10: Colocalization of endogenous Gad1b/Vgluta2 expression and gad1b/vglut2a staining. **a**, Composite image of a fish expressing endogenously labeled Gad1b (green) and a fish expressing endogenously labeled Vgluta2a (magenta). Imaged with a custom-built two-photon microscope. **b**, Composite image of a fish with HCR RNA-FISH labeled Gad1b mRNA (green) and the same fish labeled with HCR RNA-FISH labeled Vgluta2a mRNA (magenta). Imaged with a custom-built two-photon microscope. **c**, Composite image of fish expressing endogenously labeled Gad1b (green) and the same fish with HCR RNA-FISH labeled Gad1b mRNA (magenta). Imaged with an LSM 880 Zeiss Airyscan. **d**, Composite image of fish expressing endogenously labeled Gad1b (green) and the same fish with HCR RNA-FISH labeled Gad1b mRNA (magenta). Imaged with an LSM 880 Zeiss Airyscan.

2.4 Discussion

Here, we established HCR RNA-FISH as a method suited for the localized detection of mRNA within the zebrafish hindbrain. We show how distributions of endogenously fluorescent labeled Gad1b/Vglut2a show a similar distribution to the staining of gad1b-mRNA and vglut2a-mRNA. Furthermore, we apply gad1b/bglut2a configured HCR RNA-FISH staining to endogenously labeled Gad1b/Vglut2a fish and detect a match in their distributions. We also highlight a new superior set of registration commands for cell-to-cell mapping within the same sample by leveraging B-Spline-Syn. We validate this superior cell-to-cell registration quality by creating a segmentation and Hausdorff-distance-based metric.

2.4.1 HCR RNA-FISH staining of Gad1b/Vglut2a mRNA shows colocalization with endogenously marked Gad1b/Vglut2a

Comparing our HCR RNA-FISH staining of Gad1b and Vglut2a (Fig. 9b) to our endogenous expression of fluorescently marked Gad1b/Vglut2a (Fig. 9a) we see that similarities are instantly recognizable. We observe a prominent group of Gad1b-expressing cells (Fig. 9a) and a group of HCR RNA-FISH-Gad1b stained cells (Fig. 10a) within the anterior hindbrain. In both stain and endogenous expression we can spot the localization of Vglut2a around the cerebellar neuropil which is also in stain and expression a Gad1b free area. Furthermore, at the left-hand side of the stain and expression, a short stripe of Gad1b signal surrounded by Vglut2a signal can be spotted. Examining the distribution in the midbrain is unfortunately difficult since the imaging of the endogenously labeled animals was performed pitched compared to the HCR image stack. Still, we find a general pattern both in stain and expression of Gad1b being localized at the border to the hindbrain and close to the midline in the midbrain. The Vglut2a on the other hand rather shows a distribution surrounding the tectal neuropil. Another interesting matching distribution is a hole in the posterior-anterior hindbrain of the Gad1b distribution. This hole is both in stain and expression similarly filled by cells expressing Vglut2a. Examining these HCR RNA-FISH Gad1b/Vglut2a stainings and the signal of endogenous expression of Gad1b/Vglut2a we identify a matching distribution confirming the ability of HCR RNA-FISH to stain regions of Gad1b/Vglut2a expression

These colocalizations show how HCR RNA-FISH staining is a reliable way of identifying regions of Vglut2a and Gad1b expression and following from this a reliable way of identification of GABAergic and Glutameric regions. This method represents an easy, fast, and reliable way to access the neurotransmitter identity of cells within the larval zebrafish brain

2.4.2 B-Spline-Syn registration enables cell-to-cell mapping between pre-HCR and post-HCR imaging stacks of zebrafish brains

We established added options to imaging stack registration in the form of B-Spline-Syn registration. These added options evidently provide a better cell-to-cell matching registration of an imaging stack post-HCR RNA-FISH to an imaging stack pre-HCR RNA-FISH of the same animal (Fig. 10b) than previously in the field-established registration settings (Fig. 10a). Furthermore, we quantify this difference in registration quality by introducing a cell contour and Hausdorff distance-based metric. We evaluate this metric per plane for the established registration settings (Fig. 10c left) and our newly suggested B-SplineSyn registration. While the established registration settings show similar mean Hausdorff distance metrics for nearest neighbors and 2nd nearest neighbors, our new registration settings show easily distinguishable mean Hausdorff distance mean values per plane. We calculated significances using the Wilcoxon signed-rank test between nearest neighbors and 2nd nearest neighbors Hausdorff-distance distributions of every per plane (Fig. 10d). Evaluating the resulting p-values for the established registration settings, we see fluctuating p-values over planes for the established settings, signifying a bad registration (Fig. 10d left). In contrast, our proposed registration settings have low values for almost every mapped plane in the fish (Fig. 10d right). The initial high p-values meanwhile can be explained by this representing the very top of the fish, which is most influenced by the fish shrinking during HCR RNA-FISH treatment (visible in Fig. 10a,b, green outer fish) thus making good registration difficult. Alternatively, this could also be explained by general boundary effects which decrease image registration accuracy in boundary regions (Zitová & Flusser, 2003),

Overall, this quantification shows that B-Spline-Syn registration allows for registration in cell-to-cell matching quality between imaging stacks post-HCR RNA-FISH treatment and imaging stacks pre-HCR RNA-FISH treatment. Furthermore, we introduce our nearest cell contour Hausdorff distance-based metric as a quantification tool for registering imaging stacks within the same animal. These tools enable us in the larger picture to understand and map neurotransmitter identity distribution of the hindbrain integrator network.

2.4.3 Outlook

In this chapter we introduced HCR RNA-FISH to determine neurotransmitter identity of cells in the larval zebrafish brain. We confirm this by comparing endogenous expression of Vglut2a and Gad1b to stainings of Vglut2a and Gad1b created through HCR RNA-FISH.

Furthermore, we propose new registration settings leveraging B-Spline-Syn which enables the mapping of cells in an HCR-stained stack to their real position in pre-HCR acquired imaging stacks of the same animal. Combining these two methods would enable us to automatically characterize the neurotransmitter identity of every cell recorded post-experiment. Through this, we could map the functional cell types in the motion integrator discussed in Chapter 1 and Bahl and Engert, 2020 to their neurotransmitter identity. We would do this by recording an imaging stack of a larval zebrafish while presenting it with RDMS, next recording a volume stack of the fish then applying HCR RNA-FISH staining, and finally recording the HCR RNA-FISH staining. After every image stack was recorded, we could map the HCR RNA-FISH staining and the functional stack to the volume imaging stack of the living animal. Based on these mapped cells we then would be able to automatically assign cell neurotransmitter identity to functional cell type identity. This would help us to contextualize the functional dynamics of cell dynamics processing motion integration and beyond that help us to understand how inhibition and excitation are distributed across functional components within this complex neural circuit.

Even though our proposed registration settings work very well for our application and setup, this does not guarantee cell-to-cell registration quality for other applications and setups. Thus, we suggest a grid search of registration settings using our nearest cell contour Hausdorff distance-based metric as the fitness parameter. Hereby, we have to keep in mind that for this metric to work, cells must be easily segmentable, which would reduce the applicability of such a characterization of metaparameters, to only being useful to imaging experiments using nuclear localized GCaMP or other stainings that result in clear differentiation of cells.

Overall, we confirm that HCR RNA-FISH is a suitable and fast method to mark glutamatergic and GABAergic regions within zebrafish brains with the potential to retrieve single-cell neurotransmitter identity post-experiment. This enables us to contextualize functional neural responses of cells with their neurotransmitter identity which enables us to investigate further the balance of inhibition and excitation within neural networks. We are confident that integrating neurotransmitter identity with neural dynamics is an important step in understanding how the dynamics present in complex neural circuits are generated and work together to solve complex tasks. This integrated view is an important step to understanding how motion integration in the zebrafish and beyond that any complex sensorimotor transformation network in vertebrates processes sensory information.

3 Functionally guided photoactivation to map neurite morphologies

3.1 Introduction

Networks are defined through their connections. The function of a neuron can thus only be understood in the light of its connection to other parts of the network. A neural network's edges define how information flows and signals are processed through the network. Complex functionality like integration can arise from circuit motifs (R. Yang et al., 2023). By understanding how morphology and the connections of a neural circuit relate to its function, we are able to uncover basic principles of neuronal computation.

The standard approach to exploring connectivity lies within electron microscopy (EM), as it offers the highest resolution. Much interesting research has been done within the field of EM in recent years, including reconstructing

the complete connectome of the fly (Scheffer et al., 2020; Zheng et al., 2018) and the octopus (Bidel et al., 2023). Furthermore current efforts are working on creating a connectome of the zebrafish brain. While these studies provide highly detailed maps imaged at stunningly high resolution, they are missing the activity of cells which further characterize the functionality of neural networks.

This is proposed to be solved by correlated light and electron microscopy (CLEM), which consists of EM imaging that has been previously imaged in a functional context like the RDMS (R. Yang et al., 2023). However, CLEM is still plagued by the same problems as EM. First, it is time-intensive to create a whole-brain volume stack of even a tiny brain like the one of Drosophila (Zheng et al., 2018), and secondly the preprocessing of alignment, segmentation and other preparations takes even longer than the imaging process on its own. Furthermore, the size of the teams that must be appointed for years for such a project and the huge amounts of money that the process of producing such a dataset requires is not replicable. In the end, it leaves us with a repeat number of one, which is the opposite of the scientific process which lives from the constant generation and falsification of new hypotheses. That is, to create a CLEM that truly solves a functional question to the brain, we would have to put every stimulus imaginable in front of it in the light microscopy part and we would probably still forget one.

However there are other methods to relate the functionality of cells to neurite morphology. For example, relating light microscopy with sparse electroporations (Boulanger-Weill et al., 2017). While this method definitely has a faster turnover than recording full EM stacks, it is limited by the electroporation skills of the experimenter and furthermore is only applicable in easily reachable areas of the zebrafish brain. This would cause issues within our experimental set up, as the anterior hindbrain is located relatively deeply in the zebrafish brain.

Other attempts of mapping the brain rely on the stochastic expression of markers in cells (Kunst et al., 2019; Pan et al., 2011) which deliver also one neurite at a time but without associated function.

Förster et al., 2017; Förster et al., 2018 recently established an all-optical toolkit that connects functional neural dynamics with morphology within the zebrafish. For this, they created a fishline expressing a GECI and photoactivatable GFP. Through this, they were able to reconstruct a center that processes optic flow in the zebrafish (Kramer et al., 2019) by first identifying functional cells of interest and then photoactivating them to reconstruct their morphology later. This represents an adaptable, non-invasive method to investigate the morphology of neurites.

These photoactivatable versions of GFP were established by Patterson and Lippincott-Schwartz, 2002 and first applied by Ruta et al., 2010 to investigate a neural circuit within the fly. Beyond these green photoactivatable fluorophores, other photoconvertible/photoactivateable fluorophores exist (Lippincott-Schwartz & Patterson, 2009; Lukyanov et al., 2005) like Kaede (which changes after photoactivation from green to red) (Sato et al., 2006) or KFP1 (green to red) (Chudakov, Belousov, et al., 2003; Chudakov, Feofanov, et al., 2003).

In this chapter, we will investigate the neuronal morphology of functional neuron classes of the motion integrator within the zebrafish hindbrain (Bahl & Engert, 2020). For this, we leverage C3PA-GFP, a photoactivateable version of GFP (Patterson & Lippincott-Schwartz, 2002), to perform functionally guided photoactivations as established in Förster et al., 2017; Förster et al., 2018. Furthermore, we will connect this to HCR RNA-FISH stainings, providing us with the neurotransmitter identities of the investigated cells and combining functional and morphological data within the same individual.

3.2 Methods

General: In addition to all methods applied in Chapters 1 and 2, the following additional methods were added for Chapter 3.

Fishlines: We used Tg(Cau.Tuba1:c3paGFP:elavl3:H2B-GCaMP6s) fish with a **mitfa** *-/-* mutant background, which express a photoactivatable version of GFP fused to alpha-tubulin as well as the nuclear-localized GECI H2B-GCaMP6s.

We chose H2B-GCaMP6s instead of H2B-GCaMP8s since the experiment required low fluorescence of the GECI to improve the visibility of photoactivated cells. We prescreened fish for homozygotic expression of C3PA-GFP by running test photoactivations in the tectum of the larva, a region easily accessible and far enough removed from the anterior hindbrain not to receive artifacts from test photoactivations. We also prescreened for heterozygotic expression H2B-GCaMP6s by evaluating fish pre-experiment for low fluorescence to further ensure maximum visibility of photoactivated neurites.

C3PA-GFP: C3PA-GFP is a photoactivatable version of GFP (Patterson & Lippincott-Schwartz, 2002; Ruta et al., 2010). It can be activated from a non-fluorescent state to its fluorescent state upon intense irradiation to a wavelength of 413 nm. After this activation, C3PA-GFP increases its fluorescence 100 times when excited by 488 nm light and remains stable for multiple days (Patterson & Lippincott-Schwartz, 2002).

Functional cell identification: We again used a custom-built two-photon described in Chapters 1 and 2, further outlined in Fuchsloch, 2023. For the functional imaging, we presented RDMS while recording a window of the left anterior hindbrain of a larval zebrafish expressing C3PA-GFP: H2B-GCaMP6s; mitfa -/ - for 15 min to 30 min with a framerate of 1 Hz over an area of 200x300 pixels at a resolution of 0.4 μm per pixel. We chose this lower resolution to decrease processing time to minimize the time between functional imaging and photoactivation. We imaged at 950 nm with a power of 7.5 mW to 9.0 mW due to increased pixel dwell time compared to previous functional recordings. Recording with the same power may lead to premature photoactivation. After imaging a stimulus-aligned stack for responses to RDMS-L and RDMS-R as well as an average stack was created. Based on these stimulus stacks, the produced average stack, and the live image we identified a target cell that matched the dynamics of the described cell classes in Bahl and Engert, 2020 and was relocatable based on surrounding landmarks like dark neuropil regions or salient cell arrangement. We analyzed cell responses by syncing the 3 created stacks, drawing a contour around the investigated cell (freehand tool), and plotting the Z-axis profile of the stimulus-aligned stacks in live mode in Fiji (Schindelin et al., 2012). Through this, we could reliably identify cells belonging to one of the functional classes suited for photoactivations within 5 min to 15 min.

Photoactivation: After identifying a target cell we increased the scan area to a 300x300 pixel area with a resolution of approximately 0.05 μm per pixel. This allowed us to target the exact center of the target cell and focus the laser on a minimal area to avoid the photoactivation of multiple cells. We photoactivated the target cell with 100 to 1000 short laser pulses at 760 nm with a laser power of 5 mW to 8 mW. These 200 ms pulses interspaced by 100 ms downtime were interrupted after 20 repeats for an evaluation scan at 950 nm. If the cell was deemed photoactivated during the evaluation scan the protocol was interrupted prematurely. Through this approach, we were able to achieve reliable single-cell photoactivations. Single-cell photoactivations were generally easier to achieve with the custom-built two-photon microscope equipped with the 25x Nikon objective, which was measured to have a comparatively better point spread function (Fuchsloch, 2023).

Volume imaging: Before volume imaging, we anesthetized the fish with 300 μL of 0.015% MS-222 (Sigma-Aldrich) solution (Wilson et al., 2009) to prevent motion artifacts while recording the photoactivated neurite morphology. We applied the MS-222 directly into the Petri dish the fish was embedded in without removing it from under the microscope. After 15 min when the fish was properly anesthetized, we started imaging a volume scan over 200 μm with a delta z of 2 μm recording the entire hind- and midbrain of the larval zebrafish. We recorded each plane for 90 s, with a framerate of 1 Hz over an area of 800x800 pixels at a resolution of 0.4 μm per pixel. We used a linear increasing imaging power to compensate for deeper areas, which resulted in scans having an imaging power of 13 mW at the uppermost plane and a power of 18 mW at the bottom plane. We traced photoactivated morphologies from the volume stack the Fiji (Schindelin et al., 2012) implementation of simple neurite tracer (Arshadi et al., 2021) yielding SWC files for every traced neurite.

HCR RNA-FISH After volume scanning, we removed the larvae from their embedded Petri dish by cutting out a block from the agarose containing the zebrafish. We then applied HCR RNA-FISH staining, using the protocol of

Wannemacher, 2023, for *gad1b* and *vglut2a*. We used, as established in Chapter 2, Fluorophore 546 for *gad1b* and Fluorophore 405 for *vglut2a*. We scanned the HCR RNA-FISH-*Gad1b* signal and the HCR RNA-FISH-*Vglut2a* signal like in Chapter 2 resulting in an imaging stack containing HCR RNA-FISH and H2B-GCaMP6s signal. We imaged around 40 planes with a delta z of 1 μm in an area of 800x800 pixel area, recorded at a resolution of 0.3 μm around the estimated position of the photoactivated cell. The area of the photoactivated cell was estimated by landmarks present in the zebrafish mid- and hindbrain. Neurotransmitter identity was determined by locating the photoactivated cell within the H2b-GCaMP6s signal of the HCR RNA-FISH volume stacks and interpreting halos around this identified cell. Identification was aided by the higher fluorescence of photoactivated cells and landmarks present in the zebrafish anterior hindbrain.

Registration of neurites: We mapped the neurite morphologies to the z-brain by applying the inverse transformations, created through registration of the volume stack to the Z-brain, to the SWC files. For the registration of the volume stack, we used the same settings as in Chapter 1. We transformed the SWC file to a CSV to apply the inverse transformation with the following command.

```
[${ANTs_bin_path}/antsApplyTransformsToPoints --precision 0 --dimensionality
 ↪ ${ANTs_dim} --input ${all_data_points_path_linux} --output ${
↪ all_data_points_registered_linux} --transform ${
↪ transformation_prefix_path_linux}_inverse.nii.gz]
```

After successful transformation, we reverted the output CSV file into a SWC file.

Visualization of neurites: To visualize the traced neurites we first created meshes for each brain region categorized in the z-brain atlas. To generate these meshes, we transformed the available region masks with the sitk function of SimpleITK (Lowekamp et al., 2013) into NII.GZ files, which we then transformed into an OBJ file with the nii2mesh tool (Rorden, 2023) which applies a marching cube algorithm to create a mesh from the supplied NII.GZ file. To visualize traced neurites together with the created meshes, we used various functions of the navis package (Schlegel et al., 2023) which enabled us to create figures and 3D animations of our mapped neurites within the Z-brain atlas.

3.3 Results

To understand the processing of sensory information within neuronal networks, we have to understand the activity of cells that comprise the system and how these cells transmit their activity through the network. While Chapter 1 delved into the analysis of neuronal activity, Chapter 2 introduced a method to determine the neurotransmitter identity of a cell. However, understanding how a cell distributes its signal through its connectivity across the network, specifically which cells receive its input, remains an important unanswered question. To explore the connectivity and projections of functional neuron types within the motion integration network of the larval zebrafish, we conducted functionally guided photoactivations using a custom-built two-photon microscope.

3.3.1 Functionally guided photoactivations

To identify the previously discussed functional neuron types of evidence integrator neurons, dynamics threshold neurons, and motor command neurons Bahl and Engert, 2020, we sought to establish a protocol for functionally guided photoactivations. We started our experiments with 15 - 30 minutes of RDMS presentation while imaging a single plane within the anterior hindbrain of a larval zebrafish expressing C3PA-paGFP; H2B-GCaMP6s (Fig. 11a). We found that this timeframe was long enough to get enough responses of cells to RDMS-L and RDMS-R to evaluate their functional dynamics while also preventing too many movements of the fish, resulting in a shift of plane during

imaging. We also determined that it was beneficial to present fish with 15 minutes of RDMS before the start of functional imaging to induce futility, which stops fish from eliciting behaviors in response to the RDMS (Mu et al., 2019). This reduced the motion artifacts and shifting of planes during imaging significantly. We stimulus-aligned the functional recordings and manually identified cell types based on their average neural responses to RDMS-L and RDMS-R, referencing the neural dynamics established by Bahl and Engert, 2020 using Fiji (Schindelin et al., 2012) (Fig. 11a). After identifying a target cell that resembled the functional dynamic of either a dynamic threshold neuron/rebound neuron, evidence integrator neuron, or motor command neuron (Fig. 11c,d) and was structurally identifiable by surrounding landmarks (Fig. 11c), we photoactivated the selected cell at 760 nm (Fig. 11a). The number of pulses and power required to photoactivate cells differed greatly between animals. While cells in presumably homozygotic fish were photoactivatable with repeats as low as 20 and laser power as low as 5 mW, other cells in presumably heterozygotic fish were not photoactivatable by 1000 repeats with 8 mW. Therefore we introduced test photoactivations in the tectum to gauge the photoactivateability of the fish. After successful photoactivation, we anesthetized the fish with MS-222 to ensure no movement during the following volume scan. After 15 minutes, when the fish was successfully anesthetized, we imaged a volume stack of the zebrafish's complete hind- and midbrain to capture the morphology of the neurites of the photoactivated cell (Fig. 11b). Having completed the volume scan, we next prepared the fish for HCR RNA-FISH treatment to determine the neurotransmitter identity of the photoactivated cell (Fig. 11a,f). We cut out a block of the agarose the fish was embedded in and transferred the sample into 4% PFA (Fig. 11a). For the HCR RNA-FISH treatment, we followed the protocol established by (Wannemacher, 2023) using probes for Gad1b and Vglut2a. After finalization of the HCR RNA-FISH treatment, we recorded a fine resolution volume scan of H2B-GCaMP6s and HCR RNA-FISH staining around the plane the photoactivated cell was localized in (Fig. 11a,f). We located the position of the photoactivated cell within these volume stacks manually using the H2B-GCaMP6s signal. We concluded neurotransmitter identity from the halos surrounding the photoactivated cell in the correlating HCR RNA-FISH staining (Fig. 11f). Now that we acquired functional dynamics as well as neurotransmitter identity of neurons, we only need to obtain the neurons' morphology by analyzing the photoactivated neurons.

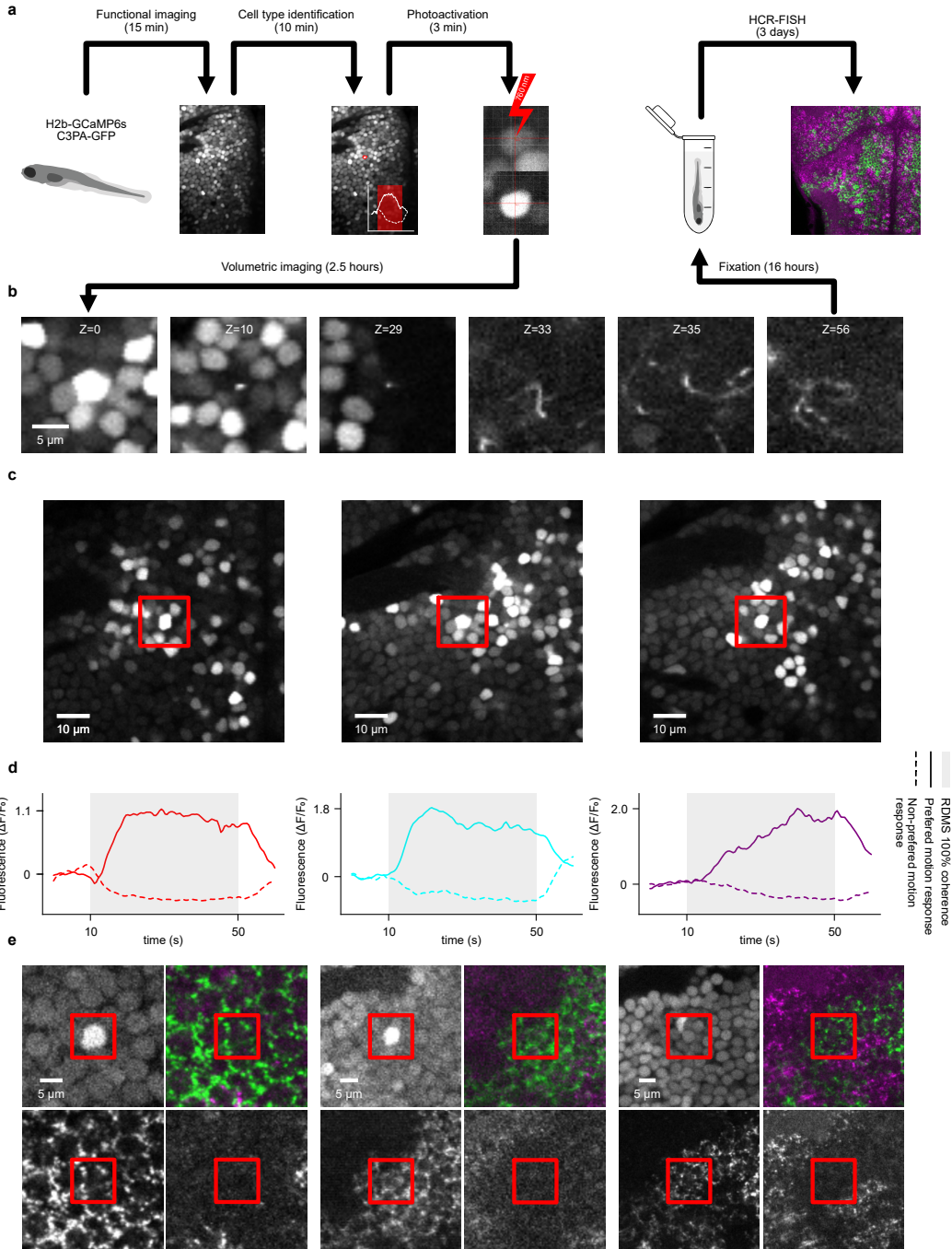


Fig. 11: Functionally guided photoactivations to connect functional responses, neurotransmitter identity, and morphology. **a**, Procedure of functionally guided photoactivations combined with HCR RNA-FISH. **b**, Photoactivated neurite across several planes imaged with a custom-built two-photon microscope. **c**, somas of three example photoactivated cells. Evidence integrator neuron (left), dynamic threshold neuron (middle), motor command neuron (right). Cell identity corresponds in columns with **(d,e)**. **d**, Example functional responses of an evidence integrator neuron (left), a dynamic threshold neuron (middle), and a motor command neuron (right) to RDMS of photoactivated cells. Cell identity corresponds in columns with **c,e**. **d**, Example HCR RNA-FISH staining of an evidence integrator neuron (left), a dynamic threshold neuron (middle), and a motor command neuron (right). Cell identity corresponds in columns with **c,e**. Top left is the GCaMP signal of the photoactivated cell. Top right is a composite of the signal of the HCR RNA-FISH staining of *gad1b* (green) and *vglut2a* (magenta). Bottom left is the signal of the HCR RNA-FISH staining of *gad1b*. Bottom right is the signal of the HCR RNA-FISH staining of *vglut2a*.

3.3.2 Analysis of photoactivated cell neurites

We traced every photoactivated neurite using the simple neurite tracer (Arshadi et al., 2021) integrated in Fiji (Schindelin et al., 2012) from which we received SWC-files representing the neurites morphology (Fig. 12a-i, Fig. 13). We mapped these morphologies to the Z-brain atlas (Randlett et al., 2015) to compare cell morphologies from multiple fish within one reference brain (Fig. 13). Analyzing these neurite morphologies revealed multiple patterns across and within functional types. Cells that were identified by their neural dynamics as dynamic threshold neurons (Fig. 11e, cyan trace) showed a stereotypical morphology (Fig. 12b,d) of projecting downward, arborizing ipsilateral and contralateral and showing one ipsilateral posterior projection. The neurons identified as evidence integrator neurons based on their average neural responses (Fig. 11e, red trace) showed much more diverse projection patterns (Fig. 12a,e,g,h,i). Class 1 of evidence integrator neurons showed only a projection downward from the soma and ipsilateral arborization (Fig. 11e). Class 2 of evidence integrator neurons showed ipsilateral and contralateral projections and ipsilateral and contralateral arborization in their neurites projections. This class can be further subdivided into Class 2a, which addition to the described projection patterns, also showed a posterior projection from the contralateral sides arborization (Fig. 12i) compared to Class 2b, which did not show this posterior projection (Fig. 12i). Class 3 of the evidence integrator neurons are characterized by their projections of neurites, which leave the anterior hindbrain, after projecting downward, into other brain regions like the pretectum (Fig. 12g). Neurons identified as motor command neurons based on their average neural traces and single traces (Fig. 11e) showed diverse projection patterns after projecting downwards from the soma (Fig. 12f). These projection patterns were extraordinary since they projected in some cells, particularly deep or posterior. This rough characterization of functionally characterized cell neurites already shows differences in neurite projection patterns between cell classes and demonstrates the power of this method.

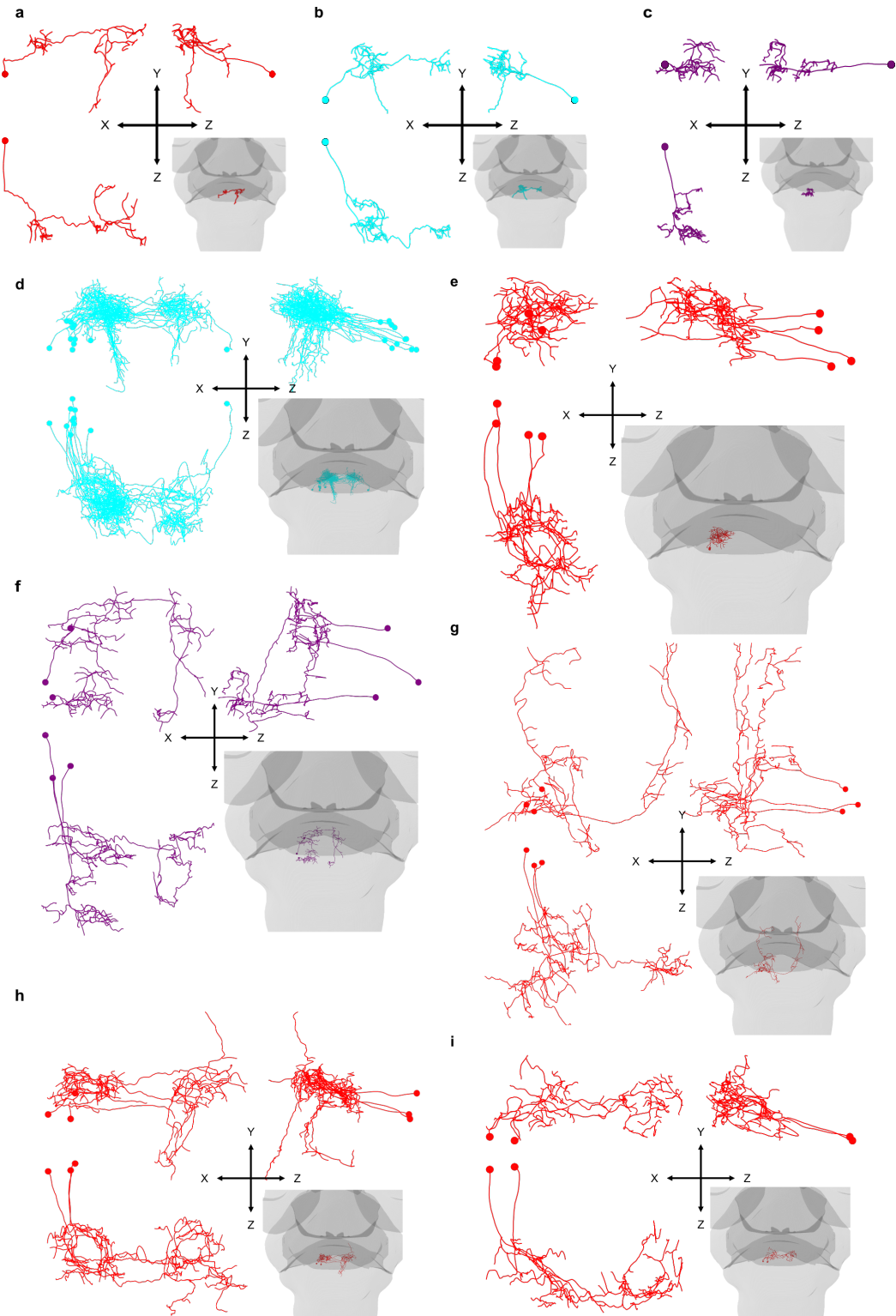


Fig. 12: Neurite morphologies of functionally characterized neurons. Neurite morphologies are coded by color with functional neuron class (evidence integrator neuron = red, dynamic threshold neuron = cyan, motor command neuron = purple). Each subfigure shows a z-projection in the top left, an x-projection in the top right, a y-projection in the bottom left, and the neuron mapped within the z-brain in the bottom right. **a**, Neurite morphology of a single evidence integrator neuron corresponding to the first column of (Fig. 11c,d,e). **b**, Neurite morphology of a single dynamic threshold neuron corresponding to the middle column of (Fig. 11c,d,e). **c**, Neurite morphology of a single motor command neuron corresponding to the right column of (Fig. 11c,d,e). **d-i**, Neurite morphology of all neurons categorized as: **d**, Dynamic threshold neurons. **e**, Evidence integrator neurons of Class 1. **f**, Motor command neurons. **g**, Evidence integrator neurons of Class 3. **h**, Evidence integrator neurons of Class 2a. **i**, Evidence integrator neurons of Class 2b.

3.3.3 Synthesizing functional dynamics, projection patterns, and neurotransmitter identity

By combining all the available information for each cell, we can now further categorize cells. We can see that the only subclass partially showing Vglut2a staining was the contralateral projecting dynamic threshold neurons, while most contralateral projecting dynamic threshold neurons still showed positive for Gad1b. All other cells showed Gad1b staining exclusively or were not identifiable in their HCR RNA-FISH staining. We classified the neurotransmitter identities manually and assigned a certainty level for each identification. Cells that were assigned a certainty below 20% were identified as N/A. N/A also included cells that had problems in their HCR RNA-FISH imaging stacks.

Functional cell type	Morphological subclass	HCR RNA-FISH stain
Evidence integrator neurons	All: 12	Gad1b: 8 Vglut2a: 0 N/A: 4
	Class 1: 4	Gad1b: 3 Vglut2a: 0 N/A: 1
	Class 2a: 3	Gad1b: 2 Vglut2a: 0 N/A: 1
	Class 2b: 2	Gad1b: 1 Vglut2a: 0 N/A: 1
	Class 3: 3	Gad1b: 2 Vglut2a: 0 N/A: 1
Dynamic threshold neurons	All: 11	Gad1b: 7 Vglut2a: 2 N/A: 2
	Ipsilateral: 1	Gad1b: 0 Vglut2a: 0 N/A: 1
	Contralateral: 10	Gad1b: 7 Vglut2a: 2 N/A: 1
Motor command neurons	All: 3	Gad1b: 2 Vglut2a: 0 N/A: 1
	Ipsilateral: 2	Gad1b: 2 Vglut2a: 0 N/A: 0
	Contralateral: 1	Gad1b: 0 Vglut2a: 0 N/A: 1

Table 1: Categorization of neurons by functional cell type, morphological class, and neurotransmitter identity.

This categorization summarizes our approach to evaluating neurons across multiple modalities. We identify cells of neuronal classes by accessing average neural dynamics. These cells are then photoactivated and traced, which enables us to further subcategorize into morphological groups. As a last method, we also add HCR RNA-FISH staining, which completes the picture of a single cell in the motion integrator network.

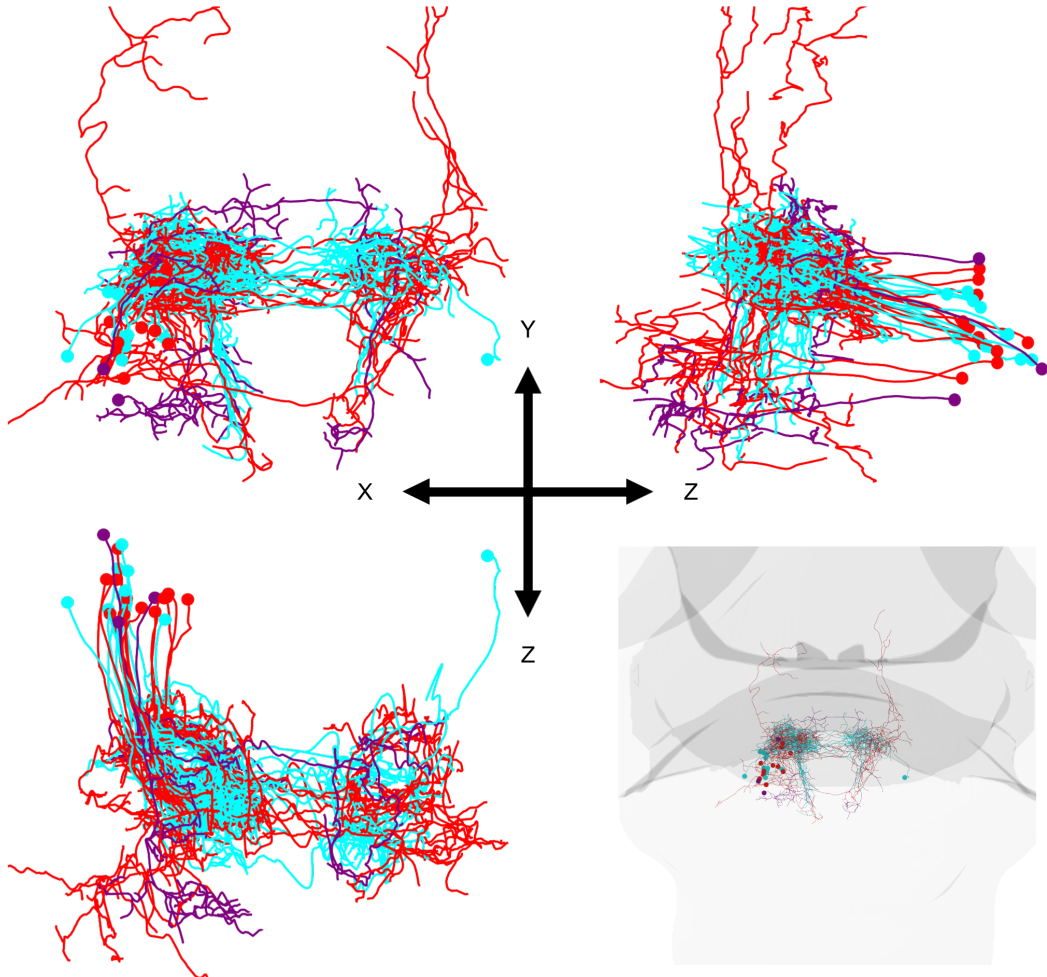


Fig. 13: An overview of all neurite morphologies. Neurite morphologies are coded by color with functional neuron class (evidence integrator neuron = red, dynamic threshold neuron = cyan, motor command neuron = purple). The figure shows all neurite morphologies with identified functional responses and available neurotransmitter identity.

3.4 Discussion

In this chapter, we introduce functionally guided photoactivations as a powerful tool to explore the neural morphology of functionally identified neurons. We show how to combine functional responses, neurite morphology, and neurotransmitter identity to receive a comprehensive understanding of neural networks on the example of the motion integrator network in the anterior hindbrain of the larval zebrafish. Furthermore, we demonstrate how functionally defined classes of neurons show different neural morphology patterns differing in contralateral and ipsilateral neurite projections.

3.4.1 Functionally Guided Photoactivations: A Comparative Analysis of Pros and Cons

As emphasized in the last chapters, neural networks are the sum of their parts and can only be understood by knowing as much as possible about the flow of information through their subparts. This consists of how cells respond in their neural activity to stimuli and how this activity is transmitted to other parts of the network. Calcium imaging solves the problem of what cells do, HCR RNA-FISH solves the problem of how they distribute their activity to other cells of the network, and our introduced photoactivations solve the problem of where cells influence and distribute their signal.

We demonstrate how we can capture a single cell in multiple modalities Fig. 11c shows cells' positions in the brain, Fig. 11e shows the same cells' neural responses to the RDMS, Fig. 11f shows the cells' neurotransmitter identities, and Fig. 12a,b,c showing the corresponding morphologies of the cells. This correlative technique of multiple modalities allows for easy and fast dissection of neural circuits, facilitating the construction of models and enabling rapid validation and formation of new hypotheses.

This focused approach to deconstructing a neural network finds its most similar approach in combined imaging and electroporation (Boulanger-Weill et al., 2017), a comparatively difficult procedure. While we can photoactivate almost as deep as we want in the brain, electroporation is often limited to surface regions of the brain and also depends on the skills of the experimenter. Our method only requires knowledge about the investigated circuits' neural dynamics and correct targeting to recapitulate the morphology of a target cell.

Our demonstrated method is an excellent tool best applied to already established or modeled networks that need further verification. By selecting neurons that show the desired neural dynamics, networks can be targeted specifically to gather more information about this network's projection patterns and, thus, its signal processing pathways. The most common approach to investigate connectomics, electron-microscopy (Eichler et al., 2017; Scheffer et al., 2020), takes a completely different approach by holistic capturing the complete brain and identifying circuits within the data later. Through this holistic approach and the improved resolution of electron microscopy, these huge connectomes (Eichler et al., 2017) contain much more information, making it much easier to detect circuits of connected cells. However, while electron microscopy provides a very detailed morphology of neural circuits, it does not provide any correlated information about cells' function. This problem is addressed through correlated light and electron microscopy, which measures cell responses in the live animal, which is then scanned with an electron microscope. The consecutive mapping of the functional data onto the ultrastructural EM data (Vishwanathan et al., 2017) enables an in-depth analysis of neural morphology in light of cell activity. The downside of CLEM is the high costs and data processing taking a long time due to alignment, segmentation, and other data cleaning procedures. Compared to this, our method is sparse yet focused and only targets cells of interest. Through this, we can iterate between hypothesis formation and hypothesis conformation, while CLEM does not easily adapt to new experimental regimes since they require creating a complete electron microscope imaging volume corresponding to light microscopy data responding to a stimulus testing the hypothesis.

Similar to the one-cell per brain approach is the stochastic expression of neuronal labels in the brain (Kunst et al., 2019). This represents another approach that only exhaustively maps neurite morphology within the brain. Theoretically, this could be combined with volumetric functional imaging to correlate function to the stochastically marked cell. However, the chance of the stochastic expression of the marker appearing in a cell of interest makes this very inefficient.

While our approach shows many advantages through its dynamic and quick nature, it also has limits. The single-cell photoactivations allow for only one neurite per brain, thus never grasping the full connectivity within one brain and speculating on the same network existing in the same form in every fish. Furthermore, this one-cell-per-fish-limit combined with the duration of one experiment, set a low throughput, highlighting the need for a hypothesis to test since, based on time per cell, electron microscopy is still faster than our presented method. This again highlights

functionally guided photoactivations as a method for targeted circuit hypothesis testing and not exhaustive brain mapping.

Another flaw of our method is that the photoactivatable component and the GECI emit green fluorescence since they are both based on GFP. As an alternative, using a red GECI (Dana et al., 2016; Shen et al., 2017) or a red photoactivateable fluorophore would offer many advantages (Lippincott-Schwartz & Patterson, 2009) in addition to the easier differentiability between cells and the photoactivated cell. For example, the photoactivated neurite could be automatically segmented and imaged with higher quality in deeper regions since longer wavelengths travel better through tissue.

Since we aim to understand connectivity within brains, especially the zebrafish hindbrain integrator, we must highlight the biggest flaw of functionally guided photoactivations. Since this is a light microscopy-based method, we cannot infer synapses, which are crucial to exploring connectivity. Inferring connectivity from neurites of cells projecting into similar areas is insufficient to understand single-cell connections. One possible method could be transsynaptic labeling (Desbois et al., 2015; Ni, 2021), ideally labeling postsynaptic cells to stain with an antibody or the previously introduced HCR RNA-FISH, but such methods are not yet developed for zebrafish.

The most obvious solution lies within correlating morphologies of cells reconstructed in electron microscopy datasets with functionally guided photoactivation morphologies. By mapping these morphologies to a reference brain, we could compare morphologies and infer functionality from the light microscopy-acquired morphologies to the EM. This would supply a functionally and neurotransmitter-identified cell, supplied by functionally guided photoactivations, and detailed circuit morphology, supplied by electron microscopy, which would detail the exact connectivity of functional cell types. A CLEM dataset of zebrafish responding to RDMS must be recorded to ensure that functionality morphology pairs correlate across the recording modalities. This would be a major technique to gather insight into the connectivity patterns of functional cell types and would help us further understand how connectivity facilitates computation in neural networks.

In brief, functionally guided photoactivations represent a powerful method to connect cell functionality, neurotransmitter identity, and neurite morphology of a cell. While functionally guided photoactivations cannot help us image post-synaptic partners, we can combine morphologies reconstructed from electron microscopy and light microscopy mapped to a common atlas to infer function within EM datasets. Through this, we could reconstruct complete neural connections of functional cell classes.

3.4.2 Updating the motion integrator circuit through functionally guided photoactivations

We explored the dynamics, neurotransmitter identities, and neural morphologies of 23 cells belonging to the functional classes defined by Bahl and Engert, 2020 using functionally guided photoactivations (Fig. 1, Evidence integrator neurons: 12; Dynamic threshold neurons: 11; Motor command neurons: 3). While analyzing the resulting mapped cell morphologies we were able to identify projections patterns unique to the functional cell classes, indicating a relationship between a cells function and its neurites morphology.

The neurites of dynamic threshold cells (Fig. 12b,d) show a delineated morphology with stereotypical ipsi- and contralateral arborizations and a neurite projecting posterior from the ipsilateral projection. 10 out of the eleven analyzed cells showed this distinctive morphology. In the one not contralateral projecting neurite, the ipsilateral arborization pattern matched the ipsilateral projection pattern of other dynamic threshold cells. This shows how reconstruction probably missed the contralateral projection and arborization due to the matching ipsilateral projections. Furthermore, the dynamic threshold cells were the only functional cell type with cells identified with an excitatory neurotransmitter identity (Fig. 1: 2 cells). The majority of dynamic threshold neurons still showed an

inhibitory neurotransmitter identity (Fig. 1).

These results contrast with the model of the motion integrator of Bahl and Engert, 2020 in two ways. First, they proposed that dynamic threshold neurons only project ipsilateral, which can be refuted due to the delineated morphology of 10 out of 11 cells. Second, they proposed dynamic threshold neurons to only be inhibitory. At the same time, we find 2 out of 11 evaluated dynamic threshold neurons to be excitatory.

Combining morphology and neurotransmitter identity, the contralateral projections of dynamic threshold neurons could be responsible for inhibiting the mirror-symmetric circuit in the other hemisphere. We also propose that the ipsilateral posterior projection could inhibit the motor center, which is positioned in the posterior hindbrain, which would match the proposed model by Bahl and Engert, 2020.

At the same time, it has to be considered that these are only neurite projections and deliver no information about postsynaptic partners, and as already evidenced by the morphologies of the dynamic threshold neurons, projections of neurites can be quite distant. Overall, dynamic threshold neurons show a very delineated and clear morphology, which validates this functional cell class as a defined functional cell type with an associated morphology.

Conversely, evidence integrator neurons show heterogenous morphologies (Fig. 12a,e,g,h,i). All investigated evidence integrator neurons showed an inhibitory or not assignable neurotransmitter identity (Fig. 1). We split their morphologies into 3 different types based on ipsilateral, contralateral, and trans-brainregional projections. This results in Class 1 (Fig. 12e), which only arborizes ipsilateral after projecting downwards into the neuropil region in the ventral anterior hindbrain. We identify an inhibitory neurotransmitter identity based on HCR RNA-FISH identification for this class (Fig. 1). While these kinds of projections were predicted by the model of Bahl and Engert, 2020 since they are a prerequisite for integration processes, they predicted an excitatory neurotransmitter identity. This may be rooted in our relatively narrow focal region of photoactivation in the anterior hindbrain since, as evidenced by Chapter 1 (Fig. 8a), integrators also localize in excitatory regions shown in Chapter 2 (Fig. 9a). It also has to be mentioned here that the most difficult part of the reconstruction of every neurite is the trans-hemispherical projection through the raphe, which contains GCaMP-expressing cells. This could mean that each of these neurons projects to the contralateral side without big contralateral projections since these are easy to spot. We hypothesize that these neurons form recurrent connections to other evidence integrators, thus forming the morphological basis of the integration process in the anterior hindbrain (Synergistic Neural Integration Is Greater Downstream of Recurrent Information Flow in Organotypic Cortical Cultures | BioRxiv, n.d.; R. Yang et al., 2023). Another idea could be that these neurons inhibit the dynamic threshold neurons as proposed by Bahl and Engert, 2020, which would fit with our identified neurotransmitter identity (Fig. 1). Alternatively, we propose that inhibition plays a bigger role in integration processes within sensorimotor transformation networks than previously assumed.

The second class we identify based on neurite projections is Class 2, a group of cells with contralateral projecting neurites (Fig. 12a,h,i). This class's general pattern is ipsilateral arborization and contralateral arborization in the ventral neuropil of the anterior hindbrain after ventral projection from the soma. Contralateral projections of evidence integrators were predicted as a way for the mirror-symmetric circuits to inhibit each other by Bahl and Engert, 2020, which we validate with the identification of this neuron class.

This class can be further subdivided into Class 2a and Class 2b. The main difference between these two classes is Class 2a projecting posteriorly from the arborization on the contralateral side, which neurons of Class 2b do not show. This posterior projection could inhibit the contralateral motor center located in the anterior parts of the hindbrain. This would feed nicely into our hypothesis of dynamic threshold neurons, whose neural activities show how far the system is from reaching its threshold, inhibiting the ipsilateral circuit. In this hypothesis, the evidence integrators, whose neural activities represent how much information has been gathered, would inhibit the contralateral circuit. This would set up a network in which, at the beginning, when there is little evidence integrated, the dynamic threshold neurons inhibit the ipsilateral circuit. As the evidence within the circuit increases, the inhibition of dynamic threshold neurons of motor centers would decrease. While dynamic threshold inhibition would decrease, evidence integrators would start inhibiting the contralateral circuit to bias swimming into their direction.

When evaluating these theories, we have to keep in mind that we cannot distinguish dendrites from axons, which

could mean that the contralateral projections could also serve as input from the contralateral system. The posterior projections could also not relate to motor centers. Instead, they could be a way of physical isolation away from the neuropil regions where the rest of the motion integrator forms its synapses. This would prevent the formation of unspecific synapses within the motion integrator. It is also possible that these neurons inhibit the ipsilateral dynamic threshold neurons with their ipsilateral arborizations.

The last identified type of evidence integrator is Class 3, which differentiates through neural projections leaving the anterior hindbrain into the pretectum or lateral regions (Fig. 12g). All neurons identified showed inhibitory neurotransmitter identity (Fig. 1). We also find one neuron projecting laterally potentially projecting to the motion-responsive clusters identified in eminentia granularis and the locus coreuleus (Fig. 4; Fig. 6ab). We hypothesize these pretectal projections to be dendrites receiving input from preprocessing areas in the pretectum, which Bahl and Engert, 2020 predicted with their model for ipsilateral connections but not contralateral connections.

Summarized, evidence integrators show diverse morphologies in their neural projections into ipsilateral and contralateral areas, with some morphologies even leaving the hindbrain. They show an inhibitory neurotransmitter identity (Fig. 1), which may relate to inhibiting the contralateral circuit or ipsilateral dynamic threshold cells.

For motor command neurons, we identified only 3 neurons so far, which did not allow us to analyze potential projection classes further (Fig. 12f). The general trend is that these neurites project extremely ventral and posterior in ipsilateral and contralateral patterns. This could hint at motor command neurons collecting signals from all over the integration network, which seems reasonable in their function as a downstream target and bottleneck of the neural network.

In addition, we observe that most neurons' contralateral projections cross the midline at the raphe (Fig. 13), potentially identifying this as an area important for trans-hemispherical projections. It is also of note that the raphe is closely located to the interpeduncular nucleus (IPN), which is assumed to be a center of integration. The IPN is proposed to play an important role in a heading direction circuit (Petrucco et al., 2023) as well as in the habenula-IPN axis, which has been connected to learning (Cherng et al., 2020; Palumbo et al., 2020), homeostatic navigation (Palieri et al., 2023), social conflicts (Chou et al., 2016), stress and value-based decision making (Hikosaka, 2010). This adjacency of the IPN and the neurites of cells involved in the motion integration circuit could enable state-dependant modification of the motion integration process in the larval zebrafish.

Overall, we show how functionally defined classes of the motion integrator in the zebrafish hindbrain show unique neuronal morphology. We reveal how the dynamic threshold cells have a very stereotyped morphology, which contradicts the previously established model by Bahl and Engert, 2020. We also demonstrate how HCR RNA-FISH can supply the neurotransmitter identity of target cells. We find almost all of our analyzed neurons to be inhibitory, which urges future investigations of the motion integrator to diversify in photoactivation location. We show how functionally guided photoactivations are a suitable tool to explore functional cell class morphology in the zebrafish brain, enabling us to investigate cells like the newly established functional clusters from Chapter 1. Finally, we demonstrate how functionally guided photoactivations can connect neuronal morphology, functional dynamics, and neurotransmitter identity, establishing it as a powerful tool for circuit dissections.

3.4.3 Conclusion

We have arrived at a point in neural circuit science where methods exist to investigate all the single components of neural circuits. Functional dynamics can be easily captured for the whole brain with ultrasensitive GECIs, morphology can be reconstructed on a synapse scale using electron microscopy, and neurotransmitter identity can be determined using stainings and even imaged *in vivo* (Eriksen et al., 2009). Since all these methods are available, we think it is necessary to synthesize the different modalities of neurons constituting a neural circuit within one animal. In this chapter, we advocate for functionally guided photoactivations as a quick and adaptable hypothesis testing and

generating method connecting cell functionality, neurite morphology, and neurotransmitter identity. We show in the example of the motion integrator within the zebrafish anterior hindbrain (Fig. 12c,e,f; Fig. 12; Fig. 13) how this method can generate mapped neurite morphology based on functional localization of neuron classes. We are confident that comparing these morphologies with morphologies of reconstructed EM cells enables us to map neural dynamics onto EM circuits. This effectively would fill the missing modality in EM datasets and would enable an understanding of neural circuits from a functional perspective, helping us to understand the flow from signal to behavior at its most reduced level. By understanding these circuits at a processing level, we are primed to discover basic principles of how neural circuits solve different fundamental problems like integration and differentiation and further along the interactions with internal state and other neural circuits.

Acknowledgments

First of all, I like to thank Armin Bahl as the person who brought me into neuroscience. I love how you are always excited about science. I love that I can sit down with you and just code and you will take the keyboard from me and just google the same error. I appreciate how you try to engage your students with actual science and how you are a great lab boss. I love how you are up to come up with stupid abbreviations at 11 p.m. And I love how you are a sucker for gossip. Working so far on the mysteries of neural circuits with you was very fun and I'm glad I chose to do my master's with you.

Secondly, I'd like to thank Katja, my supervisor since joining the group. The first thing people say about you is how nice you are, which is true. But what I love most about you is how smart you are. No matter how difficult the question is in the worst case it's still a fun time to think about a solution with Katja. You are also quite the motivator who grounds you in reality. You kicked my ass when I was sciencing in circles and kept me up when nothing worked. It was wonderful to do this master's thesis with you and make fun of Armin when he wasn't looking, and I hope we will forever be able to work together.

Next, I want to thank Heike who I really started to love when I started working with her on the photoactivation project. I love how Heiko says "Enough mulled wine, I need some beer." I love how you remind me about life and admire how you live. Without Heikotron there wouldn't be any HCR RNA-FISH stainings in this thesis. Without Heinau there wouldn't be anyone to ask when you messed up. If I think you are worth the world and we are the luckiest lab in the world to have you.

Next, I'd like to thank my personal (or everyone's personal cheerleader) Phoebe. She was also the only one who constantly corrected this thesis on Google Docs and not in separate PDFs. If Katja is the coals keeping my steam engine running Phoebe is the train of the month award. I love how you believe in others. I love how you are a little silly goose. I think you know I envy your networking skills and I hope you know I'm jealous that I have to share you with so many people—the curse of being too good of a person or something. And I must say you are the most independent, funny, woman in stem. And probably also my favorite silly goose.

Now, I have to thank Bene. Bene is not a man of many words so just thank you for keeping me from a psychotic breakdown during this night when I was transferring this thesis from Google Docs to latex.

I'd also like to thank the rest of the Bahl lab. Ulrike for being so forgiving with my bureaucratic mistakes. Leo, for being a little upside. Max for being a fun, interesting 56-year-old man from the 70s in the body of a Ph.D. student. Roberto for being somebody who loves games. Moritz for somebody who fixes my microscope. Ashrit, for being surprisingly lighthearted. Magnus for being a little bit like-minded. Flutura for keeping me on track. And all the other people who passed through the Bahl lab. You are the thing that makes this place great.

Next, I want to thank my friends Felix Eglinsdörfer and Jonathan Stink. Even though you left me alone in Konstanz before this thing became serious, I still love you guys. I think we will be forever friends and if Johnny manages to pick up his phone and Felix leaves the gym, I'm sure that this will be no problem.

I also want to thank all the people involved somehow with these theses. Be it fixing my internet access or relaxing with me at beer hour. You all are great even if it often doesn't look like it to the outside. I really don't hate anybody. :D

Lastly, I want to thank my family who supported me and were excited with me no matter what I was doing. I love you from my heart and you will always matter to me.

Okay, that's it; everybody who can prove that he read this far gets a free beer on me.

References

- Abrahão, V. P., & Shibatta, O. A. (2015). Gross morphology of the brain of *Pseudopimelodus bufonius* (Valenciennes, 1840) (Siluriformes: Pseudopimelodidae) [Publisher: Sociedade Brasileira de Ictiologia]. *Neotropical Ichthyology*, 13, 255–264. <https://doi.org/10.1590/1982-0224-20130219>
- Adami, C. (2012). The use of information theory in evolutionary biology [eprint: <https://onlinelibrary.wiley.com/doi/pdf/10.1111/j.1749-6632.2011.06422.x>]. *Annals of the New York Academy of Sciences*, 1256(1), 49–65. <https://doi.org/10.1111/j.1749-6632.2011.06422.x>
- Ahrens, M. B., Li, J. M., Orger, M. B., Robson, D. N., Schier, A. F., Engert, F., & Portugues, R. (2012). Brain-wide neuronal dynamics during motor adaptation in zebrafish. *Nature*, 485(7399), 471–477. <https://doi.org/10.1038/nature11057>
- Ahrens, M. B., Orger, M. B., Robson, D. N., Li, J. M., & Keller, P. J. (2013). Whole-brain functional imaging at cellular resolution using light-sheet microscopy. *Nature Methods*, 10(5), 413–420. <https://doi.org/10.1038/nmeth.2434>
- Arshadi, C., Günther, U., Eddison, M., Harrington, K. I. S., & Ferreira, T. A. (2021). SNT: A unifying toolbox for quantification of neuronal anatomy [Number: 4 Publisher: Nature Publishing Group]. *Nature Methods*, 18(4), 374–377. <https://doi.org/10.1038/s41592-021-01105-7>
- Aston-Jones, G., Chen, S., Zhu, Y., & Oshinsky, M. L. (2001). A neural circuit for circadian regulation of arousal [Number: 7 Publisher: Nature Publishing Group]. *Nature Neuroscience*, 4(7), 732–738. <https://doi.org/10.1038/89522>
- Audira, G., Sampurna, B. P., Juniardi, S., Liang, S.-T., Lai, Y.-H., & Hsiao, C.-D. (2018). A Versatile Setup for Measuring Multiple Behavior Endpoints in Zebrafish [Number: 4 Publisher: Multidisciplinary Digital Publishing Institute]. *Inventions*, 3(4), 75. <https://doi.org/10.3390/inventions3040075>
- Avants, B. B., Tustison, N., & Johnson, H. (2015). Advanced Normalization Tools (ANTS).
- Bahl, A., & Engert, F. (2020). Neural circuits for evidence accumulation and decision making in larval zebrafish. *Nature Neuroscience*, 23(1), 94–102. <https://doi.org/10.1038/s41593-019-0534-9>
- Baier, H., & Scott, E. K. (2009). Genetic and optical targeting of neural circuits and behavior—zebrafish in the spotlight. *Current Opinion in Neurobiology*, 19(5), 553–560. <https://doi.org/10.1016/j.conb.2009.08.001>
- Bezdek, J., & Pal, N. (1998). Some new indexes of cluster validity [Conference Name: IEEE Transactions on Systems, Man, and Cybernetics, Part B (Cybernetics)]. *IEEE Transactions on Systems, Man, and Cybernetics, Part B (Cybernetics)*, 28(3), 301–315. <https://doi.org/10.1109/3477.678624>
- Bidel, F., Meirovitch, Y., Schalek, R. L., Lu, X., Pavarino, E. C., Yang, F., Peleg, A., Wu, Y., Shomrat, T., Berger, D. R., Shaked, A., Lichtman, J. W., & Hochner, B. (2023). Connectomics of the Octopus vulgaris vertical lobe provides insight into conserved and novel principles of a memory acquisition network (A. Cardona & J. R. Huguenard, Eds.) [Publisher: eLife Sciences Publications, Ltd]. *eLife*, 12, e84257. <https://doi.org/10.7554/eLife.84257>
- Bilotta, J., & Saszik, S. (2001). The zebrafish as a model visual system. *Int. J. Dev. Neurosci.*, 19(7), 621–629.
- Borst, A. (2014). Neural Circuits for Elementary Motion Detection. *Journal of Neurogenetics*, 28(3-4), 361–373. <https://doi.org/10.3109/01677063.2013.876022>
- Boulanger-Weill, J., Candat, V., Jouary, A., Romano, S. A., Pérez-Schuster, V., & Sumbre, G. (2017). Functional Interactions between Newborn and Mature Neurons Leading to Integration into Established Neuronal Circuits. *Current Biology*, 27(12), 1707–1720.e5. <https://doi.org/10.1016/j.cub.2017.05.029>
- Bradski, G. (2000). The OpenCV Library. *Dr. Dobb's Journal of Software Tools*.
- Buzsáki, G., & Draguhn, A. (2004). Neuronal Oscillations in Cortical Networks [Publisher: American Association for the Advancement of Science]. *Science*, 304(5679), 1926–1929. <https://doi.org/10.1126/science.1099745>
- Buzsáki, G., & Mizuseki, K. (2014). The log-dynamic brain: How skewed distributions affect network operations [Number: 4 Publisher: Nature Publishing Group]. *Nature Reviews Neuroscience*, 15(4), 264–278. <https://doi.org/10.1038/nrn3687>

- Chen, T.-W., Wardill, T. J., Sun, Y., Pulver, S. R., Renninger, S. L., Baohan, A., Schreiter, E. R., Kerr, R. A., Orger, M. B., Jayaraman, V., Looger, L. L., Svoboda, K., & Kim, D. S. (2013). Ultrasensitive fluorescent proteins for imaging neuronal activity. *Nature*, 499(7458), 295–300. <https://doi.org/10.1038/nature12354>
- Chen, X., & Engert, F. (2014). Navigational strategies underlying phototaxis in larval zebrafish. *Frontiers in Systems Neuroscience*, 8, 39. <https://doi.org/10.3389/fnsys.2014.00039>
- Chen, X., Mu, Y., Hu, Y., Kuan, A. T., Nikitchenko, M., Randlett, O., Chen, A. B., Gavornik, J. P., Sompolinsky, H., Engert, F., & Ahrens, M. B. (2018). Brain-wide Organization of Neuronal Activity and Convergent Sensorimotor Transformations in Larval Zebrafish. *Neuron*, 100(4), 876–890.e5. <https://doi.org/10.1016/j.neuron.2018.09.042>
- Cherng, B.-W., Islam, T., Torigoe, M., Tsuboi, T., & Okamoto, H. (2020). The Dorsal Lateral Habenula-Interpeduncular Nucleus Pathway Is Essential for Left-Right-Dependent Decision Making in Zebrafish [Publisher: Elsevier]. *Cell Reports*, 32(11). <https://doi.org/10.1016/j.celrep.2020.108143>
- Choi, H. M. T., Schwarzkopf, M., Fornace, M. E., Acharya, A., Artavanis, G., Stegmaier, J., Cunha, A., & Pierce, N. A. (2018). Third-generation *in situ* hybridization chain reaction: Multiplexed, quantitative, sensitive, versatile, robust. *Development*, 145(12), dev165753. <https://doi.org/10.1242/dev.165753>
- Chou, M.-Y., Amo, R., Kinoshita, M., Cherng, B.-W., Shimazaki, H., Agetsuma, M., Shiraki, T., Aoki, T., Takahoko, M., Yamazaki, M., Higashijima, S.-i., & Okamoto, H. (2016). Social conflict resolution regulated by two dorsal habenular subregions in zebrafish. *Science*, 352(6281), 87–90. <https://doi.org/10.1126/science.aac9508>
- Chudakov, D. M., Belousov, V. V., Zaraisky, A. G., Novoselov, V. V., Staroverov, D. B., Zorov, D. B., Lukyanov, S., & Lukyanov, K. A. (2003). Kindling fluorescent proteins for precise *in vivo* photolabeling [Number: 2 Publisher: Nature Publishing Group]. *Nature Biotechnology*, 21(2), 191–194. <https://doi.org/10.1038/nbt778>
- Chudakov, D. M., Feofanov, A. V., Mudrik, N. N., Lukyanov, S., & Lukyanov, K. A. (2003). Chromophore Environment Provides Clue to “Kindling Fluorescent Protein” Riddle*. *Journal of Biological Chemistry*, 278(9), 7215–7219. <https://doi.org/10.1074/jbc.M211988200>
- Chun, J. J., & Shatz, C. J. (1989). The earliest-generated neurons of the cat cerebral cortex: Characterization by MAP2 and neurotransmitter immunohistochemistry during fetal life [Publisher: Society for Neuroscience Section: Articles]. *Journal of Neuroscience*, 9(5), 1648–1667. <https://doi.org/10.1523/JNEUROSCI.09-05-01648.1989>
- Creamer, M. S., Mano, O., & Clark, D. A. (2018). , and zebrafis. *Neuron*, 100(6), 1460–1473.e6. <https://doi.org/10.1016/j.neuron.2018.10.028>
- Dal Maschio, M., Donovan, J. C., Helmbrecht, T. O., & Baier, H. (2017). Linking Neurons to Network Function and Behavior by Two-Photon Holographic Optogenetics and Volumetric Imaging. *Neuron*, 94(4), 774–789.e5. <https://doi.org/10.1016/j.neuron.2017.04.034>
- Dana, H., Mohar, B., Sun, Y., Narayan, S., Gordus, A., Hasseman, J. P., Tsegaye, G., Holt, G. T., Hu, A., Walpita, D., Patel, R., Macklin, J. J., Bargmann, C. I., Ahrens, M. B., Schreiter, E. R., Jayaraman, V., Looger, L. L., Svoboda, K., & Kim, D. S. (2016). Sensitive red protein calcium indicators for imaging neural activity. *eLife*, 5, e12727. <https://doi.org/10.7554/eLife.12727>
- Desbois, M., Cook, S. J., Emmons, S. W., & Bülow, H. E. (2015). Directional Trans-Synaptic Labeling of Specific Neuronal Connections in Live Animals. *Genetics*, 200(3), 697–705. <https://doi.org/10.1534/genetics.115.177006>
- Dombeck, D. A., Graziano, M. S., & Tank, D. W. (2009). Functional Clustering of Neurons in Motor Cortex Determined by Cellular Resolution Imaging in Awake Behaving Mice [Publisher: Society for Neuroscience Section: Articles]. *Journal of Neuroscience*, 29(44), 13751–13760. <https://doi.org/10.1523/JNEUROSCI.2985-09.2009>
- Douglass, A. D., Kraves, S., Deisseroth, K., Schier, A. F., & Engert, F. (2008). Escape Behavior Elicited by Single, Channelrhodopsin-2-Evoked Spikes in Zebrafish Somatosensory Neurons. *Current Biology*, 18(15), 1133–1137. <https://doi.org/10.1016/j.cub.2008.06.077>
- Dragomir, E. I., Štih, V., & Portugues, R. (2020). Evidence accumulation during a sensorimotor decision task revealed by whole-brain imaging. *Nature Neuroscience*, 23(1), 85–93. <https://doi.org/10.1038/s41593-019-0535-8>

- Dunn, T. W., Gebhardt, C., Naumann, E. A., Riegler, C., Ahrens, M. B., Engert, F., & Del Bene, F. (2016). Neural circuits underlying visually evoked escapes in larval zebrafish [Publisher: Elsevier]. *Neuron*, 89(3), 613–628. <https://doi.org/10.1016/j.neuron.2015.12.021>
- Dunn, T. W., Mu, Y., Narayan, S., Randlett, O., Naumann, E. A., Yang, C.-T., Schier, A. F., Freeman, J., Engert, F., & Ahrens, M. B. (2016). Brain-wide mapping of neural activity controlling zebrafish exploratory locomotion. *eLife*, 5, e12741. <https://doi.org/10.7554/eLife.12741>
- Eichler, K., Li, F., Litwin-Kumar, A., Park, Y., Andrade, I., Schneider-Mizell, C. M., Saumweber, T., Huser, A., Eschbach, C., Gerber, B., Fetter, R. D., Truman, J. W., Priebe, C. E., Abbott, L. F., Thum, A. S., Zlatic, M., & Cardona, A. (2017). The complete connectome of a learning and memory centre in an insect brain. *Nature*, 548(7666), 175–182. <https://doi.org/10.1038/nature23455>
- Eriksen, J., Rasmussen, S. G. F., Rasmussen, T. N., Vaegter, C. B., Cha, J. H., Zou, M.-F., Newman, A. H., & Gether, U. (2009). Visualization of Dopamine Transporter Trafficking in Live Neurons by Use of Fluorescent Cocaine Analogs [Publisher: Society for Neuroscience Section: Articles]. *Journal of Neuroscience*, 29(21), 6794–6808. <https://doi.org/10.1523/JNEUROSCI.4177-08.2009>
- Evans, D. A., Stempel, A. V., Vale, R., Ruehle, S., Lefler, Y., & Branco, T. (2018). A synaptic threshold mechanism for computing escape decisions. *Nature*, 558(7711), 590–594. <https://doi.org/10.1038/s41586-018-0244-6>
- Filippi, A., Mueller, T., & Driever, W. (2014). Vglut2 and gad expression reveal distinct patterns of dual GABAergic versus glutamatergic cotransmitter phenotypes of dopaminergic and noradrenergic neurons in the zebrafish brain [eprint: <https://onlinelibrary.wiley.com/doi/pdf/10.1002/cne.23524>]. *Journal of Comparative Neurology*, 522(9), 2019–2037. <https://doi.org/10.1002/cne.23524>
- Fleisch, V. C., & Neuhauss, S. C. (2006). Visual Behavior in Zebrafish. *Zebrafish*, 3(2), 191–201. <https://doi.org/10.1089/zeb.2006.3.191>
- Förster, D., Dal Maschio, M., Laurell, E., & Baier, H. (2017). An optogenetic toolbox for unbiased discovery of functionally connected cells in neural circuits. *Nature Communications*, 8(1), 116. <https://doi.org/10.1038/s41467-017-00160-z>
- Förster, D., Kramer, A., Baier, H., & Kubo, F. (2018). Optogenetic precision toolkit to reveal form, function and connectivity of single neurons. *Methods*, 150, 42–48. <https://doi.org/10.1016/j.ymeth.2018.08.012>
- Freeman, J., Vladimirov, N., Kawashima, T., Mu, Y., Sofroniew, N. J., Bennett, D. V., Rosen, J., Yang, C.-T., Looger, L. L., & Ahrens, M. B. (2014). Mapping brain activity at scale with cluster computing. *Nature Methods*, 11(9), 941–950. <https://doi.org/10.1038/nmeth.3041>
- Fries, P. (2009). Neuronal Gamma-Band Synchronization as a Fundamental Process in Cortical Computation [eprint: <https://doi.org/10.1146/annurev.neuro.051508.135603>]. *Annual Review of Neuroscience*, 32(1), 209–224. <https://doi.org/10.1146/annurev.neuro.051508.135603>
- Fritschy, J.-M., Weinmann, O., Wenzel, A., & Benke, D. (1998). Synapse-specific localization of NMDA and GABA_A receptor subunits revealed by antigen-retrieval immunohistochemistry [eprint: [https://onlinelibrary.wiley.com/doi/pdf/10.1002/1522-2819\(19980112\)390:2<194::AID-CNE3>3.0.CO;2-X](https://onlinelibrary.wiley.com/doi/pdf/10.1002/1522-2819(19980112)390:2<194::AID-CNE3>3.0.CO;2-X)]. *Journal of Comparative Neurology*, 390(2), 194–210. [https://doi.org/10.1002/\(SICI\)1096-9861\(19980112\)390:2<194::AID-CNE3>3.0.CO;2-X](https://doi.org/10.1002/(SICI)1096-9861(19980112)390:2<194::AID-CNE3>3.0.CO;2-X)
- Fuchsloch, M. (2023). *Brain-wide neural representation of dynamic light processing in Larval Zebrafish* (Master's thesis).
- Giovannucci, A., Friedrich, J., Gunn, P., Kalfon, J., Brown, B. L., Koay, S. A., Taxidis, J., Najafi, F., Gauthier, J. L., Zhou, P., Khakh, B. S., Tank, D. W., Chklovskii, D. B., & Pnevmatikakis, E. A. (2019). CalmAn an open source tool for scalable calcium imaging data analysis. *eLife*, 8, e38173. <https://doi.org/10.7554/eLife.38173>
- Gomez-Marin, A., & Louis, M. (2012). Active sensation during orientation behavior in the Drosophila larva: More sense than luck. *Current Opinion in Neurobiology*, 22(2), 208–215. <https://doi.org/10.1016/j.conb.2011.11.008>
- Groschner, L. N., Malis, J. G., Zuidinga, B., & Borst, A. (2022). A biophysical account of multiplication by a single neuron. *Nature*, 603(7899), 119–123. <https://doi.org/10.1038/s41586-022-04428-3>

- Haesemeyer, M., Schier, A. F., & Engert, F. (2019). Convergent Temperature Representations in Artificial and Biological Neural Networks. *Neuron*, 103(6), 1123–1134.e6. <https://doi.org/10.1016/j.neuron.2019.07.003>
- Hanks, T. D., Ditterich, J., & Shadlen, M. N. (2006). Microstimulation of macaque area LIP affects decision-making in a motion discrimination task. *Nature Neuroscience*, 9(5), 682–689. <https://doi.org/10.1038/nn1683>
- Harris, C. R., Millman, K. J., Walt, S. J. v. d., Gommers, R., Virtanen, P., Cournapeau, D., Wieser, E., Taylor, J., Berg, S., Smith, N. J., Kern, R., Picus, M., Hoyer, S., Kerkwijk, M. H. v., Brett, M., Haldane, A., Río, J. F. d., Wiebe, M., Peterson, P., ... Oliphant, T. E. (2020). Array programming with NumPy [Publisher: Springer Science and Business Media LLC]. *Nature*, 585(7825), 357–362. <https://doi.org/10.1038/s41586-020-2649-2>
- Hartmann, S., Vogt, R., Kunze, J., Rauschert, A., Kuhnert, K.-D., Wanzenböck, J., Lamatsch, D. K., & Witte, K. (2018). Zebrafish larvae show negative phototaxis to near-infrared light (F. Del Bene, Ed.). *PLOS ONE*, 13(11), e0207264. <https://doi.org/10.1371/journal.pone.0207264>
- Hebb, D. O. (1949). *The Organization of Behavior; A Neuropsychological Theory*. John Wiley & Sons.
- Helton, T. D., Zhao, M., Farris, S., & Dudek, S. M. (2019). Diversity of dendritic morphology and entorhinal cortex synaptic effectiveness in mouse CA2 pyramidal neurons. *Hippocampus*, 29(2), 78–92.
- Hikosaka, O. (2010). The habenula: From stress evasion to value-based decision-making. *Nat. Rev. Neurosci.*, 11(7), 503–513.
- Hopfield, J. J. (1982). Neural networks and physical systems with emergent collective computational abilities. [Publisher: Proceedings of the National Academy of Sciences]. *Proceedings of the National Academy of Sciences*, 79(8), 2554–2558. <https://doi.org/10.1073/pnas.79.8.2554>
- Huff, J. (2015). The Airyscan detector from ZEISS: Confocal imaging with improved signal-to-noise ratio and super-resolution. *Nature Methods*, 12(12), i–ii. <https://doi.org/10.1038/nmeth.f.388>
- Huk, A. C., Katz, L. N., & Yates, J. L. (2017). The Role of the Lateral Intraparietal Area in (the Study of) Decision Making. *Annual Review of Neuroscience*, 40(1), 349–372. <https://doi.org/10.1146/annurev-neuro-072116-031508>
- Hwang, B., Lee, J. H., & Bang, D. (2018). Single-cell RNA sequencing technologies and bioinformatics pipelines. *Experimental & Molecular Medicine*, 50(8), 1–14. <https://doi.org/10.1038/s12276-018-0071-8>
- Kalish, B. T., Cheadle, L., Hrvatin, S., Nagy, M. A., Rivera, S., Crow, M., Gillis, J., Kirchner, R., & Greenberg, M. E. (2018). Single-cell transcriptomics of the developing lateral geniculate nucleus reveals insights into circuit assembly and refinement [Publisher: Proceedings of the National Academy of Sciences]. *Proceedings of the National Academy of Sciences*, 115(5), E1051–E1060. <https://doi.org/10.1073/pnas.1717871115>
- Kani, S., Bae, Y.-K., Shimizu, T., Tanabe, K., Satou, C., Parsons, M. J., Scott, E., Higashijima, S.-i., & Hibi, M. (2010). Proneural gene-linked neurogenesis in zebrafish cerebellum. *Developmental Biology*, 343(1), 1–17. <https://doi.org/10.1016/j.ydbio.2010.03.024>
- Kaslin, J., & Brand, M. (2022). Cerebellar Development and Neurogenesis in Zebrafish. In M. U. Manto, D. L. Gruol, J. D. Schmahmann, N. Koibuchi, & R. V. Sillitoe (Eds.), *Handbook of the Cerebellum and Cerebellar Disorders* (pp. 1623–1646). Springer International Publishing. https://doi.org/10.1007/978-3-030-23810-0_63
- Katz, L. N., Yates, J. L., Pillow, J. W., & Huk, A. C. (2016). Dissociated functional significance of decision-related activity in the primate dorsal stream. *Nature*, 535(7611), 285–288. <https://doi.org/10.1038/nature18617>
- Kramer, A., Wu, Y., Baier, H., & Kubo, F. (2019). Neuronal Architecture of a Visual Center that Processes Optic Flow. *Neuron*, 103(1), 118–132.e7. <https://doi.org/10.1016/j.neuron.2019.04.018>
- Krishnan, V., Han, M.-H., Graham, D. L., Berton, O., Renthal, W., Russo, S. J., LaPlant, Q., Graham, A., Lutter, M., Lagace, D. C., Ghose, S., Reister, R., Tannous, P., Green, T. A., Neve, R. L., Chakravarty, S., Kumar, A., Eisch, A. J., Self, D. W., ... Nestler, E. J. (2007). Molecular Adaptations Underlying Susceptibility and Resistance to Social Defeat in Brain Reward Regions. *Cell*, 131(2), 391–404. <https://doi.org/10.1016/j.cell.2007.09.018>
- Kubo, F., Hablitzel, B., Dal Maschio, M., Driever, W., Baier, H., & Arrenberg, A. B. (2014). Functional Architecture of an Optic Flow-Responsive Area that Drives Horizontal Eye Movements in Zebrafish. *Neuron*, 81(6), 1344–1359. <https://doi.org/10.1016/j.neuron.2014.02.043>

- Kunst, M., Laurell, E., Mokayes, N., Kramer, A., Kubo, F., Fernandes, A. M., Förster, D., Dal Maschio, M., & Baier, H. (2019). A Cellular-Resolution Atlas of the Larval Zebrafish Brain. *Neuron*, 103(1), 21–38.e5. <https://doi.org/10.1016/j.neuron.2019.04.034>
- Lein, E. S., Hawrylycz, M. J., Ao, N., Ayres, M., Bensinger, A., Bernard, A., Boe, A. F., Boguski, M. S., Brockway, K. S., Byrnes, E. J., Chen, L., Chen, L., Chen, T.-M., Chi Chin, M., Chong, J., Crook, B. E., Czaplinska, A., Dang, C. N., Datta, S., ... Jones, A. R. (2007). Genome-wide atlas of gene expression in the adult mouse brain [Number: 7124 Publisher: Nature Publishing Group]. *Nature*, 445(7124), 168–176. <https://doi.org/10.1038/nature05453>
- Liao, J. C., & Haehnel, M. (2012). Physiology of afferent neurons in larval zebrafish provides a functional framework for lateral line somatotopy [Publisher: American Physiological Society]. *Journal of Neurophysiology*, 107(10), 2615–2623. <https://doi.org/10.1152/jn.01108.2011>
- Lippincott-Schwartz, J., & Patterson, G. H. (2009). Photoactivatable fluorescent proteins for diffraction-limited and super-resolution imaging. *Trends in Cell Biology*, 19(11), 555–565. <https://doi.org/10.1016/j.tcb.2009.09.003>
- Lovett-Barron, M., Andelman, A. S., Allen, W. E., Vesuna, S., Kauvar, I., Burns, V. M., & Deisseroth, K. (2017). Ancestral Circuits for the Coordinated Modulation of Brain State. *Cell*, 171(6), 1411–1423.e17. <https://doi.org/10.1016/j.cell.2017.10.021>
- Lovett-Barron, M., Chen, R., Bradbury, S., Andelman, A. S., Wagle, M., Guo, S., & Deisseroth, K. (2020). Multiple convergent hypothalamus–brainstem circuits drive defensive behavior [Number: 8 Publisher: Nature Publishing Group]. *Nature Neuroscience*, 23(8), 959–967. <https://doi.org/10.1038/s41593-020-0655-1>
- Lowekamp, B. C., Chen, D. T., Ibáñez, L., & Blezek, D. (2013). The Design of SimpleITK. *Front. Neuroinform.*, 7, 45. <https://doi.org/https://doi.org/10.3389/fninf.2013.00045>
- Lukyanov, K. A., Chudakov, D. M., Lukyanov, S., & Verkhusha, V. V. (2005). Photoactivatable fluorescent proteins [Number: 11 Publisher: Nature Publishing Group]. *Nature Reviews Molecular Cell Biology*, 6(11), 885–890. <https://doi.org/10.1038/nrm1741>
- Makino, H., Hwang, E. J., Hedrick, N. G., & Komiyama, T. (2016). Circuit Mechanisms of Sensorimotor Learning. *Neuron*, 92(4), 705–721. <https://doi.org/10.1016/j.neuron.2016.10.029>
- Maley, B. E. (1996). Immunohistochemical Localization of Neuropeptides and Neurotransmitters in the Nucleus Solitarius. *Chemical Senses*, 21(3), 367–376. <https://doi.org/10.1093/chemse/21.3.367>
- Malleret, G., Alarcon, J. M., Martel, G., Takizawa, S., Vronskaya, S., Yin, D., Chen, I. Z., Kandel, E. R., & Shumyatsky, G. P. (2010). Bidirectional Regulation of Hippocampal Long-Term Synaptic Plasticity and Its Influence on Opposing Forms of Memory. *The Journal of Neuroscience*, 30(10), 3813–3825. <https://doi.org/10.1523/JNEUROSCI.1330-09.2010>
- Masquelier, T., & Thorpe, S. J. (2007). Unsupervised Learning of Visual Features through Spike Timing Dependent Plasticity [Publisher: Public Library of Science]. *PLOS Computational Biology*, 3(2), e31. <https://doi.org/10.1371/journal.pcbi.0030031>
- McCormick, C. A. (1989). Central Lateral Line Mechanosensory Pathways in Bony Fish. In S. Coombs, P. Görner, & H. Münz (Eds.), *The Mechanosensory Lateral Line* (pp. 341–364). Springer. https://doi.org/10.1007/978-1-4612-3560-6_17
- McNaughton, B. L., Battaglia, F. P., Jensen, O., Moser, E. I., & Moser, M.-B. (2006). Path integration and the neural basis of the 'cognitive map' [Number: 8 Publisher: Nature Publishing Group]. *Nature Reviews Neuroscience*, 7(8), 663–678. <https://doi.org/10.1038/nrn1932>
- Meissner, G. W., Nern, A., Singer, R. H., Wong, A. M., Malkesman, O., & Long, X. (2019). Mapping Neurotransmitter Identity in the Whole-Mount Drosophila Brain Using Multiplex High-Throughput Fluorescence in Situ Hybridization. *Genetics*, 211(2), 473–482. <https://doi.org/10.1534/genetics.118.301749>
- Milligan, G. W., & Cooper, M. C. (1985). An examination of procedures for determining the number of clusters in a data set. *Psychometrika*, 50(2), 159–179. <https://doi.org/10.1007/BF02294245>
- Mu, Y., Bennett, D. V., Rubinov, M., Narayan, S., Yang, C.-T., Tanimoto, M., Mensh, B. D., Looger, L. L., & Ahrens, M. B. (2019). Glia Accumulate Evidence that Actions Are Futile and Suppress Unsuccessful Behavior. *Cell*, 178(1), 27–43.e19. <https://doi.org/10.1016/j.cell.2019.05.050>

- Naumann, E. A., Fitzgerald, J. E., Dunn, T. W., Rihel, J., Sompolinsky, H., & Engert, F. (2016). From Whole-Brain Data to Functional Circuit Models: The Zebrafish Optomotor Response. *Cell*, 167(4), 947–960.e20. <https://doi.org/10.1016/j.cell.2016.10.019>
- Newsome, W., & Pare, E. (1988). A selective impairment of motion perception following lesions of the middle temporal visual area (MT). *The Journal of Neuroscience*, 8(6), 2201–2211. <https://doi.org/10.1523/JNEUROSCI.08-06-02201.1988>
- Ni, L. (2021). Genetic Transsynaptic Techniques for Mapping Neural Circuits in Drosophila. *Frontiers in Neural Circuits*, 15. Retrieved August 31, 2023, from <https://www.frontiersin.org/articles/10.3389/fncir.2021.749586>
- Ohki, K., Chung, S., Ch'ng, Y. H., Kara, P., & Reid, R. C. (2005). Functional imaging with cellular resolution reveals precise micro-architecture in visual cortex. *Nature*, 433(7026), 597–603. <https://doi.org/10.1038/nature03274>
- Palieri, V., Paoli, E., Kadov, I. C. G., & Portugues, R. (2023). The Preoptic Area and Dorsal Habenula Jointly Support Homeostatic Navigation in Larval Zebrafish [Pages: 2023.05.18.541289 Section: New Results]. <https://doi.org/10.1101/2023.05.18.541289>
- Palumbo, F., Serneels, B., Pelgrims, R., & Yaksi, E. (2020). The Zebrafish Dorsolateral Habenula Is Required for Updating Learned Behaviors. *Cell Reports*, 32(8), 108054. <https://doi.org/10.1016/j.celrep.2020.108054>
- Pan, Y. A., Livet, J., Sanes, J. R., Lichtman, J. W., & Schier, A. F. (2011). Multicolor Brainbow Imaging in Zebrafish [Publisher: Cold Spring Harbor Laboratory Press]. *Cold Spring Harbor Protocols*, 2011(1), pdb.prot5546. <https://doi.org/10.1101/pdb.prot5546>
- Patterson, G. H., & Lippincott-Schwartz, J. (2002). A Photoactivatable GFP for Selective Photolabeling of Proteins and Cells. *Science*, 297(5588), 1873–1877. <https://doi.org/10.1126/science.1074952>
- Pedregosa, F., Varoquaux, G., Gramfort, A., Michel, V., Thirion, B., Grisel, O., Blondel, M., Prettenhofer, P., Weiss, R., Dubourg, V., Vanderplas, J., Passos, A., Cournapeau, D., Brucher, M., Perrot, M., & Duchesnay, É. (2011). Scikit-learn: Machine Learning in Python. *Journal of Machine Learning Research*, 12, 2825–2830.
- Pereira, L., Kratsios, P., Serrano-Saiz, E., Sheftel, H., Mayo, A. E., Hall, D. H., White, J. G., LeBoeuf, B., Garcia, L. R., Alon, U., & Hobert, O. (2015). A cellular and regulatory map of the cholinergic nervous system of *C. elegans* (K. Shen, Ed.) [Publisher: eLife Sciences Publications, Ltd]. *eLife*, 4, e12432. <https://doi.org/10.7554/eLife.12432>
- Petrucco, L., Lavian, H., Wu, Y. K., Svara, F., Štih, V., & Portugues, R. (2023). Neural dynamics and architecture of the heading direction circuit in zebrafish [Publisher: Nature Publishing Group]. *Nature Neuroscience*, 1–9. <https://doi.org/10.1038/s41593-023-01308-5>
- Priestley, J. V., Somogyi, P., & Cuello, A. C. (1981). Neurotransmitter-specific projection neurons revealed by combining PAP immunohistochemistry with retrograde transport of HRP. *Brain Research*, 220(2), 231–240. [https://doi.org/10.1016/0006-8993\(81\)91214-2](https://doi.org/10.1016/0006-8993(81)91214-2)
- Qin, M., Wong, A., Seguin, D., & Gerlai, R. (2014). Induction of Social Behavior in Zebrafish: Live Versus Computer Animated Fish as Stimuli [Publisher: Mary Ann Liebert, Inc., publishers]. *Zebrafish*, 11(3), 185–197. <https://doi.org/10.1089/zeb.2013.0969>
- R. Tyrrell Rockafellar, M. W., Roger J.-B. Wets. (2009). Pompeiu-Hausdorff Distance. In *Variational analysis* (draft with corrections, Springer, pp. 117–118). Springer.
- Randlett, O., Wee, C. L., Naumann, E. A., Nnaemeka, O., Schoppik, D., Fitzgerald, J. E., Portugues, R., Lacoste, A. M. B., Riegler, C., Engert, F., & Schier, A. F. (2015). Whole-brain activity mapping onto a zebrafish brain atlas. *Nature Methods*, 12(11), 1039–1046. <https://doi.org/10.1038/nmeth.3581>
- Ratcliff, R., & McKoon, G. (2008). The Diffusion Decision Model: Theory and Data for Two-Choice Decision Tasks. *Neural Computation*, 20(4), 873–922. <https://doi.org/10.1162/neco.2008.12-06-420>
- Reddy, G., Desban, L., Tanaka, H., Roussel, J., Mirat, O., & Wyart, C. (2021). A lexical approach for identifying behavioral action sequences [Pages: 2020.08.27.270694 Section: New Results]. <https://doi.org/10.1101/2020.08.27.270694>
- Rorden, C. (2023). Nii2mesh: A tool for converting NIfTI 3D voxel images to triangulated meshes. <https://github.com/neurolabusc/nii2mesh>

- Ruta, V., Datta, S. R., Vasconcelos, M. L., Freeland, J., Looger, L. L., & Axel, R. (2010). A dimorphic pheromone circuit in *Drosophila* from sensory input to descending output. *Nature*, 468(7324), 686–690. <https://doi.org/10.1038/nature09554>
- Sato, T., Takahoko, M., & Okamoto, H. (2006). HuC:Kaede, a useful tool to label neural morphologies in networks in vivo. *genesis*, 44(3), 136–142. <https://doi.org/10.1002/gene.20196>
- Satou, C., Kimura, Y., Hirata, H., Suster, M. L., Kawakami, K., & Higashijima, S.-i. (2013). Transgenic tools to characterize neuronal properties of discrete populations of zebrafish neurons. *Development*, 140(18), 3927–3931. <https://doi.org/10.1242/dev.099531>
- Saverino, C., & Gerlai, R. (2008). The social zebrafish: Behavioral responses to conspecific, heterospecific, and computer animated fish. *Behavioural Brain Research*, 191(1), 77–87. <https://doi.org/10.1016/j.bbr.2008.03.013>
- Scheffer, L. K., Xu, C. S., Januszewski, M., Lu, Z., Takemura, S.-y., Hayworth, K. J., Huang, G. B., Shinomiya, K., Maitlin-Shepard, J., Berg, S., Clements, J., Hubbard, P. M., Katz, W. T., Umayam, L., Zhao, T., Ackerman, D., Blakely, T., Bogovic, J., Dolafi, T., ... Plaza, S. M. (2020). A connectome and analysis of the adult *Drosophila* central brain. *eLife*, 9, e57443. <https://doi.org/10.7554/eLife.57443>
- Schindelin, J., Arganda-Carreras, I., Frise, E., Kaynig, V., Longair, M., Pietzsch, T., Preibisch, S., Rueden, C., Saalfeld, S., Schmid, B., Tinevez, J.-Y., White, D. J., Hartenstein, V., Eliceiri, K., Tomancak, P., & Cardona, A. (2012). Fiji: An open-source platform for biological-image analysis. *Nature Methods*, 9(7), 676–682. <https://doi.org/10.1038/nmeth.2019>
- Schlegel, P., Barnes, C. L., Champion, A., Tokarz, D., Jagannathan, S., Williams, R., Pedigo, B. D., Messense, Y., Zatian, A., Ortega Jiménez, A., & Newstein, P. (2023). NAVis: Python library for Neuron Analysis and Visualization [Publication Title: GitHub repository]. <https://github.com/navis-org/navis>
- Schoonheim, P. J., Arrenberg, A. B., Del Bene, F., & Baier, H. (2010). Optogenetic Localization and Genetic Perturbation of Saccade-Generating Neurons in Zebrafish. *Journal of Neuroscience*, 30(20), 7111–7120. <https://doi.org/10.1523/JNEUROSCI.5193-09.2010>
- Schulze, L., Zada, D., & Lovett-Barron, M. (2023). A medley of gene expression adds new depth to zebrafish brain maps [Publisher: American Association for the Advancement of Science]. *Science Advances*, 9(8), eadg8660. <https://doi.org/10.1126/sciadv.adg8660>
- Shadlen, M. N., & Newsome, W. T. (2001). Neural Basis of a Perceptual Decision in the Parietal Cortex (Area LIP) of the Rhesus Monkey. *Journal of Neurophysiology*, 86(4), 1916–1936. <https://doi.org/10.1152/jn.2001.86.4.1916>
- Shainer, I., Kuehn, E., Laurell, E., Kassar, M. A., Mokayes, N., Sherman, S., Larsch, J., Kunst, M., & Baier, H. (2023). A single-cell resolution gene expression atlas of the larval zebrafish brain. *Science Advances*, 9(eade9909).
- Shariatgorji, R., Nilsson, A., Fridjonsdottir, E., Strittmatter, N., Dannhorn, A., Svensson, P., Goodwin, R. J. A., Odell, L. R., & Andrén, P. E. (2021). Spatial visualization of comprehensive brain neurotransmitter systems and neuroactive substances by selective in situ chemical derivatization mass spectrometry imaging [Number: 7 Publisher: Nature Publishing Group]. *Nature Protocols*, 16(7), 3298–3321. <https://doi.org/10.1038/s41596-021-00538-w>
- Shen, Y., Dana, H., Abdelfattah, A. S., Patel, R., Shea, J., Molina, R. S., Rawal, B., Rancic, V., Chang, Y.-F., Wu, L., Chen, Y., Qian, Y., Wiens, M. D., Hambleton, N., Ballanyi, K., Hughes, T. E., Drobizhev, M., Kim, D. S., Koyama, M., ... Campbell, R. E. (2017). A genetically encoded Ca²⁺ indicator based on circularly permuted sea anemone red fluorescent protein [Pages: 213082 Section: New Results]. <https://doi.org/10.1101/213082>
- Stringer, C., Wang, T., Michaelos, M., & Pachitariu, M. (2021). Cellpose: A generalist algorithm for cellular segmentation. *Nature Methods*, 18(1), 100–106. <https://doi.org/10.1038/s41592-020-01018-x>
- Surer, E. (2020). Panda3D. In N. Lee (Ed.), *Encyclopedia of Computer Graphics and Games* (pp. 1–3). Springer International Publishing. https://doi.org/10.1007/978-3-319-08234-9_535-1

- Tapia, M., Baudot, P., Formisano-Tréziny, C., Dufour, M. A., Temporal, S., Lasserre, M., Marquèze-Pouey, B., Gabert, J., Kobayashi, K., & Goaillard, J.-M. (2018). Neurotransmitter identity and electrophysiological phenotype are genetically coupled in midbrain dopaminergic neurons [Number: 1 Publisher: Nature Publishing Group]. *Scientific Reports*, 8(1), 13637. <https://doi.org/10.1038/s41598-018-31765-z>
- Tavenard, R., Faouzi, J., Vandewiele, G., Divo, F., Androz, G., Holtz, C., Payne, M., Yurchak, R., Rußwurm, M., Kolar, K., & Woods, E. (2020). Tslearn, A Machine Learning Toolkit for Time Series Data. *Journal of Machine Learning Research*, 21(118), 1–6. <http://jmlr.org/papers/v21/20-091.html>
- Tsao, C.-H., Chen, C.-C., Lin, C.-H., Yang, H.-Y., & Lin, S. (2018). Drosophila mushroom bodies integrate hunger and satiety signals to control innate food-seeking behavior (K. Scott, Ed.) [Publisher: eLife Sciences Publications, Ltd]. *eLife*, 7, e35264. <https://doi.org/10.7554/eLife.35264>
- Tustison, N. J., & Avants, B. B. (2013). Explicit B-spline regularization in diffeomorphic image registration. *Frontiers in Neuroinformatics*, 7, 39. <https://doi.org/10.3389/fninf.2013.00039>
- Umargono, E., Suseno, J. E., & S. K., V. G. (2019). K-Means Clustering Optimization using the Elbow Method and Early Centroid Determination Based-on Mean and Median: *Proceedings of the International Conferences on Information System and Technology*, 234–240. <https://doi.org/10.5220/0009908402340240>
- Vargas, R., Jóhannesdóttir, I. þ., Sigurgeirsson, B., Þorsteinsson, H., & Karlsson, K. Æ. (2011). The zebrafish brain in research and teaching: A simple *in vivo* and *in vitro* model for the study of spontaneous neural activity. *Advances in Physiology Education*, 35(2), 188–196. <https://doi.org/10.1152/advan.00099.2010>
- Virtanen, P., Gommers, R., Oliphant, T. E., Haberland, M., Reddy, T., Cournapeau, D., Burovski, E., Peterson, P., Weckesser, W., Bright, J., van der Walt, S. J., Brett, M., Wilson, J., Millman, K. J., Mayorov, N., Nelson, A. R. J., Jones, E., Kern, R., Larson, E., ... van Mulbregt, P. (2020). SciPy 1.0: Fundamental algorithms for scientific computing in Python [Number: 3 Publisher: Nature Publishing Group]. *Nature Methods*, 17(3), 261–272. <https://doi.org/10.1038/s41592-019-0686-2>
- Vishwanathan, A., Daie, K., Ramirez, A. D., Lichtman, J. W., Aksay, E. R., & Seung, H. S. (2017). Electron Microscopic Reconstruction of Functionally Identified Cells in a Neural Integrator. *Current Biology*, 27(14), 2137–2147.e3. <https://doi.org/10.1016/j.cub.2017.06.028>
- Vladimirov, N., Mu, Y., Kawashima, T., Bennett, D. V., Yang, C.-T., Looger, L. L., Keller, P. J., Freeman, J., & Ahrens, M. B. (2014). Light-sheet functional imaging in fictively behaving zebrafish. *Nature Methods*, 11(9), 883–884. <https://doi.org/10.1038/nmeth.3040>
- Wang, K., Hinz, J., Haikala, V., Reiff, D. F., & Arrenberg, A. B. (2019). Selective processing of all rotational and translational optic flow directions in the zebrafish pretectum and tectum. *BMC Biology*, 17(1), 29. <https://doi.org/10.1186/s12915-019-0648-2>
- Wannemacher, M. A. (2023). Whole-brain activity mapping by immediate early gene *c-fos* HCR RNA-FISH imaging in larval zebrafish.
- Weston, M. C., Nehring, R. B., Wojcik, S. M., & Rosenmund, C. (2011). Interplay between VGLUT Isoforms and Endophilin A1 Regulates Neurotransmitter Release and Short-Term Plasticity. *Neuron*, 69(6), 1147–1159. <https://doi.org/10.1016/j.neuron.2011.02.002>
- Wilcoxon, F. (1945). Individual Comparisons by Ranking Methods [Publisher: International Biometric Society]. *Biometrics Bulletin*, 1(6), 80–83. <http://links.jstor.org/sici?&sici=0099-4987%28194512%291%3A6%3C80%3AICBRM%3E2.0.CO%3B2-P>
- Wilson, J. M., Bunte, R. M., & Cartt, A. J. (2009). Evaluation of Rapid Cooling and Tricaine Methanesulfonate (MS222) as Methods of Euthanasia in Zebrafish (*Danio rerio*). *Journal of the American Association for Laboratory Animal Science*, 48(6), 5.
- Yang, E., Zwart, M. F., James, B., Rubinov, M., Wei, Z., Narayan, S., Vladimirov, N., Mensh, B. D., Fitzgerald, J. E., & Ahrens, M. B. (2022). A brainstem integrator for self-location memory and positional homeostasis in zebrafish [Publisher: Elsevier]. *Cell*, 185(26), 5011–5027.e20. <https://doi.org/10.1016/j.cell.2022.11.022>

- Yang, R., Vishwanathan, A., Wu, J., Kemnitz, N., Ih, D., Turner, N., Lee, K., Tartavull, I., Silversmith, W. M., Jordan, C. S., David, C., Bland, D., Sterling, A., Goldman, M. S., Aksay, E. R., & Seung, H. S. (2023). Cyclic structure with cellular precision in a vertebrate sensorimotor neural circuit. *Current Biology*, 33(11), 2340–2349.e3. <https://doi.org/10.1016/j.cub.2023.05.010>
- Yates, J. L., Park, I. M., Katz, L. N., Pillow, J. W., & Huk, A. C. (2017). Functional dissection of signal and noise in MT and LIP during decision-making. *Nature Neuroscience*, 20(9), 1285–1292. <https://doi.org/10.1038/nn.4611>
- Zhang, Y., & Looger, L. L. (2023). Fast and sensitive GCaMP calcium indicators for neuronal imaging [eprint: <https://onlinelibrary.wiley.com/doi/pdf/10.1113/JP283832>]. *The Journal of Physiology*, n/a(n/a). <https://doi.org/10.1113/JP283832>
- Zheng, Z., Lauritzen, J. S., Perlman, E., Robinson, C. G., Nichols, M., Milkie, D., Torrens, O., Price, J., Fisher, C. B., Sharifi, N., Calle-Schuler, S. A., Kmecova, L., Ali, I. J., Karsh, B., Trautman, E. T., Bogovic, J. A., Hanslovsky, P., Jefferis, G. S., Kazhdan, M., ... Bock, D. D. (2018). A Complete Electron Microscopy Volume of the Brain of Adult *Drosophila melanogaster*. *Cell*, 174(3), 730–743.e22. <https://doi.org/10.1016/j.cell.2018.06.019>
- Zitová, B., & Flusser, J. (2003). Image registration methods: A survey. *Image and Vision Computing*, 21(11), 977–1000. [https://doi.org/10.1016/S0262-8856\(03\)00137-9](https://doi.org/10.1016/S0262-8856(03)00137-9)

Acronyms

GECI genetically encoded calcium indicator

dpf days post fertilization

OMR optomotor response

GFP Green fluorescent protein

RDMS random dot motion stimuli

LIP lateral intraparietal cortex

MT middle temporal visual area

PMT photomultiplier tubes

CalmAn computational toolbox for large-scale calcium imaging data analysis

PMR preferred motion responses

NPMR non-preferred motion responses

RDMS-L leftward random dot motion stimuli

RDMS-R rightward random dot motion stimuli

ANTs Advanced Normalization Tools

nn-CC nearest neighbor cross correlation metric

nn-MI nearest neighbor mutual information metric

msd-CC most similar distance cross-correlation metric

msd-MI most similar distance mutual information metric

HCR RNA-FISH Hybridization Chain Reaction Ribonucleic Acid Fluorescence In Situ Hybridization

GABA gamma-aminobutyric acid

mRNA messenger ribonucleic acid

CLEM correlated light and electron microscopy

EM electron microscopy

IPN interpeduncular nucleus